

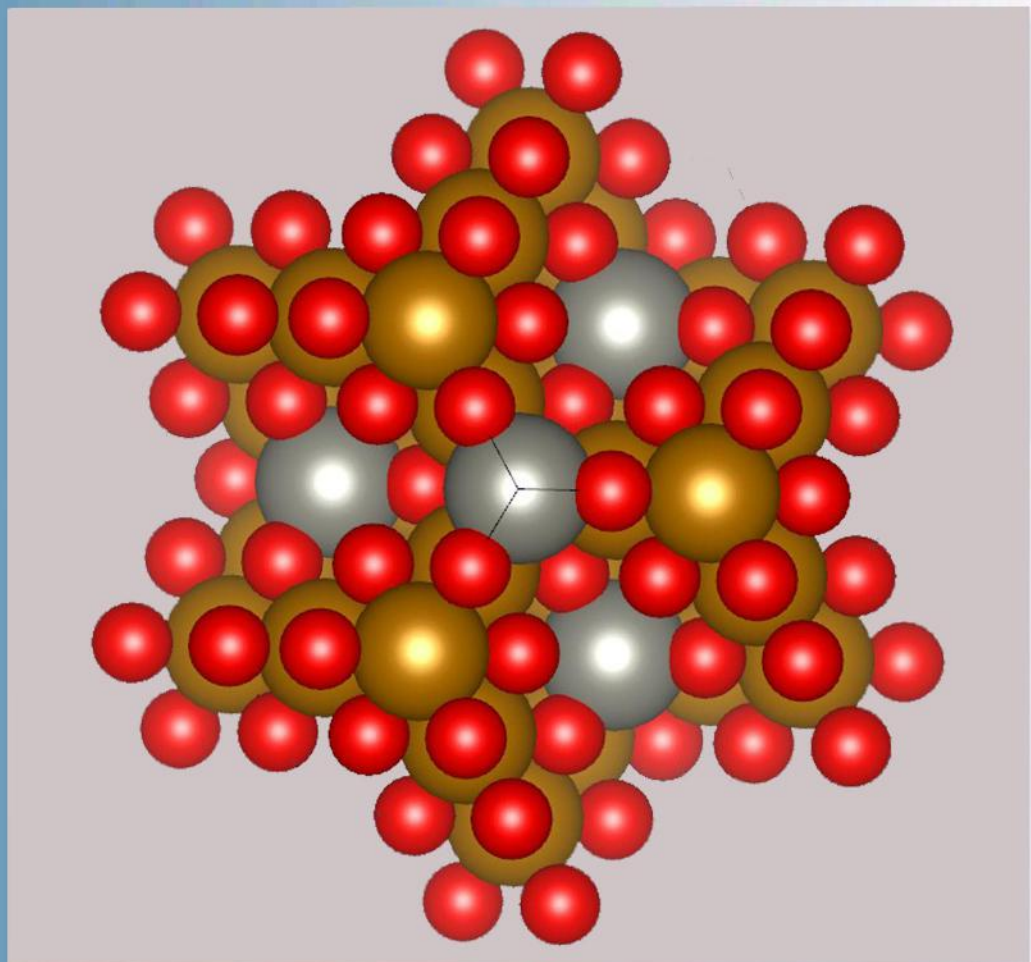


ISSN 1028-8546

Volume XXIX Number 1
Section: En March 2023

Azerbaijan Journal of Physics

Fizika



www.physics.gov.az
www.physics.gov.az/ajpfizika.html

Institute of Physics

Ministry of Science and Education Republic of Azerbaijan

Published from 1995
Ministry of Press and Information
of Azerbaijan Republic,
Registration number 514, 20.02.1995

ISSN 1028-8546
vol. XXIX, Number 01, 2023
Section: En

Azerbaijan Journal of Physics

FIZIKA

*Ministry of Science and Education Republic of Azerbaijan
Institute of Physics*

HONORARY EDITORS

Arif PASHAYEV

EDITORS-IN-CHIEF

Arif HASHIMOV

SENIOR EDITOR

Talat MEHDIYEV

INTERNATIONAL REVIEW BOARD

Arif Hashimov, Azerbaijan
Boris Denker, Russia
Vyacheslav Tuzlukov, Belarus
Gennadii Jablonskii, Belarus
Vladimir Man'ko, Russia
Mirhasan Seyidov, Turkey
Dieter Hochheimer, USA
Victor L'vov, Israel
Majid Ebrahim-Zadeh, Spain

Huseyn Ibragimov, Azerbaijan
Nazim Mamedov, Azerbaijan
Anatoly Boreysho, Russia
Mikhail Khalin, Russia
Javad Abdinov, Azerbaijan
Faik Mikailzade, Turkey
Tayar Djafarov, Azerbaijan
Kerim Allahverdiyev, Azerbaijan
Talat Mehdiyev, Azerbaijan

Zakir Jahangirli, Azerbaijan
Salima Mehdiyeva, Azerbaijan
Nadir Abdullayev, Azerbaijan
Oktay Tagiyev, Azerbaijan
Ayaz Bayramov, Azerbaijan
Tofiq Mammadov, Azerbaijan
Shakir Nagiyev, Azerbaijan
Rauf Guseynov, Azerbaijan

TECHNICAL EDITORIAL BOARD

Senior secretary: Elmira Akhundova; Nazli Huseynova, Elshana Aleskerova,
Rena Nayimbayeva, Nigar Aliyeva.

PUBLISHING OFFICE

131, H. Javid ave., AZ-1143, Baku
Ministry of Science and Education
Republic of Azerbaijan, Institute of Physics

Tel.: (99412) 539-51-63, 539-32-23
Fax: (99412) 537-22-92
E-mail: jophphysics@gmail.com
Internet: www.physics.gov.az

Published at " _____ "
_____ str., Baku

Sent for printing on: _____. 201_
Printing approved on: _____. 201_
Physical binding: _____
Number of copies: _____200
Order: _____

It is authorized for printing:

THERMAL PHOTONS PRODUCTION IN PROTON-PROTON COLLISIONS AT HIGH ENERGIES

PART I. DIFFERENTIAL CROSS-SECTIONS OF PROCESSES, CALCULATED WITHOUT AND TAKING INTO ACCOUNT FORMFACTOR OF MESONS

M.R. ALIZADA, A.I. AHMADOV

Department of Theoretical Physics, Baku State University

str. Z. Khalilov, 23, Az-1148 Baku, Azerbaijan

E-mail: mohsunalizade@gmail.com

Thermal photons produced in following processes: $\pi^+\pi^- \rightarrow \gamma\rho^0$, $\pi^\pm\rho^0 \rightarrow \gamma\pi^\pm$, $\rho^0 \rightarrow \gamma\pi^+\pi^-$, $\pi^+\pi^- \rightarrow \gamma\eta$, $\pi^\pm\eta \rightarrow \gamma\pi^\pm$, $\pi^+\pi^- \rightarrow \gamma\gamma$ are considered Feynman diagrams of processes and matrix elements has been wrote. Differential cross-sections of processes has been calculated without and taking account formfactor of mesons. The dependencies of differential cross-sections of processes of production thermal photons on energy of colliding mesons (\sqrt{s}), transverse momentum (p_T) and on cosine of scattering angle of photons has been determined and has been comparised.

Keywords: proton-proton collision, mesons, thermal photons, Feynman diagram, differential cross-section.

PACS: 13.75.Lb; 13.30.Eg; 13.20.Cz; 13.25.Cq

I. INTRODUCTION

Photons are one of the main products of proton-proton collision at high energies. Photons interact only electromagnetically, and therefore their average free paths are usually much larger than the transverse size of the region of hot matter created in any nuclear collision. As a result, high energy photons formed in the interior of the plasma typically pass through the surrounding substance without interaction, carrying information directly from anywhere from where they were formed to the detector. Depending on the mechanism of their production, direct photons are usually divided into two main categories: prompt and thermal photons [1,2].

Photons produced in a proton-proton (prompt photons) collision with energy in the range from 1.5 to several *GeV* carry information about the formation of a quark gluon phase and information about distribution of partons in the nuclei. Prompt photons are formed by rigid scattering of incoming partons, such as Compton scattering of $qg \rightarrow q\gamma$ or annihilation of $q\bar{q} \rightarrow g\gamma$, as well as the braking radiation of quarks that undergo severe scattering [3,4]. These processes are described by perturbative pQCD in the LO and NLO order that dominate LHC energies. One purpose of prompt photonic measurements is to improve the accuracy of such calculations in various collision systems. In RHIC at the center of mass at energy per nucleon-nucleon pair $\sqrt{s}=0.2$ *TeV* and at LHC at $\sqrt{s}=2.76$ *TeV*, it was found that prompt photons with transverse momentum (p_T) above about 3 and 15 *GeV/c* respectively dominate fast photons and follow the power law spectral form in small systems (pp , pA , dA) as well as in heavy ion collisions as described in pQCD.

Secondary photons can be formed in reactions by mesons formed by hadrons in a proton-proton collision [6-8]. Photoproduction from light and heavy nuclei is a very effective tool for studying the interactions of mesons with nuclear substances and the properties of hadrons. The study of the electromagnetic transitions of the nucleus into unstable resonances of excitation gives a are representation of the structure of the nucleus. Excited hadrons from base quark and gluon block carry information about quark-gluon plasma. Measurement of meson production reactions from quasi-free nucleons was much more systematic, in particular by studying in detail the nuclear effect on quasi-free proton sections, which can be compared with their free counter-cell sections [5,6].

We considered thermal photons productions in the processes: $\pi^+\pi^- \rightarrow \gamma\rho^0$, $\pi^\pm\rho^0 \rightarrow \gamma\pi^\pm$, $\rho^0 \rightarrow \gamma\pi^+\pi^-$, $\pi^+\pi^- \rightarrow \gamma\eta$, $\pi^\pm\eta \rightarrow \gamma\pi^\pm$, and $\pi^+\pi^- \rightarrow \gamma\gamma$. We constructed Feynman diagrams of these processes and wrote matrix elements. Calculation of the square of matrix elements are performed using FeynCalc. The dependencies of differential cross-section of processes on energy of colliding meson, transverse momentum of p_T and cosine of scattering angle of photons has been determined. The differential sections of the processes calculated without and taking into account the meson formfactor were compared.

I. DIFFERENTIAL CROSS-SECTIONS OF THE PROCESSES

$\pi^+\pi^- \rightarrow \gamma\rho^0$, $\pi^\pm\rho^0 \rightarrow \gamma\pi^\pm$, $\rho^0 \leftarrow \gamma + \pi^+ + \pi^-$,
 $\pi^+\pi^- \rightarrow \gamma\eta$, $\pi^\pm\eta \rightarrow \gamma\pi^\pm$, $\pi^+\pi^- \rightarrow \gamma\gamma$.

WITHOUT AND TAKING INTO ACCOUNT FORMFACTOR OF MESONS

- a. differential cross-section of processes without taking into account formfactor of mesons The complete matrix element (M_I) of process $\pi^+ \pi^- \rightarrow \gamma \rho^0$ consists of the sum of the
1. process $\pi^+ \pi^- \rightarrow \gamma \rho^0$ following matrix elements:

$$M_{11} = eg_s \varepsilon_\mu(k_1)(2p_1 - k_1)_\nu \frac{1}{(p_1 - k_1)^2 - m_\pi^2} (k_2 - 2p_2)_\mu \varepsilon_\nu(k_2)$$

$$M_{12} = eg_s \varepsilon_\mu(k_1)(k_1 - 2p_2)_\mu \frac{1}{(p_1 - k_2)^2 - m_\pi^2} (2p_1 - k_2)_\nu \varepsilon_\nu(k_2)$$

$$M_{13} = 2ieg_s g_{\mu\nu} \varepsilon_\mu(k_1) \varepsilon_\nu(k_2)$$

where k_1, k_2, p_1 and p_2 are momentums of photon, gluon, π^+ and π^- mesons correspondingly.

Mandelstam invariants of this process are: $s = (p_1 + p_2)^2 = (k_1 + k_2)^2$, $t = (p_1 - k_2)^2 = (p_2 - k_1)^2$, $u = (p_1 - k_1)^2 = (p_2 - k_2)^2$.

In the calculations, the product of polarization vectors was taken as follows:

photon: $\varepsilon_\mu(k_1) \varepsilon_{\mu'}^*(k_1) = -g_{\mu\mu'}$ ρ^0 meson: $\varepsilon_\nu(k_2) \varepsilon_{\nu'}^*(k_2) = -g_{\nu\nu'} + \frac{k_2^\nu \cdot k_2^{\nu'}}{m_\rho^2}$

The square of the matrix element M_I was calculated by FeynCalc at photon mass $m_\gamma=0$. The differential section of process was calculated by formula [7]:

$$\frac{d\sigma}{dt} = \frac{1}{16\pi s^2} \frac{p'_{cm}}{p_{cm}} |M_I|^2$$

where $|M_I|^2$ - square of matrix elements of the process and

$$(p_{cm})^2 = \frac{1}{4s} (s - (m_1 + m_2)^2) (s - (m_1 - m_2)^2), \quad (p'_{cm})^2 = \frac{1}{4s} (s - (m_3 + m_4)^2) (s - (m_3 - m_4)^2).$$

For process $\pi^+ + \pi^- \rightarrow \gamma + \rho^0$ masses are equal: $m_1=m_2=m_\pi$; $m_4=m_\rho$; $m_3=m_\gamma$. In estimating the differential section, Mandelstam invariants t and u were expressed through s and p_T as follows:

$$t = -\frac{s}{2}(1 - \cos(\vartheta)) + m_\rho^2 + m_\pi^2, \quad u = -\frac{s}{2}(1 + \cos(\vartheta)) + m_\rho^2 + m_\pi^2, \quad t = -p_T \sqrt{s} e^{-y},$$

$$u = -p_T \sqrt{s} e^y$$

Matrix elements of the process, taking into account the meson formfactor, are:

$$M_{11} = eg_s \varepsilon_\mu(k_1)(2p_1 - k_1)_\nu h_+(p_a) \frac{1}{(p_1 - k_1)^2 - m_\pi^2} (k_2 - 2p_2)_\mu \varepsilon_\nu(k_2)$$

$$M_{12} = eg_s \varepsilon_\mu(k_1)(k_1 - 2p_2)_\mu h_+(p_b) \frac{1}{(p_1 - k_2)^2 - m_\pi^2} (2p_1 - k_2)_\nu \varepsilon_\nu(k_2)$$

$$M_{13} = 2ieg_s a g_{\mu\nu} \varepsilon_\mu(k_1) \varepsilon_\nu(k_2)$$

where $h_+(p_a) = \frac{m_\rho^2 - m_\pi^2}{m_\rho^2 - p_a^2}$, $h_+(p_b) = \frac{m_\rho^2 - m_\pi^2}{m_\rho^2 - p_b^2}$, $a = h_+(p_a) + h_+(p_b)$, $p_a = p_1 - k_1 = k_2 - p_2$,

$$p_b = p_1 - k_2 = k_1 - p_2$$

2. process $\pi^\pm \rho^0 \rightarrow \gamma \pi^\pm$

The complete matrix element (M_2) of process $\pi^\pm \rho^0 \rightarrow \gamma \pi^\pm$ consists of the sum of the following matrix elements:

$$M_{21} = eg_s \varepsilon_\mu(k_1)(k_1 + 2p_2)_\mu \frac{1}{(p_1 + k_2)^2 - m_\pi^2} (k_2 + 2p_1)_\nu \varepsilon_\nu(k_2)$$

$$M_{22} = eg_s \varepsilon_\mu(k_1) (2p_1 - k_1)_\mu \frac{1}{(p_1 - k_1)^2 - m_\pi^2} (2p_2 - k_2)_\nu \varepsilon_\nu(k_2)$$

$$M_{23} = 2ieg_s g_{\mu\nu} \varepsilon_\mu(k_1) \varepsilon_\nu(k_2)$$

where k_1, k_2, p_1 and p_2 are momentums of photon, gluon, initial π^\pm and final π^\pm mesons correspondingly.

Mandelstam invariants of this process are: $s = (p_1 + p_2)^2 = (k_1 + k_2)^2$, $t = (p_1 - k_1)^2 = (p_2 - k_2)^2$, $u = (p_1 - k_2)^2 = (p_2 - k_1)^2$.

In the calculations, the product of the polarization vectors were taken as follows [13,14]. The square of the matrix element M_2 was calculated by FeynCalc at photon mass $m_\gamma=0$. Differential cross-section of process is calculated at: $m_1=m_4=m_\pi$, $m_2=m_\rho$; $m_3=m_\gamma$. In estimating the differential section, Mandelstam invariants t and u were expressed through s and p_T as follows:

$$t = -\frac{s}{2}(1 - \cos(\vartheta)) + m_\rho^2 + m_\pi^2, \quad u = -\frac{s}{2}(1 + \cos(\vartheta)) + m_\pi^2 + m_\pi^2, \quad t = -p_T \sqrt{s} e^{-y}, \quad u = -p_T \sqrt{s} e^y$$

Matrix elements of the process, taking into account the meson formfactor, are:

$$M_{21} = eg_s \varepsilon_\mu(k_1) (k_1 + 2p_2)_\mu h_+(p_a) \frac{1}{(p_1 + k_2)^2 - m_\pi^2} (k_2 + 2p_1)_\nu \varepsilon_\nu(k_2)$$

$$M_{22} = eg_s \varepsilon_\mu(k_1) (2p_1 - k_1)_\mu h_+(p_b) \frac{1}{(p_1 - k_1)^2 - m_\pi^2} (2p_2 - k_2)_\nu \varepsilon_\nu(k_2)$$

$$M_{23} = 2ieg_s a g_{\mu\nu} \varepsilon_\mu(k_1) \varepsilon_\nu(k_2)$$

where $h_+(p_a); h_+(p_b)$ and a have expression as (1), $p_a = p_1 + k_2 = p_2 + k_1$; $p_b = p_1 - k_1 = p_2 - k_2$.

3. process $\rho^0 \rightarrow \gamma + \pi^+ + \pi^-$

The complete matrix element (M_3) of process $\rho^0 \rightarrow \gamma + \pi^+ + \pi^-$ consists of the sum of the following matrix elements:

$$M_{31} = eg_s \varepsilon_\nu(k_2) (k_2 - 2p_2)_\nu \frac{1}{(p_1 + k_1) - m_\pi^2} (k_1 + 2p_1)_\mu \varepsilon_\mu(k_1)$$

$$M_{32} = eg_s \varepsilon_\nu(k_2) (k_2 - 2p_1)_\nu \frac{1}{(k_2 - p_1)^2 - m_\pi^2} (k_1 + 2p_2)_\mu \varepsilon_\mu(k_1)$$

$$M_{33} = 2ieg_s g_{\mu\nu} \varepsilon_\mu(k_1) \varepsilon_\nu(k_2)$$

where k_1, k_2, p_1 and p_2 are momentums of photon, gluon, π^+ and π^- mesons correspondingly.

Mandelstam invariants of this process are: $s = (p_2 + k_1)^2$, $t = (k_1 + p_1)^2$, $u = (p_1 + p_2)^2$.

In the calculations, the product of the polarization vectors were taken as follows [16,17]. The square of the matrix element M_1 was calculated by FeynCalc at photon mass $m_\gamma=0$. The differential cross-section of each process was calculated by formula [7]:

$$\frac{d\sigma}{dx_1 dx_2} = \frac{Q}{32(2\pi)^3} |M_3|^2$$

where $Q = \sqrt{k_2^2} = m_\rho$, $x_i = 2E_i/Q$ ($i = 1, 2, 3$)

In estimating the differential section, Mandelstam invariants t and u were expressed through s and p_T as follows:

$$t = -\frac{s}{2}(1 - \cos(\vartheta)) + m_\rho^2 + m_\pi^2, \quad u = -\frac{s}{2}(1 + \cos(\vartheta)) + m_\rho^2 + m_\pi^2, \quad t = -p_T \sqrt{s} e^{-y}, \quad u = -p_T \sqrt{s} e^y$$

Matrix elements of the process, taking into account the meson formfactor, are:

$$M_{31} = eg_s \varepsilon_\nu(k_2) (k_2 - 2p_2)_\nu h_+(p_a) \frac{1}{(p_1 + k_1) - m_\pi^2} (k_1 + 2p_1)_\mu \varepsilon_\mu(k_1)$$

$$M_{32} = eg_s \varepsilon_\nu(k_2) (k_2 - 2p_1)_\nu h_+(p_a) \frac{1}{(k_2 - p_1)^2 - m_\pi^2} (k_1 + 2p_2)_\mu \varepsilon_\mu(k_1)$$

$$M_{33} = 2ieg_s a g_{\mu\nu} \varepsilon_\mu(k_1) \varepsilon_\nu(k_2)$$

where $h_+(p_a); h_+(p_b)$ and a have expression as (1), $p_a = p_1 + k_1 = k_2 - p_2$; $p_b = k_2 - p_1 = p_2 + k_1$.

4. process $\pi^+ \pi^- \rightarrow \gamma \eta$

The complete matrix element (M_5) of process $\pi^+ \pi^- \rightarrow \gamma \eta$ consists of the sum of the following matrix elements:

$$M_{41} = eg_s \varepsilon_\mu(k_1) (2p_1 - k_1)_\nu \frac{1}{(p_1 - k_1)^2 - m_\pi^2} (k_2 - 2p_2)_\mu i\gamma_5(k_2)_\nu A$$

$$M_{42} = eg_s \varepsilon_\mu(k_1) (k_1 - 2p_2)_\mu \frac{1}{(p_1 - k_2)^2 - m_\pi^2} (2p_1 - k_2)_\nu i\gamma_5(k_2)_\nu A$$

$$M_{43} = 2ieg_s g_{\mu\nu} \varepsilon_\mu(k_1) i\gamma_5(k_2)_\nu A$$

where k_1, k_2 and p_1 and p_2 are momentums of photon, η, π^+ and π^- mesons correspondingly,

$$A = \lambda_u g_\pi \text{Sin}(\phi) + \lambda_s g_s \text{Cos}(\phi), \quad \lambda_u = \begin{pmatrix} 1 & 0 & 0 \\ 0 & 1 & 0 \\ 0 & 0 & 0 \end{pmatrix}, \quad \lambda_s = \begin{pmatrix} 1 & 0 & 0 \\ 0 & 1 & 0 \\ 0 & 0 & -\sqrt{2} \end{pmatrix}, \quad g_s=6,14, \quad g_\pi = \frac{m_u}{F_\pi}, \quad F_\pi=93$$

$M\partial B, \phi = 54^\circ$.

Mandelstam invariants of this process are: $s = (p_1 + p_2)^2 = (k_1 + k_2)^2$, $t = (p_1 - k_2)^2 = (p_2 - k_1)^2$,
 $u = (p_1 - k_1)^2 = (p_2 - k_2)^2$

In the calculations, the product of the polarization vectors were taken as follows: photon:
 $\varepsilon_\mu(k_1) \varepsilon_\mu^*(k_1) = -g_{\mu\mu}$

The square of the matrix element M_1 was calculated by FeynCalc at photon mass $m_\gamma=0$. For process $\pi^+ + \pi^- \rightarrow \gamma + \eta$ masses equal: $m_1=m_2=m_\pi$; $m_4=m_\eta$; $m_3=m_\gamma$. In estimating the differential section, Mandelstam invariants t and u were expressed through s and from p_T as follows:

$$t = -\frac{s}{2}(1 - \cos(\vartheta)) + m_\eta^2 + m_\pi^2, \quad u = -\frac{s}{2}(1 + \cos(\vartheta)) + m_\eta^2 + m_\pi^2, \quad t = -p_T \sqrt{s} e^{-y}, \quad u = -p_T \sqrt{s} e^y.$$

5. process $\pi^\pm \eta \rightarrow \gamma \pi^\pm$

The complete matrix element (M_6) of process $\pi^\pm \eta \rightarrow \gamma \pi^\pm$ consists of the sum of the following matrix elements:

$$M_{51} = eg_s \varepsilon_\mu(k_1) (k_1 + 2p_2)_\mu \frac{1}{(p_1 + k_2)^2 - m_\pi^2} (k_2 + 2p_1)_\nu i\gamma_5(k_2)_\nu A$$

$$M_{52} = eg_s \varepsilon_\mu(k_1) (2p_1 - k_1)_\mu \frac{1}{(p_1 - k_1)^2 - m_\pi^2} (2p_2 - k_2)_\nu i\gamma_5(k_2)_\nu A$$

$$M_{53} = 2ieg_s g_{\mu\nu} \varepsilon_\mu(k_1) i\gamma_5(k_2)_\nu A$$

where k_1, k_2 and p_1 and p_2 are momentums of photon, η , initial π^\pm and final π^\pm mesons correspondingly,

$$A = \lambda_u g_\pi \text{Sin}(\phi) + \lambda_s g_s \text{Cos}(\phi), \quad \lambda_u = \begin{pmatrix} 1 & 0 & 0 \\ 0 & 1 & 0 \\ 0 & 0 & 0 \end{pmatrix}, \quad \lambda_s = \begin{pmatrix} 1 & 0 & 0 \\ 0 & 1 & 0 \\ 0 & 0 & -\sqrt{2} \end{pmatrix}, \quad g_s=6,14, \quad g_\pi = \frac{m_u}{F_\pi}, \quad F_\pi=93$$

$MeB, \phi = 54^\circ$.

Mandelstam invariants of this process are: $s = (p_1 + p_2)^2 = (k_1 + k_2)^2$, $t = (p_1 - k_1)^2 = (p_2 - k_2)^2$
and $u = (p_1 - k_2)^2 = (p_2 - k_1)^2$.

In the calculations, the product of polarization vectors was taken as follows: for photon: $\varepsilon_\mu(k_1)\varepsilon_\mu^*(k_1) = -g_{\mu\mu'}$

The square of the matrix element M_5 was calculated by FeynCalc and at photon mass $m_\gamma=0$ it is equal. The differential cross-section of the process was calculated by the formula [9]:

$$\frac{d\sigma}{dt} = \frac{1}{16\pi s^2} \frac{p'_{cm}}{p_{cm}} |M_5|^2$$

Here $(p_{cm})^2 = \frac{1}{4s} (s - (m_1 + m_2)^2) (s - (m_1 - m_2)^2)$ и $(p'_{cm})^2 = \frac{1}{4s} (s - (m_3 + m_4)^2) (s - (m_3 - m_4)^2)$

For process $\pi^\pm + \eta \rightarrow \gamma + \pi^\pm$ masses equal: $m_1=m_4=m_\pi; m_2=m_\eta; m_3=m_\gamma$

In estimating the differential section, Mandelstam invariants t and u were expressed through s and from p_T as follows:

$$t = -\frac{s}{2}(1 - \cos(\vartheta)) + m_\eta^2 + m_\pi^2, \quad u = -\frac{s}{2}(1 + \cos(\vartheta)) + m_\pi^2 + m_\pi^2, \quad t = -p_T \sqrt{s} e^{-y}, \quad u = -p_T \sqrt{s} e^y.$$

6. process $\pi^+ \pi^- \rightarrow \gamma\gamma$

The complete matrix element (M_6) of process $\pi^+ \pi^- \rightarrow \gamma\gamma$ consists of the sum of the following matrix elements:

$$M_{61} = e^2 \varepsilon_\mu(k_1) (2p_1 - k_1)_\nu \frac{1}{(p_1 - k_1)^2 - m_\pi^2} (k_2 - 2p_2)_\mu \varepsilon_\nu(k_2)$$

$$M_{62} = e^2 \varepsilon_\mu(k_1) (k_1 - 2p_2)_\mu \frac{1}{(p_1 - k_2)^2 - m_\pi^2} (2p_1 - k_2)_\nu \varepsilon_\nu(k_2)$$

$$M_{63} = -2e^2 g_{\mu\nu} \varepsilon_\mu(k_1) \varepsilon_\nu(k_2)$$

where k_1, k_2 and p_1 and p_2 are momentums of initial photon, final photon, initial π^+ and final π^- mesons, correspondingly,

$$A = \lambda_u g_\pi \sin(\phi) + \lambda_s g_s \cos(\phi), \quad \lambda_u = \begin{pmatrix} 1 & 0 & 0 \\ 0 & 1 & 0 \\ 0 & 0 & 0 \end{pmatrix}, \quad \lambda_s = \begin{pmatrix} 1 & 0 & 0 \\ 0 & 1 & 0 \\ 0 & 0 & -\sqrt{2} \end{pmatrix}, \quad g_s = 6, 14, \quad g_\pi = \frac{m_u}{F_\pi}, \quad F_\pi = 93$$

$M \rightarrow B, \phi = 54^\circ$.

Mandelstam invariants of this process are: $s = (p_1 + p_2)^2 = (k_1 + k_2)^2, t = (p_1 - k_2)^2 = (p_2 - k_1)^2, u = (p_1 - k_1)^2 = (p_2 - k_2)^2$. In the calculations, the product of polarization vectors was taken as follows for photon: $\varepsilon_\mu(k_1)\varepsilon_\mu^*(k_1) = -g_{\mu\mu'}$. The square of the matrix element M_6 was calculated by FeynCalc at photon mass $m_\gamma=0$. The differential cross-section of the process was calculated by the formula [7]:

$$\frac{d\sigma}{dt} = \frac{1}{16\pi s^2} \frac{p'_{cm}}{p_{cm}} |M_6|^2$$

here $(p_{cm})^2 = \frac{1}{4s} (s - (m_1 + m_2)^2) (s - (m_1 - m_2)^2)$ and $(p'_{cm})^2 = \frac{1}{4s} (s - (m_3 + m_4)^2) (s - (m_3 - m_4)^2)$.

For process $\pi^+ + \pi^- \rightarrow \gamma + \gamma$ mass equal: $m_1=m_2=m_\pi; m_3= m_4=m_\gamma$

In estimating the differential section, Mandelstam invariants t and u were expressed through s and from p_T as follows:

$$t = -\frac{s}{2}(1 - \cos(\vartheta)) + m_\pi^2, \quad u = -\frac{s}{2}(1 + \cos(\vartheta)) + m_\pi^2, \quad t = -p_T \sqrt{s} e^{-y}, \quad u = -p_T \sqrt{s} e^y.$$

III. RESULTS OF NUMERICAL CALCULATIONS AND THEIR DISCUSSION

a. the dependencies of differential cross-section of processes on energy colliding mesons, transverse momentum p_T , cosine of the scattering angle of photons and formfactor of mesons

1. process $\pi^+\pi^- \rightarrow \gamma\rho^0$

In the fig.1(a,b,c) are represents the dependence of differential cross-section of photon production $\pi^+\pi^- \rightarrow \gamma\rho^0$ process, calculated without and taking into account formfactor of mesons on energy colliding mesons \sqrt{s} , on the transverse momentum p_T and on cosine of scattering angle of photon.

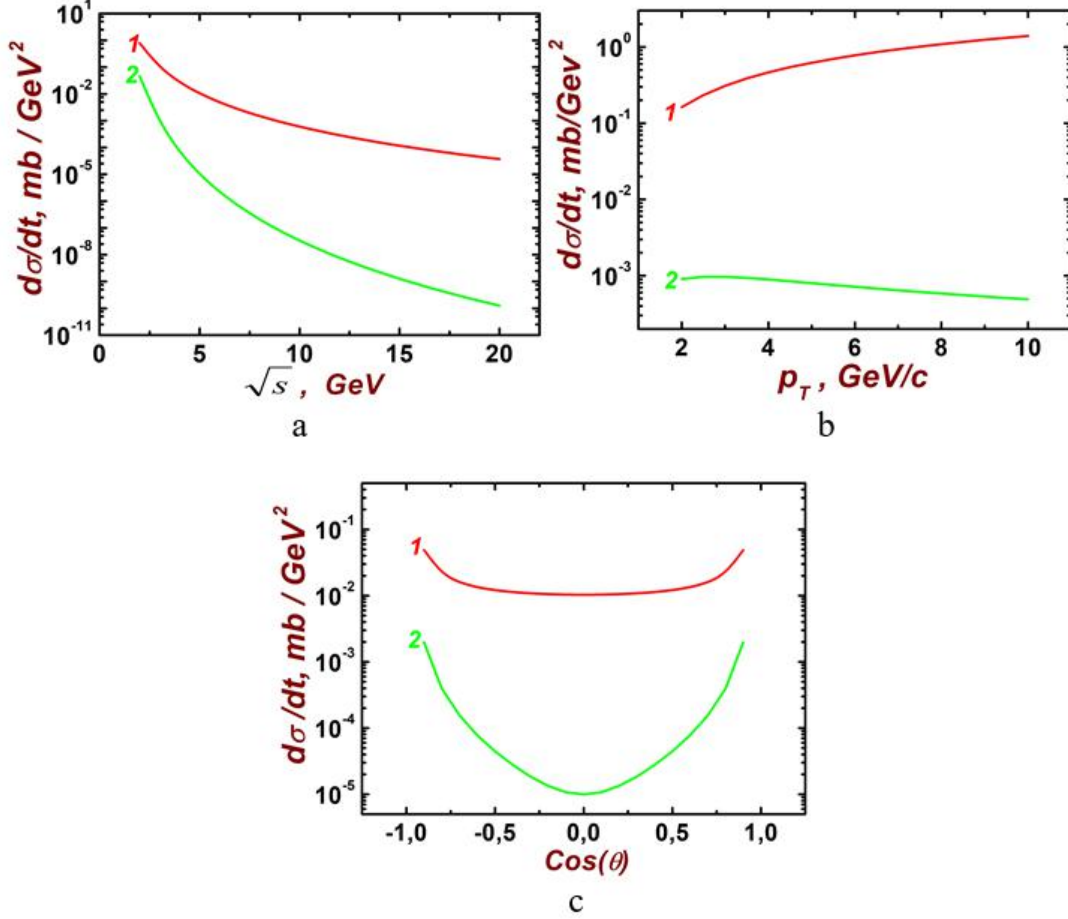


Fig. 1. (a,b,c) The dependence of differential cross-section of photon production $\pi^+\pi^- \rightarrow \gamma\rho^0$ process calculated without (curve 1) and taking into account formfactor of mesons (curve 2) on energy of colliding mesons \sqrt{s} (a), on transverse momentum p_T (b), on cosine of scattering angle of photon calculated (c) calculated without and taking into account formfactor of mesons curves 1 and 2, correspondingly.

As see from fig.1(a) the differential cross-section of processes decrease with increasing of energy of colliding π mesons. Lorentz conversion of the size of colliding particles shows that at high energies colliding particles have the shape of a disk, this in turn reduces the likelihood of colliding of constituent particles. Particles pass through each other without interaction of components. Therefore, the differential collision section is small at high energies than at low collision energies.

Differential cross-section of process increase with increasing transverse momentum p_T and at values of $p_T > 5$ GeV/c dependence to reach plateau (fig.1(b)).

As see from fig.1(c) the dependence differential cross-section of process on cosine of scattering angle of photon is symmetric relative to point $\text{Cos}(\theta)=0$ and have big value at $\text{Cos}(\theta)=\pm 1$.

The dependence differential cross-section on cosine of scattering angle of photon have minimum at $\text{Cos}(\theta)=0$ and maximums at $\text{Cos}(\theta)=\pm 1$.

Influence formfactor of meson to differential cross-section of process is significant at high values of energies of colliding mesons and transverse momentum.

The ratio of dependencies of differential cross-section on energy of colliding mesons, transverse momentum and cosine of scattering angle has been investigated. The ratio of dependencies of differential cross-sections on energy of colliding meson and ratio of dependencies of the differential cross-section on momentum p_T calculated without and taking into account the formfactor the meson is significant at large energy values of colliding mesons and transverse momentum. As ratio of $R_{II} > 1$ in all values of energy \sqrt{s} and transverse momentum p_T means

$$\frac{d\sigma_1(\pi^+\pi^-\rightarrow\gamma\rho^0)}{dt} > \frac{d\sigma_{1f}(\pi^+\pi^-\rightarrow\gamma\rho^0)}{dt} \text{ Ratio}$$

of dependencies of differential cross-sections of meson of process $\pi^+\pi^-\rightarrow\gamma\rho^0$ on cosine of scattering angle of photons calculated without and taking into account formfactor has symmetrical form relative to $\text{Cos}(\theta)=0$. It has a maximum at $\text{Cos}(\theta)=0$ and with an increase in the absolute value of the cosine of the angle of scattering of photons decreases (fig.3(c)). Taking into account the formfactor of meson in the dependence of the differential cross-section on the cosine of the scattering angle has a

large effect at small values of the cosine of the angle and a small effect at the $\text{Cos}(\theta)=\pm 1$.

2. process $\pi^\pm\rho^0\rightarrow\gamma\pi^\pm$

In the fig.2(a,b,c) represent the dependence of the differential cross-section of $\pi^\pm\rho^0\rightarrow\gamma\pi^\pm$ process on energy of colliding mesons, the transverse momentum p_T , and on the cosine of the angle of the scattering photon calculated (c) without and taking into account of formfactor of mesons.

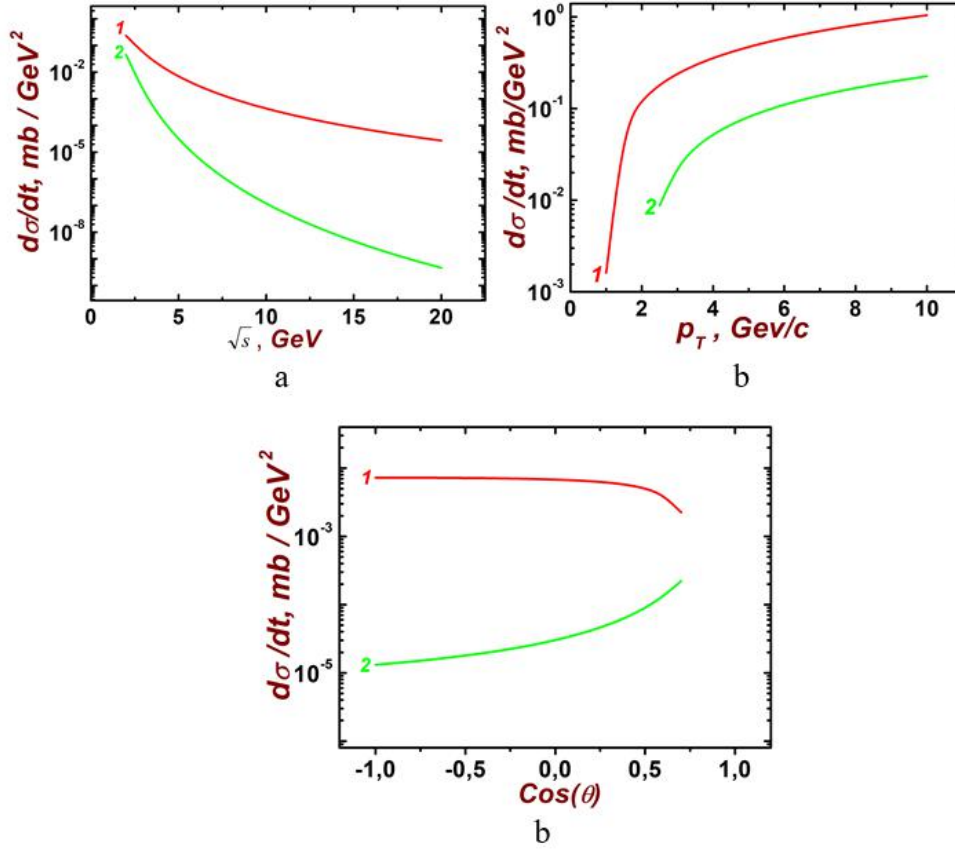


Fig.2. (a,b,c) dependence of the differential cross-section of $\pi^\pm\rho^0\rightarrow\gamma\pi^\pm$ process on energy of colliding mesons (a) and on the transverse momentum p_T (b), on the cosine of the scattering angle of the photon (c) calculated without and taking into account formfactor of mesons curves 1 and 2, correspondingly.

As can be seen from fig.2(b), the dependence of the differential cross-section on p_T is increased with increasing transverse momentum and at big values of p_T reach saturation. The dependence of the differential cross-section on the cosine of the scattering angle of photon in the interval $[-1, 0.4]$ is practically constant and in the interval $(0.4, 1]$ decreases sharply fig.3(c). Differential cross-section of process decrease with increasing transverse momentum p_T .

Differential cross-section of process decrease with increasing of energy of colliding mesons (fig.6(a)). Differential cross-section decrease with increasing transverse momentum p_T . Differential cross-section of process increase with increasing with cosine

of scattering angle of photon. Differential cross-section of process have minimum at $\text{Cos}(\theta)=-1$ and maximums at $\text{Cos}(\theta)=+1$. The dependence of differential cross-section of process on cosine of scattering angle of photon dependet on energy of colliding mesons and decrease with increasing of energy of mesons.

As ratio of $R_{1f} > 1$ in all values of energy \sqrt{s} and transverse momentum p_T means

$$\frac{d\sigma_1(\pi^\pm\rho^0\rightarrow\gamma\pi^\pm)}{dt} > \frac{d\sigma_{1f}(\pi^\pm\rho^0\rightarrow\gamma\pi^\pm)}{dt}$$

Ratio of differential cross-section on energy of colliding mesons decrease with increasing of energy.

Differential cross-section decrease with increasing cosine of scattering angle of photon.

3. process $\rho^0 \rightarrow \gamma\pi^+\pi^-$

Fig.3(a,b) represent the dependence of the differential cross-section $\rho^0 \rightarrow \gamma\pi^+\pi^-$ process on the

energy of colliding mesons, on transverse momentum p_T , and the on the cosine of scattering angle of the photon calculated at the energies of colliding mesons 5 and 10 GeV.

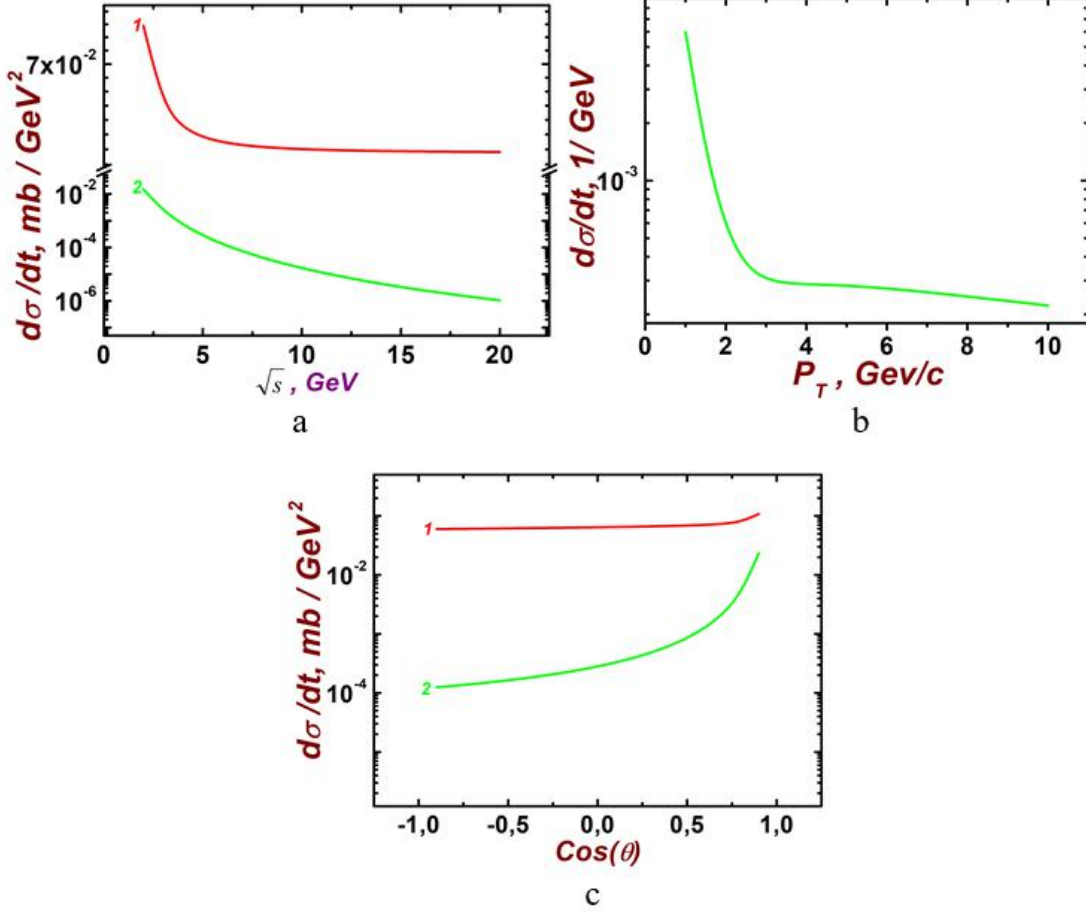


Fig.3. (a,b,c) the dependence of the differential cross section of $\rho^0 \rightarrow \gamma\pi^+\pi^-$ process on energy of colliding mesons (a), on the transverse momentum p_T (b), and on the cosine of the scattering angle of photon calculated without and taking into account formfactor of mesons curves 1 and 2, correspondingly (c).

As see from fig.3(b) the differential cross-section of process $\rho^0 \rightarrow \gamma\pi^+\pi^-$ is decreased with increasing of energy of colliding mesons. Differential cross-section of process $\rho^0 \rightarrow \gamma\pi^+\pi^-$ is decreased with increasing transverse momentum p_T . Differential cross-section of process $\rho^0 \rightarrow \gamma\pi^+\pi^-$ is decreased with increasing with increasing of the cosine of scattering angle of photon.

4. process $\pi^+\pi^- \rightarrow \gamma\eta$

Fig.4(a,b,c) represent the dependence of the differential cross-section of process $\pi^+\pi^- \rightarrow \gamma\eta$

on energy colliding mesons, on transverse momentum, and cosine of angle of scattering of photon calculated at the energies of colliding mesons 5 and 10 GeV.

As see from fig.4(b) the differential cross-section of process $\pi^+\pi^- \rightarrow \gamma\eta$ is decreased with increasing of energy of colliding mesons. Differential cross-section of process $\pi^+\pi^- \rightarrow \gamma\eta$ is decreased with increasing transverse momentum p_T . Differential cross-section of process $\pi^+\pi^- \rightarrow \gamma\eta$ does not depend on the cosine of scattering angle of photon.

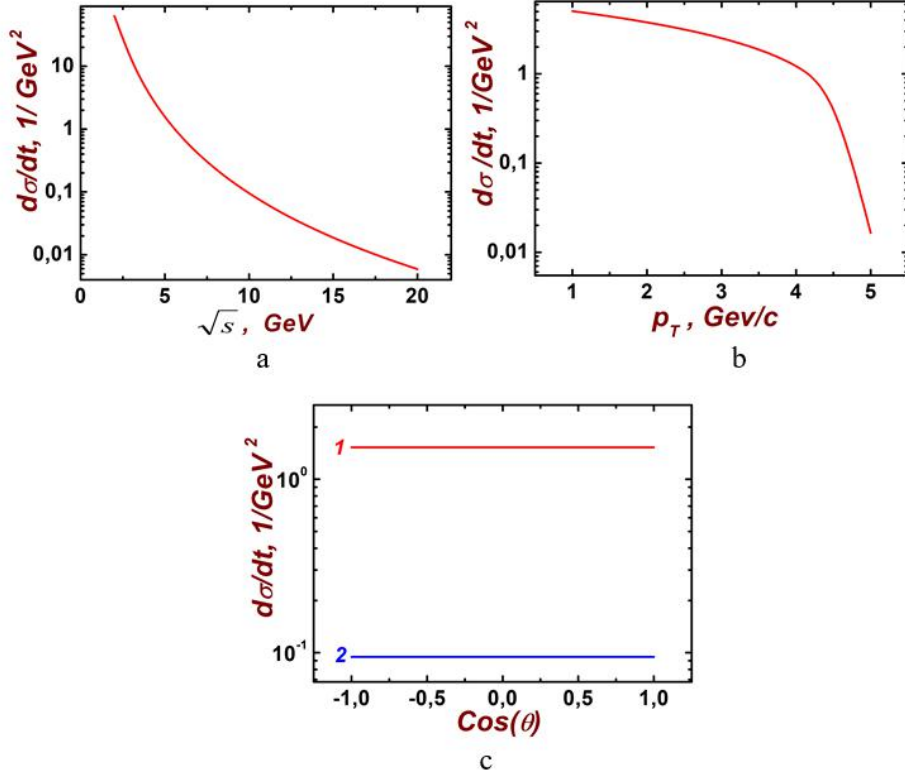


Fig.4. (a,b,c) The dependence of the differential cross-section of process $\pi^+\pi^-\rightarrow\gamma\eta$ on energy colliding mesons (a), on transverse momentum p_T (b), and cosine of angle of scattering of photon (c) calculated at energies of colliding mesons 5 and 10 GeV curves 1 and 2, correspondingly (c).

5. process $\pi^\pm\eta\rightarrow\gamma\pi^\pm$

Fig.5(a,b,c) represent the dependence of the differential cross section of process $\pi^\pm\eta\rightarrow\gamma\pi^\pm$ on the energy of colliding mesons, on transverse momentum p_T and cosine of scattering angle of photon, calculated at energies of colliding mesons 5 and 10 GeV curves 1 and 2, correspondingly.

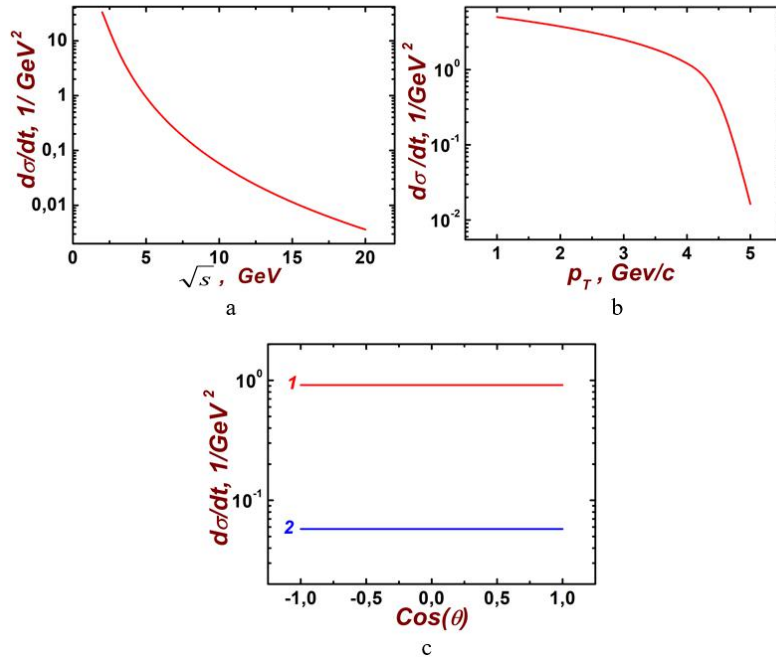


Fig. 5. (a,b,c) The dependence of the differential cross section $\pi^\pm\eta\rightarrow\gamma\pi^\pm$ process on tenergy of colliding mesons (a), on the transverse momentum p_T (b) and cosine of scattering angle of γ photon (c) calculated at energies of colliding mesons 5 and 10 GeV curves 1 and 2, correspondingly.

As see from fig.5(b) the differential cross-section of process $\pi^\pm\eta \rightarrow \gamma\pi^\pm$ is decreased with increasing of energy of colliding mesons. Differential cross-section of process $\pi^\pm\eta \rightarrow \gamma\pi^\pm$ is decreased with increasing transverse momentum p_T . Differential cross-section of process $\pi^\pm\eta \rightarrow \gamma\pi^\pm$ does not depend on the cosine of scattering angle of photon.

6. process $\pi^+\pi^- \rightarrow \gamma\gamma$

Fig.6(a,b,c) represent the dependencies of the differential cross-section of $\pi^+\pi^- \rightarrow \gamma\gamma$ process on the energy of colliding mesons, transverse momentum p_T , and on the cosine of scattering angle of photon, calculated at energies 5 and 10 GeV.

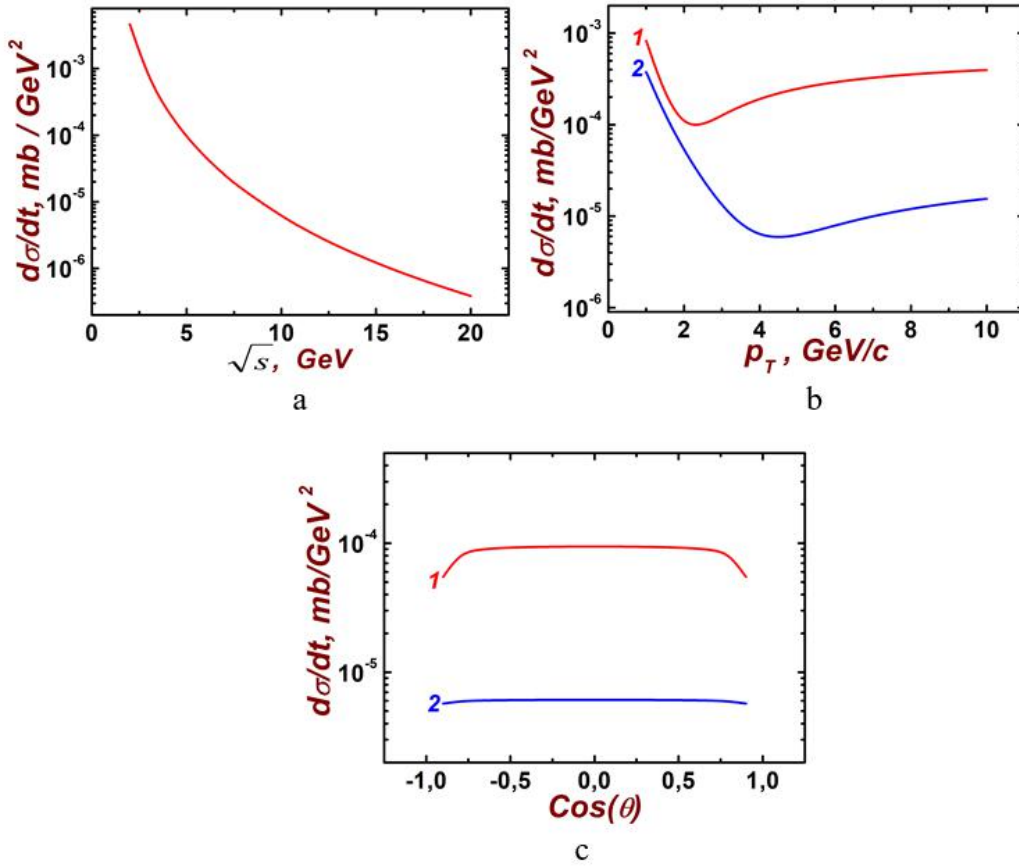


Fig.6. (a,b,c) the differential cross-section of $\pi^+\pi^- \rightarrow \gamma\gamma$ process on energy of colliding mesons (a), on the transverse momentum p_T (b), and on the cosine of the scattering angle of photon (c), calculated at energies 5 and 10 GeV.

CONCLUSIONS

It is shown that the differential cross-section of all investigated processes decreased with increasing of energy of colliding protons. The dependencies of differential cross-sections of process on transverse momentum, cosine of scattering angle of photon depend on energy of colliding mesons. The dependencies of differential cross-sections of processes decrease with increasing of energy of

The differential cross-section of process decreased with increasing of energy of colliding mesons. The dependence of differential cross-section of $\pi^+\pi^- \rightarrow \gamma\gamma$ have minimum at p_T 2.2 GeV/c and at taking into account formfactor of meson it shift to big values of p_T . The dependence of differential cross-section on cosine of scattering angle of photon in the big interval practically is constant and sharply decreases at $Cos(\theta) = \pm 1$.

The dependence differential cross-section on transverse momentum and cosine of scattering angle of photon decreases with increasing of energy of colliding mesons.

colliding mesons.

The dependence of differential cross-section on cosine of scattering angle of photons is different.

The dependence of differential cross-section of processes $\pi^+\pi^- \rightarrow \gamma\rho^0$, $\rho^0 \rightarrow \gamma\pi^+\pi^-$ and $\pi^+\pi^- \rightarrow \gamma\eta$ on cosine of the angle of scattering photons is symmetric relative to 0 and it increases with the cosine of the angle in the intervals [-1, 0) and (0, 1].

The differential cross-section of process $\pi^\pm \rho^0 \rightarrow \gamma \pi^\pm$ has a maximum at -1 cosine of the scattering angle of photons and decreases with increasing cosine of the angle scattering photons.

The differential cross-section of process $\pi^\pm \eta \rightarrow \gamma \pi^\pm$ does not depend on cosine of the angle scattering photons. It is shown that accounting of the formfactor of mesons reduces of differential cross-section of processes.

The dependence of differential cross-section on the energy of the colliding mesons calculated taking into account the formfactor of meson has lower values than without taking into account the formfactor. The

meson formfactor has a small contribution to the differential cross-section at large energies of colliding mesons. Influence formfactor of meson to differential cross-section of process depend on energy of colliding mesons. Influence of formfactor of mesons to differential cross-section of process decreased with increasing energy of colliding mesons.

All mathematical calculations were performed in Mathematica 10 and FeynCalc. Feynman diagrams are constructed using JaxoDraw 2. The graphs are constructed using the Origin 9 program and edited using the Adobe Photoshop 8 graphics editor.

-
- [1] *P. Aurenche, R. Baier, M. Fontannaz.* Phys.Rev. D 42, 1440 (1990). DOI:<https://doi.org/10.1103>.
- [2] *T. Becher, C. Lorentzen, M.D. Schwartz.* Phys. Rev. D 86, 054026 (2012). <https://doi.org/10.1103/PhysRevD.86.054026>, arXiv:1206.6115 [hep-ph].
- [3] <https://doi.org/10.48550/arXiv.1206.6115>.
- [4] *J. Kapusta, P Lichard, D Seibert.* High energy photons from quark-gluon plasma versus hot hadronic gas. Nuclear Physics A 544, 1992, 485.
- [5] *J. Kapusta, P. Lichard, D. Seibert.* High-energy photons from quark-gluon plasma versus hot hadronic gas. Phys.Rev. D 44, 2774 (1991).
- [6] *P. Arnold, G.D. Moore, L.G. Yaffe.* Photon emission from ultrarelativistic plasmas. JHEP 11, 2011, 057.
- [7] *B. Krusche1.* Photoproduction of mesons off nuclei Electromagnetic excitations of the neutron and meson-nucleus interactions. arXiv:1110.0192v1 [nucl-ex] 2 Oct (2011).
- [8] *E. Byckling, K. Kajantie.* John Wiley and Sons, London, New York, Sydney, Toronto, 1973.

Received: 14.12.2022

PRODUCTION OF A HIGGS-BOSON PAIR IN e^-e^+ -COLLISIONS (II)

S.K. ABDULLAYEV, M.Sh. GOJAYEV

*Baku State University, Azerbaijan,
AZ 1148, Baku, st. Z. Khalilova, 23, m_qocayev@mail.ru*

Within the framework of the Standard Model and taking into account arbitrary polarizations of the electron-positron pair, the differential cross section of the process $e^-e^+ \rightarrow ZHH$ is calculated taking into account all Feynman diagrams. The characteristic features in the behavior of the cross section and polarization characteristics (left-right spin asymmetry, transverse spin asymmetry) depending on the angles of departure and the energies of the particles are investigated and revealed.

Keywords: Standard model, electron-positron pair, Higgs boson pair, left-right spin asymmetry, transverse spin asymmetry.
PACS: 13.66.Fg, 14.70.Hp, 14.80.Bn.

1. INTRODUCTION

The Standard Model (SM), based on local gauge symmetry $SU_C(3) \times SU_L(2) \times U_Y(1)$, satisfactorily describes the physics of strong and electroweak interactions of quarks, leptons and gauge bosons [1-3]. A doublet of scalar fields $\varphi = \begin{pmatrix} \varphi^+ \\ \varphi^0 \end{pmatrix}$ is introduced into the theory, the neutral component of which has a vacuum value other than zero. As a result of spontaneous symmetry breaking due to quantum excitations of the scalar field, a Higgs boson H appears, and due to interaction with this field, charged leptons, quarks and gauge bosons W^\pm and Z^0 acquire mass. This mechanism of particle mass generation is known as the mechanism of spontaneous violation of the Brauth-Englert-Higgs symmetry.

The discovery of the Higgs boson with characteristics corresponding to SM predictions was carried out by ATLAS and CMS collations in 2012 at the Large Hadron Collider (LHC) at CERN [4, 5] (see also reviews [6-8]). With the discovery of the Higgs boson H with a mass of about 125 GeV, the missing particle in SM was found, and this began a new period in the study of the properties of fundamental interactions. In this regard, theoretical and experimental interest in various channels of the Higgs boson production and decay has greatly increased.

Due to the rather strong connection of the Higgs boson with vector Z - and W -bosons, the main sources of the production of Higgs bosons are the radiation of their Z - and W -bosons born in various experiments. A particularly intense source of Higgs bosons could be the processes occurring in electron-positron collisions. Note that collisions of high-energy electrons and positrons are an effective method for studying the mechanisms of interaction of elementary particles. This is due to the following circumstances. Firstly, the interaction of an electron-positron pair is described in SM, so the results obtained are well in-

terpreted. Secondly, since the electron-positron pair does not participate in strong interactions, the background conditions of experiments are significantly improved compared to the studies conducted in the LHC with proton-proton beams. Note that high-energy electron-positron colliders have either been designed or are scheduled to be designed in various laboratories around the world [9, 10].

The process of the Higgs boson generation in electron-positron collisions $e^-e^+ \rightarrow ZH$ is considered in a number of papers [2, 11-14]. Here we consider the process of the generation of the Higgs boson of a pair in arbitrarily polarized electron-positron collisions

$$e^- + e^+ \rightarrow Z^* \rightarrow Z + H + H, \quad (1)$$

where Z^* is the virtual Z -boson. In the case of an unpolarized electron-positron pair, this process is considered in [2, 15, 16].

An analytical expression for the differential effective cross section of the reaction (1) is obtained within the SM and taking into account arbitrary polarizations of the electron-positron pair. Left-right and transverse spin asymmetries due to the polarizations of the electron-positron pair are determined. The dependence of the asymmetries and the effective cross-section of the process on the departure angles and particle energies is studied in detail.

2. CALCULATION OF DIAGRAMS c) AND d)

The process $e^-e^+ \rightarrow ZHH$ is described by Feynman diagrams shown in Fig. 1 (4-particle momentums are written in parentheses). The calculation of diagrams a) and b) was carried out in the first part of this work [17]. Calculations of diagrams c) and d), as well as interference of all diagrams, are also carried out here.

The amplitude corresponding to diagram b) can be written as:

$$M_c = g_{Zee} g_{ZZH}^2 \ell_\mu D_{\mu\nu}(p) D_{\nu\rho}(q) U_\rho^*(k), \quad (2)$$

PRODUCTION OF A HIGGS-BOSONPAIR IN e^-e^+ -COLLISIONS (II)

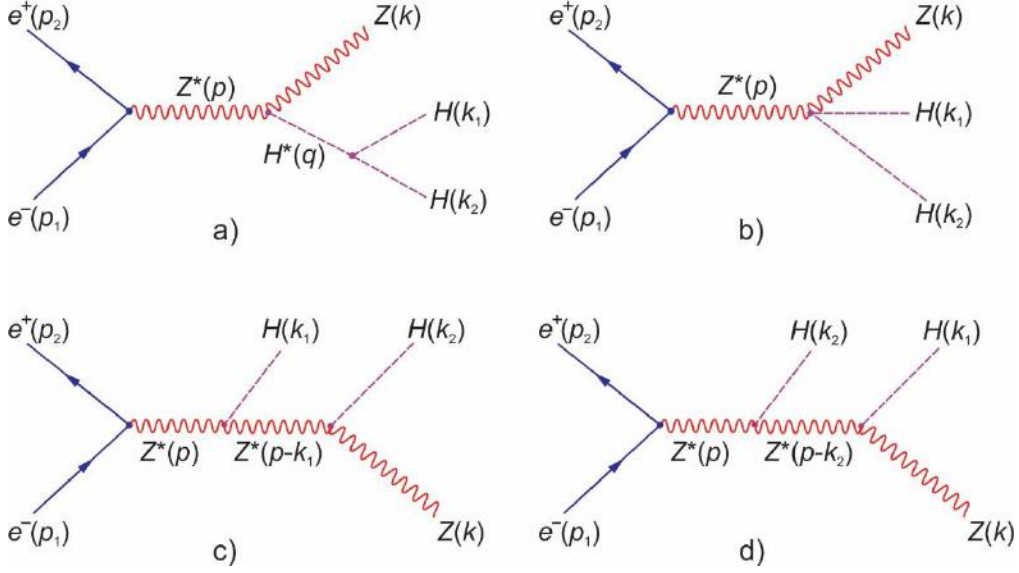


Fig. 1. Feynman diagrams of process $e^-e^+ \rightarrow ZHH$

where

$$\ell_\mu = \bar{v}(p_2, s_2) \gamma_\mu [g_L(1 + \gamma_5) + g_R(1 - \gamma_5)] u(p_1, s_1) \quad (3)$$

– electron-positron weak neutral current; s_1 and s_2 4-polarization vectors of electron and positron; g_L and g_R – left and right electron Z -boson coupling constants.

$$g_L = -\frac{1}{2} + x_W, \quad g_R = x_W; \quad (4)$$

$x_W = \sin^2 \theta_W$ – Weinberg parameter (θ_W – Weinberg angle);

$$g_{Zee} = (\sqrt{2}G_F)^{1/2} M_Z, \quad g_{ZZH} = 2(\sqrt{2}G_F)^{1/2} M_Z^2 \quad (5)$$

– constants of electron- Z -boson and Higgs boson- Z -boson interactions; $D_{\mu\nu}(p)$ and $D_{\nu\rho}(q)$ are vector Z -boson propagators

$$D_{\mu\nu}(p) = i \left(-g_{\mu\nu} + \frac{p_\mu p_\nu}{M_Z^2} \right) \cdot \frac{1}{p^2 - M_Z^2},$$

M_Z – the mass of the Z -boson; G_F – the Fermi constant of weak interactions; $p = p_1 + p_2$ and $q = p - k_1 = k + k_2$ – the total 4-momenta of the electron-positron pair and the Z -Higgs boson system; $U_\rho^*(k)$ – the 4-polarization vector of the vector Z -boson.

At high energies of the electron-positron pair ($\sqrt{s} \gg m$, \sqrt{s} – the total energy of the e^-e^+ -pair in the center-of-mass system, m – the mass of the electron), a weak electron current is preserved

$$p_\mu \ell_\mu = (p_1 + p_2)_\mu \ell_\mu = 0,$$

as a result, the amplitude (2) is greatly simplified:

$$M_c = g_{Zee} g_{ZZH}^2 \cdot \frac{1}{s(1-r_Z)} \cdot \frac{1}{s(y_1 + r_H - r_Z)} \cdot \ell_\nu \cdot \left(g_{\nu\rho} - \frac{q_\nu q_\rho}{M_Z^2} \right) U_\rho^*(k). \quad (6)$$

For the modulus of the square of the matrix element (6), the expression is obtained:

$$|M_c|^2 = \frac{g_{Zee}^2}{s^2(1-r_Z)^2} \frac{g_{ZZH}^4}{s^2(y_1+r_H-r_Z)^2} L_{\mu\nu} \left(g_{\mu\sigma} - \frac{q_\mu q_\sigma}{M_Z^2} \right) \cdot \left(g_{\nu\rho} - \frac{q_\nu q_\rho}{M_Z^2} \right) \cdot \left(-g_{\rho\sigma} + \frac{k_\rho k_\sigma}{M_Z^2} \right). \quad (7)$$

Here $L_{\mu\nu} = \ell_\mu \bar{\ell}_\nu$ is the electron-positron tensor

$$\begin{aligned} L_{\mu\nu} = & 2(g_L^2 + g_R^2)[p_{1\mu}p_{2\nu} + p_{2\mu}p_{1\nu} - (p_1 \cdot p_2)g_{\mu\nu} - m^2(s_{1\mu}s_{2\nu} + s_{2\mu}s_{1\nu} - (s_1 \cdot s_2)g_{\mu\nu})] + \\ & + 2(g_L^2 - g_R^2)m[p_{1\mu}s_{2\nu} + p_{1\nu}s_{2\mu} - (p_1 \cdot s_2)g_{\mu\nu} - s_{1\mu}p_{2\nu} - s_{1\nu}p_{2\mu} + (p_2 \cdot s_1)g_{\mu\nu}] + \\ & + 4g_L g_R [(p_1 \cdot s_2)(s_{1\mu}p_{2\nu} + s_{1\nu}p_{2\mu} - (s_1 \cdot p_2)g_{\mu\nu}) + (p_2 \cdot s_1)(p_{1\mu}s_{2\nu} + p_{1\nu}s_{2\mu}) - \\ & - (p_1 \cdot p_2)(s_{1\mu}s_{2\nu} + s_{2\mu}s_{1\nu} - (s_1 \cdot s_2)g_{\mu\nu}) - (s_1 \cdot s_2)(p_{1\mu}p_{2\nu} + p_{2\mu}p_{1\nu})]. \end{aligned} \quad (8)$$

In formula (7), the tensor

$$\sum_{\text{pol.}} U_\rho^*(k) U_\sigma(k) = -g_{\rho\sigma} + \frac{k_\rho k_\sigma}{M_Z^2}$$

it arose due to the summation of the vector Z -boson by polarization states.

Due to the cumbersomeness of the expression, the product of the electron $L_{\mu\nu}$ and Z -boson tensors

$$\begin{aligned} & L_{\mu\nu} \left(g_{\mu\sigma} - \frac{q_\mu q_\sigma}{M_Z^2} \right) \cdot \left(g_{\nu\rho} - \frac{q_\nu q_\rho}{M_Z^2} \right) \cdot \left(-g_{\rho\sigma} + \frac{k_\rho k_\sigma}{M_Z^2} \right) = \\ & = L_{\mu\nu} \left[-g_{\mu\nu} + \frac{k_\mu k_\nu}{M_Z^2} + \frac{k_{1\mu} k_{1\nu}}{M_Z^2} \left(2 - \frac{y_1 + r_H}{r_Z} + \frac{(y_1 + r_Z)^2}{4r_Z^2} \right) + \frac{k_\mu k_{1\nu} + k_\nu k_{1\mu}}{M_Z^2} \cdot \frac{y_1 + r_Z}{2r_Z} \right], \end{aligned}$$

it is not given here, we have introduced the notation:

$$r_Z = \left(\frac{M_Z}{\sqrt{s}} \right)^2, \quad r_H = \left(\frac{M_H}{\sqrt{s}} \right)^2, \quad y_1 = 1 - x_1, \quad x_1 = \frac{2E_1}{\sqrt{s}},$$

E_1 – the energy of the Higgs boson with 4-momentum k_1 .

The differential effective cross section of the reaction $e^- e^+ \rightarrow ZHH$ corresponding to diagram b) of Fig. 1 is expressed by the formula ($e^- e^+$ -the pair is arbitrarily polarized):

$$\begin{aligned} \frac{d^3\sigma_c}{dx_Z dx_1 d\Omega} = & \frac{\sqrt{2}}{128\pi^4} \cdot \frac{G_F^3 M_Z^6}{s(1-r_Z)^2} \cdot \frac{r_Z}{(y_1+r_H-r_Z)^2} \times \\ & \times \{ [(g_L^2(1-\lambda_1)(1+\lambda_2) + g_R^2(1+\lambda_1)(1-\lambda_2)) \cdot f_1 + 2g_L g_R \eta_1 \eta_2 f_2] \}, \end{aligned} \quad (9)$$

where

$$\begin{aligned} f_1 = & x_Z^2(1-v^2 \cos^2 \theta) + 4r_Z v^2(1+\cos^2 \theta) + \left(2 - \frac{y_1 + r_H}{r_Z} + \frac{(y_1 + r_Z)^2}{4r_Z^2} \right) [x_1^2(1-v^2 \cos^2 \theta_1) - \\ & - 4r_H v^2 \sin^2 \theta_1] + \frac{y_1 + r_Z}{r_Z} [x_Z x_1 - v^2 \sqrt{(x_Z^2 - 4r_Z)(x_1^2 - 4r_H)} \cos \theta \cos \theta_1 - (1-v^2)(y_2 - z_Z)], \end{aligned} \quad (10)$$

$$\begin{aligned} f_2 = & -v^2(x_Z^2 - 4r_Z) \sin^2 \theta \cos(2\varphi - \Phi) - \left(2 - \frac{y_1 + r_H}{r_Z} + \frac{(y_1 + r_Z)^2}{4r_Z^2} \right) [v^2(x_1^2 - 4r_H) \sin^2 \theta_1 \cos(2\varphi - \Phi) + \\ & + \frac{y_1 + r_Z}{r_Z} \left[\cos \Phi (x_Z x_1 - v^2 \sqrt{(x_Z^2 - 4r_Z)(x_1^2 - 4r_H)}) \cos \theta \cos \theta_1 - \frac{1+v^2}{2} \sqrt{(x_Z^2 - 4r_Z)(x_1^2 - 4r_H)} \times \right. \\ & \left. \times \sin \theta \sin \theta_1 (\cos \Phi + \cos(2\varphi - \Phi)) - (1+v^2)(y_2 - r_Z) \cos \Phi \right], \end{aligned} \quad (11)$$

λ_1 and λ_2 (η_1 and η_2) – the helicity (transverse components of spin vectors) of the electron and positron, $d\Omega = \sin \theta d\theta d\varphi$ – the solid angle of departure of the Z -boson, $\theta(\theta_1)$ – the angle between the directions of the momentums of the electron \vec{p}_1 and the Z -boson \vec{k} (Higgs boson \vec{k}_1), $v = \sqrt{1-4m^2/s}$ – the velocity of the electron in the center of mass system, $\vec{p}_1 + \vec{p}_2 = \vec{k} + \vec{k}_1 + \vec{k}_2 = 0$ because of which the final particles lie in the same plane with the azimuthal angle φ .

PRODUCTION OF A HIGGS-BOSONPAIR IN e^-e^+ -COLLISIONS (II)

It should be noted that the electron momentum \vec{p}_1 is directed along the axis Z , and its spin vector $\vec{\eta}_1$ is along the axis X , then the spin vector $\vec{\eta}_2$ will lie in the plane XOY , the angle between the transverse components of the spin vectors $\vec{\eta}_1$ and $\vec{\eta}_2$ is denoted by Φ .

We now proceed to the calculation of the diagram d), the amplitude of which can be written as follows :

$$M_d = g_{Zee} g_{ZZH}^2 \frac{1}{s(1-r_Z)} \frac{1}{s(y_2+r_H-r_Z)} \ell_\nu \left(g_{\nu\rho} - \frac{q'_\nu q'_\rho}{M_Z^2} \right) U_\rho^*(k), \quad (12)$$

where $q'_\nu = (p-k_2)_\nu = (k+k_1)_\nu$ is the total 4-momentum Z - and Higgs bosons. Based on this amplitude, the following expression is obtained for the differential effective cross section of the reaction $e^-e^+ \rightarrow ZHH$:

$$\frac{d^3\sigma_d}{dx_Z dx_1 d\Omega} = \frac{\sqrt{2}}{128\pi^4} \cdot \frac{G_F^3 M_Z^6}{s(1-r_Z)^2} \cdot \frac{r_Z}{(y_2+r_H-r_Z)^2} \times \\ \times \{ [(g_L^2(1-\lambda_1)(1+\lambda_2) + g_R^2(1+\lambda_1)(1-\lambda_2))] \cdot F_1 + 2g_L g_R \eta_1 \eta_2 F_2 \}, \quad (13)$$

where the functions F_1 and F_2 are obtained from the functions f_1 and f_2 (expressions (10) and (11)) using substitutions

$$\theta_1 \rightarrow \theta_2, x_1 \rightarrow x_2, y_1 \rightarrow y_2.$$

The square of the amplitude corresponding to the interference of diagrams c) and d)

$$M_c^+ M_d + M_d^+ M_c = 2 \frac{g_{Zee}^2}{s^2(1-r_Z)^2} \frac{g_{ZZH}^4}{s^2(y_1+r_H-r_Z)(y_2+r_H-r_Z)} \times \\ \times L_{\mu\nu} \left[-g_{\mu\nu} + \frac{k_\mu k_\nu}{M_Z^2} + \frac{k_{1\mu} k_{1\nu}}{M_Z^2} + \frac{k_{2\mu} k_{2\nu}}{M_Z^2} - \frac{k_\mu k_{1\nu} + k_{1\mu} k_\nu}{2M_Z^2} \frac{y_2-r_Z}{2r_Z} - \frac{k_\mu k_{2\nu} + k_{2\mu} k_\nu}{2M_Z^2} \frac{y_1-r_Z}{2r_Z} \right. \\ \left. - \frac{k_{1\mu} k_{2\nu} + k_{2\mu} k_{1\nu}}{2M_Z^2} \frac{1}{2r_Z} \left(y_Z + r_Z - 2r_H - \frac{y_1-r_Z}{2r_Z} (y_2-r_Z) \right) \right] \quad (14)$$

it has a bulky appearance, so it is not given here.

Based on the matrix element (14) for the contribution to the cross-section of the interference process $e^-e^+ \rightarrow ZHH$ of diagrams c) and d), we obtain the expression (angle Φ accepted π):

$$\frac{d^3\sigma_{c,d}^{(inter.)}}{dx_Z dx_1 d\Omega} = \frac{\sqrt{2}}{64\pi^4} \cdot \frac{G_F^3 M_Z^6}{s(1-r_Z)^2} \cdot \frac{r_Z}{(y_1+r_H-r_Z)(y_2+r_H-r_Z)} \left\{ g_L^2(1-\lambda_1)(1+\lambda_2) + g_R^2(1+\lambda_1)(1-\lambda_2) \right\} \times \\ \times \left[x_Z^2 \sin^2 \theta + 4r_Z(1+\cos^2 \theta) + (x_1^2 - 4r_H) \sin^2 \theta_1 + (x_2^2 - 4r_H) \sin^2 \theta_2 - \right. \\ \left. - \frac{y_2-r_Z}{2r_Z} (x_Z x_1 - \sqrt{(x_Z^2 - 4r_Z)(x_1^2 - 4r_H)}) \cdot \cos \theta \cos \theta_1 - 2(y_2 - r_Z) - \right. \\ \left. - \frac{y_1-r_Z}{2r_Z} (x_Z x_2 - \sqrt{(x_Z^2 - 4r_Z)(x_2^2 - 4r_H)}) \cdot \cos \theta \cos \theta_2 - 2(y_1 - r_Z) - \right. \\ \left. - \frac{1}{2r_Z} (x_1 x_2 - \sqrt{(x_1^2 - 4r_H)(x_2^2 - 4r_H)}) \cdot \cos \theta_1 \cos \theta_2 - 2(y_Z + r_Z - 2r_H) \right] \times \\ \times \left(y_Z + r_Z - 2r_H - \frac{1}{2r_Z} (y_1 - r_Z)(y_2 - r_Z) \right) + 2g_L g_R \eta_1 \eta_2 \left[((x_Z^2 - 4r_Z) \sin^2 \theta + \right. \\ \left. + (x_1^2 - 4r_H) \sin^2 \theta_1 - (x_2^2 - 4r_H) \sin^2 \theta_2) \cos 2\varphi + \frac{y_2-r_Z}{2r_Z} (x_Z x_1 - \sqrt{(x_Z^2 - 4r_Z)(x_1^2 - 4r_H)}) \times \right. \\ \left. \times \cos(\theta - \theta_1) - 2(y_2 - r_Z) - \sqrt{(x_Z^2 - 4r_Z)(x_1^2 - 4r_H)} \cdot \sin \theta \sin \theta_1 \cos(2\varphi) + \right. \\ \left. + \frac{y_1-r_Z}{2r_Z} (x_Z x_2 - \sqrt{(x_Z^2 - 4r_Z)(x_2^2 - 4r_H)}) \cdot \cos(\theta - \theta_2) - 2(y_1 - r_Z) - \sqrt{(x_Z^2 - 4r_Z)(x_2^2 - 4r_H)} \times \right. \\ \left. \times \cos(\theta_1 - \theta_2) - 2(y_Z + r_Z - 2r_H) - \sqrt{(x_1^2 - 4r_H)(x_2^2 - 4r_H)} \cdot \sin \theta_1 \sin \theta_2 \cos(2\varphi) \right] \}. \quad (15)$$

3. CALCULATION OF INTERFERENCE DIAGRAMS a), b) AND c), d)

During annihilation of an arbitrarily polarized electron-positron pair for interference diagram a), b) and c),

d), the following expressions are obtained:

$$\begin{aligned} \frac{d^3 \sigma_{a,c}^{(inter.)}}{dx_Z dx_1 d\Omega} &= \frac{3\sqrt{2}}{128\pi^4} \cdot \frac{G_F^3 M_Z^6}{s(1-r_Z)^2} \cdot \frac{r_H}{y_Z + r_Z - r_H} \cdot \frac{1}{y_1 + r_H - r_Z} \times \\ &\times \{-[g_L^2(1-\lambda_1)(1+\lambda_2) + g_R^2(1+\lambda_1)(1-\lambda_2)][x_Z^2 \sin^2 \theta + 4r_Z(1+\cos^2 \theta) + (x_1^2 - 4r_H) \sin^2 \theta_1 + \\ &+ \frac{y_1 + r_Z}{2r_Z} \cdot (x_Z x_1 - \sqrt{(x_Z^2 - 4r_Z)(x_1^2 - 4r_H)}) \cos \theta \cos \theta_1 - 2(y_2 - r_Z)] + \\ &+ 2g_L g_R \eta_1 \eta_2 [-(x_Z^2 - 4r_Z) \sin^2 \theta \cos(2\varphi) - (x_1^2 - 4r_H) \sin^2 \theta_1 \cos(2\varphi) + \\ &+ \frac{y_1 + r_Z}{2r_Z} (x_Z x_1 - \sqrt{(x_Z^2 - 4r_Z)(x_1^2 - 4r_H)}) \cos(\theta - \theta_1) - 2(y_2 - r_Z) - \\ &- \sqrt{(x_Z^2 - 4r_Z)(x_1^2 - 4r_H)} \sin \theta \sin \theta_1 \cos(2\varphi)]\}; \end{aligned} \quad (16)$$

$$\begin{aligned} \frac{d^3 \sigma_{a,d}^{(inter)}}{dx_Z dx_1 d\Omega} &= \frac{3\sqrt{2}}{128\pi^4} \cdot \frac{G_F^3 M_Z^6}{s(1-r_Z)^2} \cdot \frac{r_H}{y_Z + r_Z - r_H} \cdot \frac{1}{y_2 + r_H - r_Z} \times \\ &\times \{-[g_L^2(1-\lambda_1)(1+\lambda_2) + g_R^2(1+\lambda_1)(1-\lambda_2)][x_Z^2 \sin^2 \theta + 4r_Z(1+\cos^2 \theta) + \\ &+ (x_2^2 - 4r_H) \sin^2 \theta_2 + \frac{y_2 + r_Z}{2r_Z} \cdot (x_Z x_2 - \sqrt{(x_Z^2 - 4r_Z)(x_2^2 - 4r_H)}) \cos \theta \cos \theta_2 - 2(y_1 - r_Z)] + \\ &+ 2g_L g_R \eta_1 \eta_2 [-(x_Z^2 - 4r_Z) \sin^2 \theta \cos(2\varphi) - (x_2^2 - 4r_H) \sin^2 \theta_2 \cos(2\varphi) + \\ &+ \frac{y_2 + r_Z}{2r_Z} (x_Z x_2 - \sqrt{(x_Z^2 - 4r_Z)(x_2^2 - 4r_H)}) \cos(\theta - \theta_2) - 2(y_1 - r_Z) - \\ &- \sqrt{(x_Z^2 - 4r_Z)(x_2^2 - 4r_H)} \sin \theta \sin \theta_2 \cos(2\varphi)]\}; \end{aligned} \quad (17)$$

$$\begin{aligned} \frac{d^3 \sigma_{b,c}^{(inter)}}{dx_Z dx_1 d\Omega} &= \frac{\sqrt{2} G_F^3 M_Z^6}{256\pi^4} \cdot \frac{1}{s(1-r_Z)^2} \cdot \frac{1}{y_1 + r_H - r_Z} \cdot \frac{r_H}{r_Z} \times \\ &\times \{-[g_L^2(1-\lambda_1)(1+\lambda_2) + g_R^2(1+\lambda_1)(1-\lambda_2)][x_Z^2 \sin^2 \theta + 4r_Z(1+\cos^2 \theta) + \\ &+ (x_1^2 - 4r_H) \sin^2 \theta_1 + \frac{y_2 + r_Z}{2r_Z} (x_Z x_1 - \sqrt{(x_Z^2 - 4r_Z)(x_1^2 - 4r_H)}) \cos \theta \cos \theta_1 - 2(y_2 - r_Z)] + \\ &+ 2g_L g_R \eta_1 \eta_2 [-(x_Z^2 - 4r_Z) \sin^2 \theta \cos(2\varphi) - (x_1^2 - 4r_H) \sin^2 \theta_1 \cos(2\varphi) + \\ &+ \frac{y_1 + r_Z}{2r_Z} (x_Z x_1 - \sqrt{(x_Z^2 - 4r_Z)(x_1^2 - 4r_H)}) \cos(\theta - \theta_1) - 2(y_2 - r_Z) - \\ &- \sqrt{(x_Z^2 - 4r_Z)(x_1^2 - 4r_H)} \sin \theta \sin \theta_1 \cos(2\varphi)]\}; \end{aligned} \quad (18)$$

$$\begin{aligned} \frac{d^3 \sigma_{b,d}^{(inter)}}{dx_Z dx_1 d\Omega} &= \frac{\sqrt{2} G_F^3 M_Z^6}{256\pi^4} \cdot \frac{1}{s(1-r_Z)^2} \cdot \frac{1}{y_2 + r_H - r_Z} \cdot \frac{r_H}{r_Z} \times \\ &\times \{-[g_L^2(1-\lambda_1)(1+\lambda_2) + g_R^2(1+\lambda_2)(1-\lambda_1)][x_Z^2 \sin^2 \theta + 4r_Z(1+\cos^2 \theta) + \\ &+ (x_2^2 - 4r_H) \sin^2 \theta_2 + \frac{y_2 + r_Z}{2r_Z} \cdot (x_Z x_2 - \sqrt{(x_Z^2 - 4r_Z)(x_2^2 - 4r_H)}) \cos \theta \cos \theta_2 - \\ &- 2(y_1 - r_Z)] + 2g_L g_R \eta_1 \eta_2 [-(x_Z^2 - 4r_Z) \sin^2 \theta - (x_2^2 - 4r_H) \sin^2 \theta_2 \cos(2\varphi) + \\ &+ \frac{y_2 + r_Z}{2r_Z} (x_Z x_2 - \sqrt{(x_Z^2 - 4r_Z)(x_2^2 - 4r_H)}) \cos(\theta - \theta_2) - 2(y_1 - r_H) - \\ &- \sqrt{(x_Z^2 - 4r_Z)(x_2^2 - 4r_H)} \sin \theta \sin \theta_2 \cos(2\varphi)]\}; \end{aligned} \quad (19)$$

PRODUCTION OF A HIGGS-BOSONPAIR IN e^-e^+ -COLLISIONS (II)

Thus, we calculated the differential effective cross section of the reaction $e^-e^+ \rightarrow ZHH$ taking into account all Feynman diagrams (Fig. 1, a, b, c, d). This section contains the contributions of diagrams a), b) and their interferences (they are given in (I) work), the contributions of diagrams c), d) and their interferences (formulas (9), (13) and (15)), as well as the interferences of diagrams a) and c), a) and d), b) and c), b) and d) (formulas (16)-(19)).

4. LEFT-RIGHT AND TRANSVERSE SPIN ASYMMETRIES

Consider left-right A_{LR} and transverse $A_\varphi(x_Z, \theta)$ spin asymmetries taking into account all Feynman diagrams. In all expressions of the differential effective cross sections given above, the helicity of the electron and positron are in the form

$$[g_L^2(1-\lambda_1)(1+\lambda_2) + g_R^2(1+\lambda_1)(1-\lambda_2)],$$

consequently, the left-right spin asymmetry due to the longitudinal polarization of the electron is expressed by the formula

$$A_{LR} = \frac{g_L^2 - g_R^2}{g_L^2 + g_R^2}. \quad (20)$$

As can be seen, the left-right spin asymmetry A_{LR} depends only on the Weinberg parameter x_W and with the value of this parameter $x_W = 0.2315$ is $A_{LR} = 14\%$.

As for the transverse spin asymmetry $A_\varphi(x_Z, \theta)$, we estimate it at the value of the Higgs boson energy $x_1 = 0.5$ according to the formula

$$A_\varphi(x_Z, \theta) = \frac{2g_L g_R}{g_L^2 + g_R^2} \cdot \frac{\psi_2}{\psi_1}, \quad (21)$$

where the functions ψ_1 and ψ_2 are equal:

$$\begin{aligned} \psi_1 = & \frac{1}{4r_Z} \left(1 - \frac{3r_H}{y_Z + r_Z - r_H} \right)^2 [x_Z^2 \sin^2 \theta + 4r_Z(1 + \cos^2 \theta)] + \\ & + \frac{r_Z}{(y_1 + r_H - r_Z)^2} \cdot [x_Z^2 \sin^2 \theta + 4r_Z(1 + \cos^2 \theta) + \frac{y_1 + r_Z}{r_Z}(x_Z x_1 - 2(y_2 - r_Z))] + \\ & + \frac{r_Z}{(y_2 + r_H - r_Z)^2} \cdot \left[x_Z^2 \sin^2 \theta + 4r_Z(1 + \cos^2 \theta) + \left(2 - \frac{y_1 + r_H}{r_Z} + \frac{(y_1 + r_Z)^2}{4r_Z^2} \right) \times \right. \\ & \times (x_2^2 - 4r_H) \sin^2 \theta_2 + \frac{y_2 + r_Z}{r_Z} \cdot (x_Z x_2 - \sqrt{(x_Z^2 - 4r_Z)(x_2^2 - 4r_H)}) \cos \theta \cos \theta_2 - \\ & \left. - 2(y_1 - r_Z) \right] + \frac{2}{y_1 + r_H - r_Z} \cdot \frac{r_Z}{(y_2 + r_H - r_Z)} \cdot \left[x_Z^2 \sin^2 \theta + 4r_Z(1 + \cos^2 \theta) + \right. \\ & \left. + (x_2^2 - 4r_H) \sin^2 \theta_2 - \frac{y_2 - r_Z}{2r_Z}(x_Z x_1 - 2(y_2 - r_Z)) - \frac{y_1 - r_Z}{2r_Z} \cdot (x_Z x_2 - \right. \\ & \left. - \sqrt{(x_Z^2 - 4r_Z)(x_2^2 - 4r_H)}) \cos \theta \cos \theta_2 - 2(y_1 - r_Z) \right] - \frac{1}{2r_Z} (x_1 x_2 - 2(y_Z + r_Z - 2r_H)) \times \\ & \times \left(y_Z + r_Z - 2r_H - \frac{1}{2r_Z} (y_1 - r_Z)(y_2 - r_Z) \right) \left] - \frac{3}{y_Z + r_Z - r_H} \cdot \frac{r_H}{y_1 + r_H - r_Z} \times \right. \\ & \left. \times \left[x_Z^2 \sin^2 \theta + 4r_Z(1 + \cos^2 \theta) + \frac{y_1 + r_Z}{2r_Z}(x_Z x_1 - 2(y_2 - r_Z)) \right] - \right. \\ & - \frac{3}{y_Z + r_Z - r_H} \cdot \frac{r_H}{y_2 + r_H - r_Z} \left[x_Z^2 \sin^2 \theta + 4r_Z(1 + \cos^2 \theta) + (x_2^2 - 4r_H) \sin^2 \theta_2 + \right. \\ & \left. + \frac{y_2 + r_Z}{2r_Z}(x_Z x_2 - \sqrt{(x_Z^2 - 4r_Z)(x_2^2 - 4r_H)}) \cos \theta \cos \theta_2 - 2(y_1 - r_Z) \right] - \\ & \left. - \frac{r_H}{2r_Z} \cdot \frac{1}{y_1 + r_H - r_Z} \left[x_Z^2 \sin^2 \theta + 4r_Z(1 + \cos^2 \theta) + \frac{y_1 + r_Z}{2r_Z}(x_Z x_1 - 2(y_2 - r_H)) \right] - \right. \end{aligned}$$

$$\begin{aligned}
& -\frac{r_H}{2r_Z} \cdot \frac{1}{y_2 + r_H - r_Z} \left[x_Z^2 \sin^2 \theta + 4r_Z(1 + \cos^2 \theta) + (x_2^2 - 4r_H) \sin^2 \theta_2 + \right. \\
& \left. + \frac{y_2 + r_Z}{2r_Z} \cdot (x_Z x_2 - \sqrt{(x_Z^2 - 4r_Z)(x_2^2 - 4r_H)}) \cos \theta \cos \theta_2 - 2(y_1 - r_Z) \right]; \quad (22) \\
& \psi_2 = \frac{1}{4r_Z} \left(1 - \frac{3r_H}{y_Z + r_Z - r_H} \right)^2 [(x_Z^2 - 4r_Z) \sin^2 \theta \cos 2\varphi + \\
& + \frac{r_Z}{(y_1 + r_H - r_Z)^2} \cdot [(x_Z^2 - 4r_Z) \sin^2 \theta \cos 2\varphi + \frac{y_1 + r_Z}{r_Z} (-x_Z x_1 + 2(y_2 - r_Z))] + \\
& + \frac{r_Z}{(y_2 + r_H - r_Z)^2} \cdot \left[(x_Z^2 - 4r_Z) \sin^2 \theta \cos 2\varphi + \left(2 - \frac{y_1 + r_H}{r_Z} + \frac{(y_1 + r_Z)^2}{4r_Z^2} \right) \times \right. \\
& \times (x_2^2 - 4r_H) \sin^2 \theta_2 \cos 2\varphi + \frac{y_2 + r_Z}{r_Z} \cdot (-x_Z x_2 + \sqrt{(x_Z^2 - 4r_Z)(x_2^2 - 4r_H)}) \times \\
& \left. \times (\cos \theta \cos \theta_2 + \sin \theta \sin \theta_2 (1 + \cos 2\varphi) + 2(y_1 - r_Z)) \right] + \\
& + \frac{2}{y_1 + r_H - r_Z} \cdot \frac{r_Z}{y_2 + r_H - r_Z} \cdot \left[\cos 2\varphi ((x_Z^2 - 4r_Z) \sin^2 \theta - (x_2^2 - 4r_H) \sin^2 \theta_2) + \right. \\
& + \frac{y_2 - r_Z}{2r_Z} \cdot (x_Z x_1 - 2(y_2 - r_Z)) + \frac{y_1 - r_Z}{2r_Z} \cdot (x_Z x_2 - \sqrt{(x_Z^2 - 4r_Z)(x_2^2 - 4r_H)}) \cos(\theta - \theta_2) - \\
& \left. - 2(y_1 - r_Z) - \sqrt{(x_Z^2 - 4r_Z)(x_2^2 - 4r_H)} \cdot \sin \theta \sin \theta_2 \cos 2\varphi \right] + \\
& + \frac{1}{2r_Z} \left(y_Z + r_Z - 2r_H - \frac{(y_1 - r_Z)(y_2 - r_Z)}{2r_Z} \right) \cdot (x_1 x_2 - 2(y_Z + r_Z - 2r_H)) \left. + \frac{3}{y_Z + r_Z - r_H} \cdot \right. \\
& \times \frac{r_H}{y_1 + r_H - r_Z} \cdot \left[-(x_Z^2 - 4r_Z) \sin^2 \theta \cos 2\varphi + \frac{y_1 + r_Z}{2r_Z} (x_Z x_1 - 2(y_2 - r_Z)) \right] + \\
& + \frac{3}{y_Z + r_Z - r_H} \cdot \frac{r_H}{y_2 + r_Z - r_H} \cdot \left[\cos 2\varphi (-(x_Z^2 - 4r_Z) \sin^2 \theta - (x_2^2 - 4r_H) \sin^2 \theta_2) + \right. \\
& + \frac{y_2 + r_Z}{2r_Z} (x_Z x_2 - \sqrt{(x_Z^2 - 4r_Z)(x_2^2 - 4r_H)}) \cos(\theta - \theta_2) - 2(y_1 - r_Z) - \\
& \left. - \sqrt{(x_Z^2 - 4r_Z)(x_2^2 - 4r_H)} \cdot \sin \theta \sin \theta_2 \cos 2\varphi \right] + \\
& + \frac{r_H}{2r_Z} \cdot \frac{1}{y_1 + r_H - r_Z} \left[-(x_Z^2 - 4r_Z) \sin^2 \theta \cos 2\varphi + \frac{y_1 + r_Z}{2r_Z} (x_Z x_1 - 2(y_2 - r_Z)) \right] + \\
& + \frac{r_H}{2r_Z} \cdot \frac{1}{y_2 + r_H - r_Z} [\cos 2\varphi (-(x_Z^2 - 4r_Z) \sin^2 \theta - (x_2^2 - 4r_H) \sin^2 \theta_2) + \\
& + \frac{y_2 + r_Z}{2r_Z} (x_Z x_2 - \sqrt{(x_Z^2 - 4r_Z)(x_2^2 - 4r_H)}) \cos(\theta - \theta_2) - 2(y_1 - r_H) - \\
& \left. - \sqrt{(x_Z^2 - 4r_Z)(x_2^2 - 4r_H)} \cdot \sin \theta \sin \theta_2 \cos 2\varphi \right]. \quad (23)
\end{aligned}$$

When obtaining these formulas, we took into account that at $x_1 = 0.5$ $x_1^2 - 4r_H = 0$ and the angle θ_2 between the momentums of the electron and the second Higgs boson \vec{k}_2 is related to the angle θ by the ratio

$$\cos \theta_2 = -\sqrt{\frac{x_Z^2 - 4r_Z}{x_2^2 - 4r_H}} \cos \theta.$$

Figure 2 shows the dependence of the transverse spin asymmetry $A_\varphi(x_Z, \theta)$ on the angle θ at different energy values x_Z : 1) $x_Z = 0.55$; 2) $x_Z = 0.60$; 3) $x_Z = 0.65$. As can be seen from the figure, the transverse spin asymmetry is positive and at $x_Z = 0.55$ and $x_Z = 0.60$ with increasing angle θ , it decreases and reaches a minimum at an angle of $\theta = 90^\circ$, and with further increase in angle, the transverse spin asymmetry increases. At $x_Z = 0.65$, an increase in the angle θ leads to an increase in the transverse spin asymmetry, it reaches a maximum at $\theta = 90^\circ$, and then decreases.

PRODUCTION OF A HIGGS-BOSONPAIR IN e^-e^+ -COLLISIONS (II)

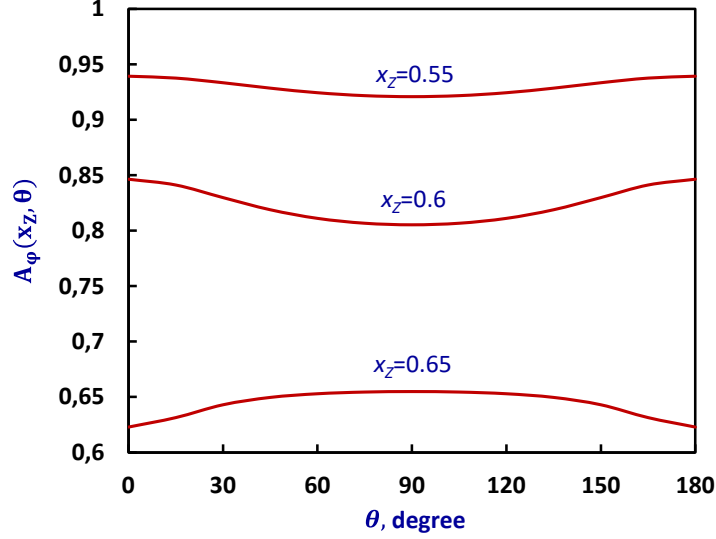


Fig. 2. Angular dependence of transverse spin asymmetry at different x_z

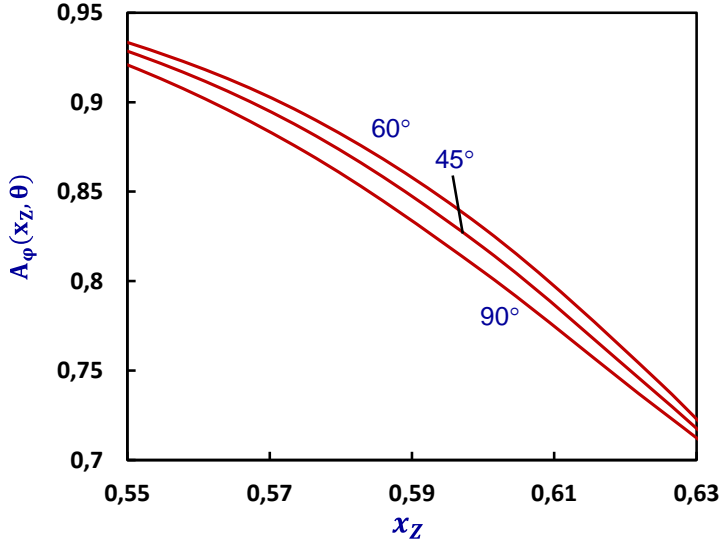


Fig. 3. Energy dependence of transverse spin asymmetry at different angles θ

Fig. 3 illustrates the dependence of the transverse spin asymmetry on the fraction of energy x_z carried away by the Z^0 -boson at different departure angles θ : 1) $\theta=45^\circ$; 2) $\theta=60^\circ$; 3) $\theta=90^\circ$. It follows from the figure that with increasing x_z the transverse spin asymmetry monotonically decreases.

Averaging over the polarization states e^-e^+ -pairs for the differential effective cross section of the reaction $e^-e^+ \rightarrow HHZ^0$ we have the formula (all Feynman diagrams are taken into account)

$$\frac{d^3\sigma}{dx_z dx_1 d\Omega} = \frac{\sqrt{2}}{128\pi^4} \frac{G_F^3 M_Z^6}{s} \cdot \frac{1}{(1-r_Z)^2} \cdot \psi_1, \quad (24)$$

where the function ψ_1 is given by formula (22).

Figure 4 shows the angular dependence of the differential effective cross section of the reaction $e^-e^+ \rightarrow HHZ^0$ at $\sqrt{s} = 500$ GeV, $x_1 = 0.5$, $x_W = 0.2315$ and various energy values x_z : 1)

$x_z = 0.65$; 2) $x_z = 0.70$; 3) $x_z = 0.75$. As can be seen from the figure, with an increase in the polar angle θ , the differential effective cross-section increases and reaches a maximum at an angle of $\theta=90^\circ$, and with a further increase in the same angle, the effective cross-section decreases. An increase in the energy x_z carried away by the Z^0 -boson leads to an increase in the effective cross-section of the process under study.

Fig. 5 illustrates the dependence of the cross section of the process $e^-e^+ \rightarrow HHZ^0$ on the variable x_z at $\sqrt{s} = 500$ GeV, $x_1 = 0.5$ and various values of the departure angle θ : 1) $\theta=30^\circ$; 2) $\theta=60^\circ$; 3) $\theta=90^\circ$. It can be seen from the figure that with an increase in the energy x_z carried away by the Z^0 -boson, the effective cross-section increases, the increase in the departure angle θ also leads to an increase in the effective cross-section of the process under consideration.

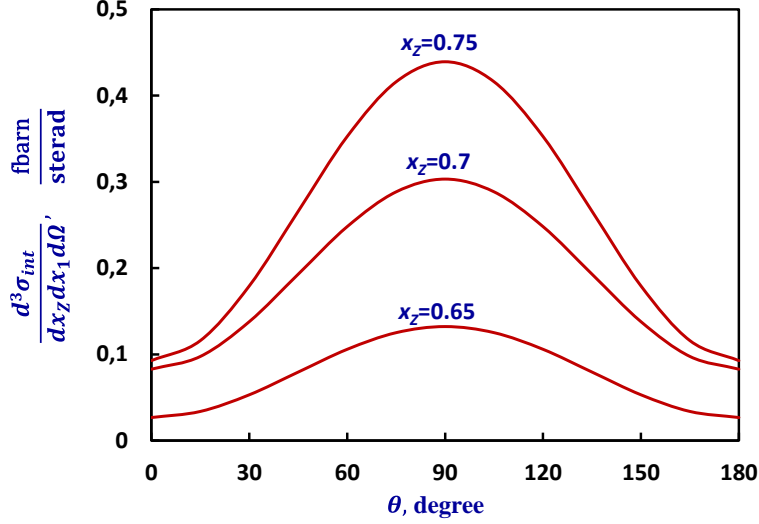


Fig. 4. Angular dependence of the cross section the process $e^-e^+ \rightarrow HHZ^0$ at different energy values x_z

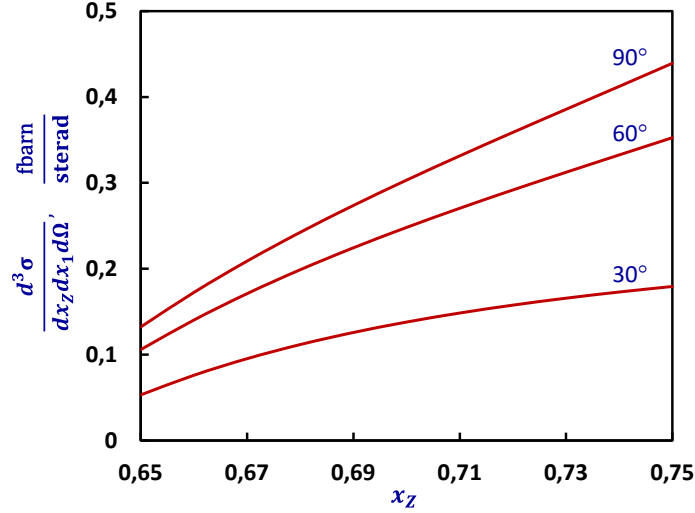


Fig. 5. Energy dependence of the cross section of process $e^-e^+ \rightarrow HHZ^0$ at different angles of θ

By averaging over the polarization states of the electron-positron pair and integrating over the departure angles of the particles, for the energy distribution of the Higgs bosons we obtain the formula

$$\frac{d^2\sigma}{dx_1 dx_2} = \frac{G_F^3 M_Z^6}{48\sqrt{2}\pi^3} \cdot \frac{g_L^2 + g_R^2}{s(1-r_Z)^2} \cdot \psi, \quad (25)$$

where

$$\psi = \frac{\varphi_0}{8} b^2 + \frac{1}{4r_Z(y_1 + r_H - r_Z)} \left[\frac{\varphi_1}{y_1 + r_H - r_Z} + \frac{\varphi_2}{y_2 + r_H - r_Z} + 2r_Z b \varphi_3 \right] + \{y_1 \leftrightarrow y_2\}, \quad (26)$$

$$b = \frac{\lambda_{HHH}}{y_3 - r_H + r_Z} + \frac{2}{y_1 + r_H - r_Z} + \frac{2}{y_2 + r_H - r_Z} + \frac{1}{r_Z}, \quad (27)$$

$$\varphi_0 = r_Z[(y_1 + y_2)^2 + 8r_Z],$$

$$\varphi_1 = (y_1 - 1)^2(r_Z - y_1)^2 - 4r_H y_1(y_1 + y_1 r_Z - 4r_Z) + r_Z(r_Z - 4r_H)(1 - 4r_H) - r_Z^2,$$

$$\varphi_2 = [r_Z(y_3 + r_Z - 8r_H) - (1 + r_Z)y_1 y_2](1 + y_3 + 2r_Z) + y_1 y_2[y_1 y_2 + 1 + r_Z^2 + 4r_H(1 + r_Z)] + 4r_H r_Z(1 + r_Z + 4r_H) + r_Z^2,$$

$$\varphi_3 = y_1(y_1 - 1)(r_Z - y_1) - y_2(y_1 + 1)(y_1 + r_Z) + 2r_Z(1 + r_Z - 4r_H).$$

Figure 6 shows the dependence of the differential effective cross section (25) on the scaling energy x_1 at $\sqrt{s} = 500$ GeV and various values of the variable x_2 : 1) $x_2=0.65$; 2) $x_2=0.75$; 3) $x_2=0.85$. As can be seen from the figure, at $x_2=0.85$, the differential effective cross-section increases with the growth of the variable x_1 , and at $x_2=0.75$ ($x_2=0.65$), the effective cross-section first decreases and reaches a minimum at $x_1=0.67$ ($x_1=0.73$), and then with an increase of x_1 it begins to grow. In the case of $x_2=0.85$ and $x_1=0.8$, the cross-section of the process is 2.23 fbarn.

5. CONCLUSION

In conclusion, we note that the experimental

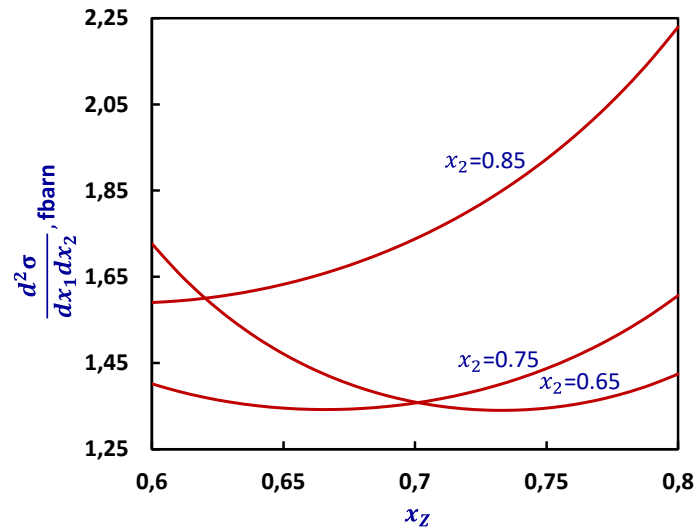


Fig. 6. Energy dependence of the reaction $e^-e^+ \rightarrow HHZ^0$ cross section at different values x_2 .

We discussed the process of the production of a vector Z^0 -boson and two Higgs boson pairs in polarized electron-positron collisions $e^-e^+ \rightarrow HHZ^0$. Taking into account all possible Feynman diagrams a), b), c) and d) Fig. 1, analytical expressions for the amplitudes and differential effective cross section of the process are obtained. Left-right A_{LR} and transverse

study of the reaction of the association production of a Higgs boson pair and a vector Z^0 -boson in electron-positron annihilation is of great interest, since it allows measuring the interaction constants of three Higgs bosons g_{HHH} and two Z^0 - and two Higgs bosons g_{ZZHH} .

Although the interaction constants of vector bosons with the Higgs boson g_{ZZH} and g_{WWH} are measured in the LHC in proton-proton collisions, however, direct measurement of the interaction constants g_{HHH} and g_{ZZHH} is associated with certain difficulties.

Therefore, the study of the process $e^-e^+ \rightarrow HHZ^0$ is of particular interest.

spin asymmetries A_φ due to longitudinal and transverse polarizations of the electron-positron pair are determined. The dependence of these characteristics and the differential effective cross-section on the departure angles and particle energies is studied in detail. The calculation results are illustrated with graphs.

- | | |
|---|--|
| <p>[1] A.A. Sokolov, I.M. Ternov, V.Ch. Zhukovsky, A.V. Borisov. Calibration fields. Moscow: Publishing House of MSU, 1986. 260 p. (in Russian).</p> <p>[2] A. Djouadi. The Anatomy of Electro-Weak Symmetry Breaking. Tome I: The Higgs boson in the Standard Model. arXiv: hep-ph/0503172v2, 2005.</p> <p>[3] S.K. Abdullayev. Standard Model, properties of leptons and quarks. Baku, 2017. 276 p. (in Azerb.)</p> <p>[4] ATLAS Collaboration. Observation of a new particle in the search for the Standard Model Higgs boson with the ATLAS detector of the LHC. Phys. Letters, 2012, B 716, p. 1-29.</p> | <p>[5] CMS Collaboration. Observation of a new boson at mass of 125 GeV with the CMS experiment at the LHC. Phys. Letters, 2012, B 716, p. 30-60.</p> <p>[6] V.A. Rubakov. On Large Hadron Colliders discovery of a new particle with Higgs Boson properties. UFN, 2012, V.182, No 10, p.1017-1025 (in Russian).</p> <p>[7] D.I. Kazakov. The Higgs boson is found: what is next? UFN, 2014, V. 184, No 9, p. 1004-1017 (In Russian).</p> <p>[8] A.V. Lanev. CMS Collaboration results: Higgs boson and search for new physics. UFN, 2014, V. 184, No 9, p. 996-1004 (In Russian).</p> <p>[9] V.D. Shiltsev. High energy particle colliders:</p> |
|---|--|

- past 20 years, next 20 years and beyond. UFN, 2012, V. 182, No 10, p. 1033-1046. (in Russian).
- [10] *K. Peters*. Prospects for beyond Standard Model Higgs boson searches at future LHC runs and other machines. arXiv: 1701.05124v2 [hep-ex], 2007, 8p.
- [11] *W. Kilian, M. Kramer, P. Zerwas*. Higgsstrahlung and WW fusion in e^+e^- -collisions. Phys. Lett. B373, 1996, p. 135-140.
- [12] *M. Greco, G. Montagna, O. Nicrosini, F. Piccinini, G. Volpi*. ISR corrections to associated HZ production at future Higgs factories. Phys. Lett. 2018. v. B777. P. 294-297.
- [13] *M. Greco, T. Han, Z. Lio*. ISR effects for resonant Higgs production at future lepton colliders. Phys. Lett. 2016, v. B763, p. 409-415.
- [14] *Y. Gong, Z. Li, X. Xu, L. Yang, X. Zhao*. Mixed QCD-electroweak corrections for Higgs boson production at e^+e^- -colliders. Phys. Rev., 2017, v. D 95 (9), p. 093003.
- [15] *A. Djouadi, W. Kilian, M. Mühlleitner, P.M. Zerwas*. Testing Higgs self-couplings at e^+e^- -linear colliders. Eur. Phys. J. C Particles and Fields, 1999, v. 10, p. 27-43.
- [16] *V. Barger, T. Han, P. Langacker, B. McElrath, P. Zerwas*. Effects of genuine dimension-six Higgs operators. Phys. Rev., 2003, v. D67, p. 115001.
- [17] *S.K. Abdullayev, M.Sh. Gojayev*. Production of a Higgs-boson pair in e^+e^- -collisions (I). Izv. VUZov. Fizika, 2022, т. 65, № 8, с. 28-36 (In Russian).

Received: 29.12.2022

CHANGE IN THE PROPERTIES OF POLYMER NANOCOMPOSITES (PP+ZrO₂) WITH METAL OXIDE NANOADDITIVES AFTER ELECTROTHERMOPOLARIZATION

H.S. IBRAHIMOVA

Institute of Physics, Ministry of Science and Education

hicran90@rambler.ru

The presented scientific article discusses the changes taking place in isotactic propylene and metal nanoadditive nanocomposite before and after exposure to ETP. Depending on the percentage of the metal nanoadditive in the PP+ZrO₂ nanocomposite, the permittivity (ϵ), dielectric loss angle ($\text{tg}\alpha$), and logarithm of resistivity ($\lg\rho$) are observed. The obtained dependence is explained by the high permittivity of the nanoadditive incorporated into the polymer matrix. Also, the incorporation of the nanoadditive leads to the formation of structural defects and, as a consequence, an increase in electrical conductivity and a decrease in strength. The change in the dielectric properties of the PP+3% ZrO₂ nanocomposite before and after electrothermopolarization was determined at a constant electric field strength. TSD curves have been plotted that characterize the electret state at various values of the electric field, and the parameters of the electret state have been calculated from these curves.

Keywords: nanocomposites, polypropylene, electrothermal polarization, mechanical and electrical strength, thermally stimulated depolarization current.

PACS:61.46.w,82.35.Np,71.38.k

INTRODUCTION

In recent years, in connection with the development of information technologies, biotechnology, medicine, etc. interest in nanoscale systems and, accordingly, in nanocomposites has sharply increased, since these objects have a number of specific features compared to ordinary bulk materials.

Nanostructured metal-polymer materials are an interesting area of modern science and nanotechnology, since the use of metals, their oxides, or complexes leads to a change in the catalytic, optical, magnetic, and other properties of polymer materials. The study of nano- and microworld objects is a priority direction in the development of modern science and technology. In recent years, there has been increasing interest in research related to the production of metallic nanomaterials and the study of their structure and properties, which is currently one of the most urgent problems of metallurgy. However, the resulting nanocomposites are often under the influence of external factors, especially the electric field. Of particular interest are the changes that occur in these nanocomposites under the influence of the electric field. By adding additives of various nature to polyolefins, it is possible to increase or decrease the stability of their electret states. Based on a large number of experiments, it can be judged that the stability of the electret states of these substances can be controlled by introducing nanometal oxides into polymers [1-4]. One of the most important effects of the electric field is the change in charge state in these nanocomposites. And, of course, this change, like all other properties, also affects the dielectric properties. In nanocomposites under the influence of the electric field migratory polarization, a change in dielectric losses, and injection phenomena at the boundaries with electrodes can be observed.

EXPERIMENTAL PART

To obtain nanocomposites, the polymer is first dissolved in toluene at the melting point, and then ZrO₂ nanoadditive stabilized with Y₂O₃ is poured into the mixture. Nanocomposite samples with a thickness of 50-100 μm are obtained after storing the resulting nanomaterial under the suction cabinet and holding it for 3 minutes at a pressure of 15 MPa by hot pressing. Thus, in the mode of fast cooling at a rate of 20-35 $^{\circ}\text{C}/\text{sec}$, the composites were immersed in the water-ice mixture together with the foil. Polymer nanocomposites were exposed to various electric field strengths for 1 hour at a temperature $T=373\text{K}$ below the breakdown voltage of the electric field. The strength properties of the studied nanocomposites were determined at room temperature [5]. The permittivity (ϵ) and dielectric loss tangent ($\text{tg}\alpha$) were measured with an E8-4 automatic device at a frequency of $100\text{-}10^6$ Hz, and the resistivity with an E6-13A teraohmmeter. The electret state was studied starting from room temperature in the range of 20 $^{\circ}\text{C}$ -200 $^{\circ}\text{C}$ for 4 min/cm. To obtain the electret state in the polyolefins under study, the samples are placed between two electrodes in the device used. It should be noted that the surface charge density, activation energy, and thickness of the polymer matrix inside the composite, which are the main characteristics of the electret state, are studied by the method of thermally stimulated depolarization, which is one of the most effective and widely used methods. The activation energy of the nanocomposites was calculated by the Garlick-Gibson method. This activation energy value indicates that the traps formed as a result of polarization are high-energy. The thickness of the interfacial layer is calculated by the formula

$$\delta = \frac{2ne^2}{\epsilon_1\epsilon_2\kappa T}$$

Here ε_1 and ε_2 – is the permittivity of the polymer and nanoadditive, k – is the Boltzmann constant and T – is the absolute temperature.

nanocomposite samples on the percentage of nanoadditive. As is seen from the figure, with an increase in the percentage of nanoadditive, i.e. ZrO_2 nanometal oxide, the permittivity (ε) and dielectric loss angle ($tg\alpha$) values in these samples increase, however, despite this, we observe a decrease in the resistivity $lg\rho$.

RESULTS AND THEIR DISCUSSION

Figure 1 shows the dependence of the electrophysical parameters of PP+ ZrO_2

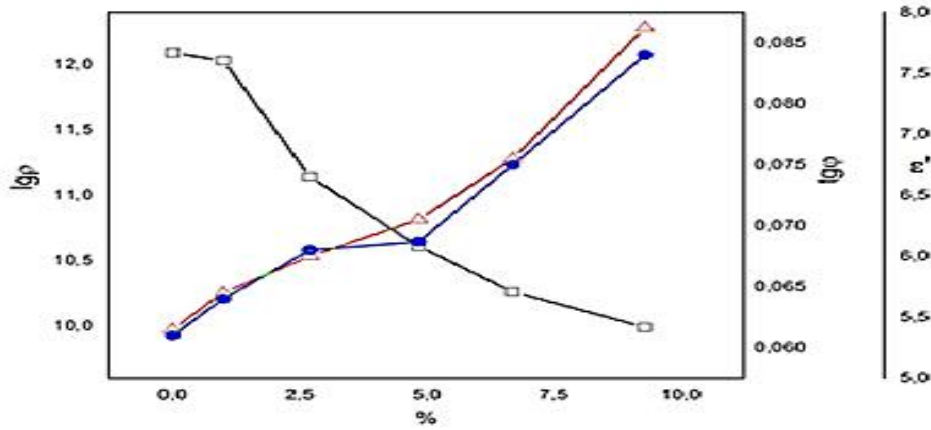


Fig. 1. Dependence of the permittivity (ε), dielectric loss angle ($tg\alpha$) and logarithm of resistivity $lg\rho$ in PP+ ZrO_2 nanocomposite on the percentage of nanoadditive

The dependence obtained can be explained by the high permittivity of the nanoadditive incorporated into the polymer matrix. Thus, if the permittivity of isotactic polypropylene, which we take as a matrix, is 2.2, the permittivity of ZrO_2 that we take as a nanoadditive is 25. In our opinion, the incorporation of metal oxide nanoadditives into the matrix leads to the formation of cracks, which reduces the resistivity of the nanocomposite. Naturally, a decrease in resistivity leads to an increase in the conductivity of the nanocomposite [6].

is a correlation between ε , $tg\alpha$ and electrical strength. For non-polar polymers, the permittivity ε is due to electron polarization, while dielectric loss is due to two reasons - dipole polarization and electrical conductivity. Changes in the molecular structure also affect these parameters [7,8]. It is noteworthy that, in our opinion, the main reason for the strength loss of the nanocomposite is an increase in conductivity. The observed decrease in strength is due to the formation of numerous structural defects, which is confirmed by the results of TSD. To study the stabilization properties of electric charges the process of depolarization of nanocomposite samples is considered [9].

Figure 2 shows the dependence of the electric strength, permittivity (ε) and loss angle tangent ($tg\alpha$) of PP+3% ZrO_2 nanocomposites on various electric field strengths. It can be seen from the figure that there

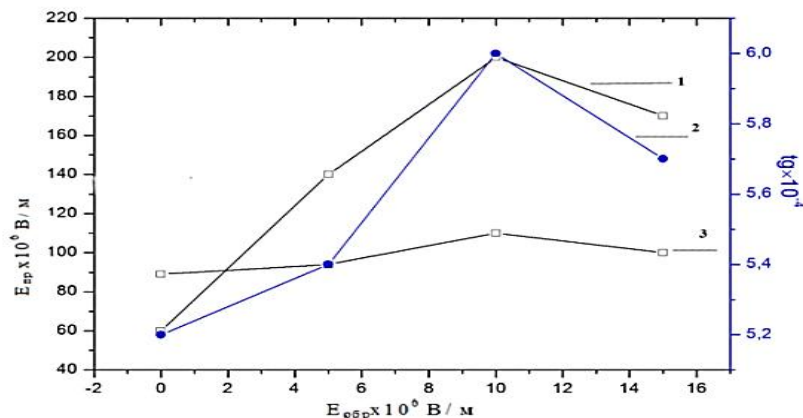


Fig. 2. Dependence of the electric strength, permittivity, and dielectric loss angle of the PP+3% ZrO_2 nanocomposite on the treatment intensity of electric field.

Figure 3 shows the TSD curves obtained after exposure to nanocomposites of various values of electric field strength. By calculating the area under the curves, the activation energy of the charges released from the traps, the thickness of the interfacial layer between the matrix and the nanoadditive, and the amount of charge per unit area can be calculated. These parameters calculated by us are given in Table

1. The maxima formed by the curves are determined by the amount of charge released from the traps. The activation energy of nanocomposites has a value of 0,72 eV at the field value $E=10 \cdot 10^6$ V/m, keeping the temperature constant. This activation energy value indicates that the traps created by polarization have high energy [10, 11].

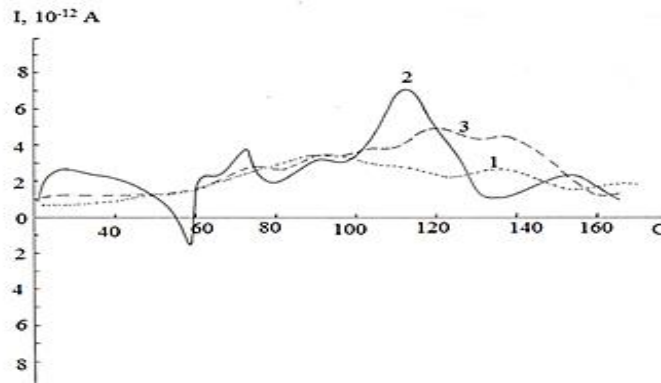


Fig. 3. TSD curves plotted after exposure of PP+3% ZrO₂ nanocomposites to ETP at various electric field strengths 1- $E=5 \cdot 10^6$ V/m, 2 $E=10 \cdot 10^6$ V/m, 3 - $E=15 \cdot 10^6$ V/m.

If we compare the calculations obtained from the TSD curves, then it can be seen that at a field value of $E=10 \cdot 10^6$ V/m, these parameters get the maximum value.

Table 1.

Surface charge density, activation energy, thickness of the interfacial layer inside the polymer matrix composite, calculated from TSD curves at different electric field strengths at a temperature of $T=373$ K.

	$E=5 \cdot 10^6$ V/m	$E=10 \cdot 10^6$ V/m	$E=15 \cdot 10^6$ V/m
$\delta(\mu\text{m})$	$7,211 \cdot 10^{-12}$	$11,4 \cdot 10^{-12}$	$11,1 \cdot 10^{-12}$
$q(\text{C/m}^2)$	$95,3 \cdot 10^{-7}$	$150,53 \cdot 10^{-7}$	$148 \cdot 10^{-7}$
$Q(\text{C})$	$4,672 \cdot 10^{-9}$	$7,37 \cdot 10^{-9}$	$7,24 \cdot 10^{-9}$
$E(\text{eV})$	0,44	0,72	0,38

CONCLUSION

Thus, after exposure of nanocomposites consisting of PP+ZrO₂ to ETP, a significant change in charge state occurs, which affects their strength and dielectric properties. The regions between the amorphous and crystalline phases play the role of

traps. In heterogeneous polymer compounds, there are boundaries that separate two phases, which in most cases act as energy traps. By varying the percentage of polymer and nanoadditive, it is possible to increase or decrease the thickness of the boundary layer, thereby controlling the electret states and dielectric properties.

- [1] N.C. Angastiniotis, S. Christopoulos, K.C. Petalidou et al. Controlling the optical properties of nanostructured oxide-based polymer films [Scientific Reports](#) Vol 11, Article number: 16009 (2021).
- [2] A.E. Hend, A.H. Maroof, A.N. Nadra et al. Development of natural polymer/metal oxide nanocomposite reinforced with graphene oxide for optoelectronic applications. *NRIAG Astronomy and Geophysics J* 2020, Vol. 10, No. 1, 10–22.
- [3] N.T. Kahramanov et al. Nanostructuralized composites and polymer material science, *Plastic Masses* 1–2, 49 (2016).
- [4] R.N. Yastrebinski, P.V. Matyuxin, Y. Samoiloa. Use of heavy metal oxides for synthesis of radiation protective materials *International journal of applied and fundamental research*–2015. – № 12(2), p 1199-1202.
- [5] M.A. Ramazanov, F.V. Hajiyeva, A.M. Maharramov and U.A. Hasanova. Effect of corona discharge on the structure and photoluminescence properties of nanocomposites based on polypropylene (PP) and zirconium dioxide (ZrO₂) nanoparticles *J. Ferroelectrics* 2017, Vol. 507, 1–6.
- [6] T.S. Sazanova, M.Vorotyntsev, V.B. Kulikov,

- IM. Davletbaeva, I.I. Zaripo.* AFM Study of Hybrid Polymeric Membranes: Surface Topographical Analysis and Estimation of Pore Size Distribution Membranes and Membrane Technologies 2016, V 6, № 2, p. 166–175.
- [7] *M.A. Ramazanov, H.S. Ibrahimova, H.A. Shirinova.* Influence of temperature-time crystallization conditions on PP+ZrO₂ charge state and electret properties. J ferroelectrics 577,1 pp 153-160.
- [8] *A. Rychkov D. Rychkov.* Electret properties of polyethylene and polytetrafluoroethylene films with chemically modified surface IEEE Transactions on Dielectrics and Electrical Insulation Vol. 18, №1, 2011p 8-14.
- [9] *M.A. Umarov, I.N. Ganiev.* Temperature dependence of heat capacity and change in thermodynamic functions of lead grade c2. Journal of Mechanical Engineering and Mechanical Engineering 2018, 23-28.
- [10] *A.M. Magerramov, M.A. Nuriyev and F.A. Akhmed.* Peculiarities of composite charge states of metal polypropylene-oxides. Physics and chemistry of material treatment, №1, pp. 57–60, 2013.
- [11] *H.S. Aliyev.* Features of forming volume discharges in polymer dielectrics under the influence of electric discharges Azerbaijan journal of physics 2019, v.25 №4 p.15-19.

Received: 09.01.2023

THERMAL PHOTONS PRODUCTION IN PROTON-PROTON COLLISIONS AT HIGH ENERGIES

PART II. DETERMINATION OF DOMINANT PROCESS OF PRODUCTION OF THERMAL PHOTONS

M.R. ALIZADA, A.I. AHMADOV

Department of Theoretical Physics, Baku State University

str. Z. Khalilov, 23, Az-1148 Baku, Azerbaijan

E-mail: mohsunalizade@gmail.com

Thermal photons produced in following processes: $\pi^+ \pi^- \rightarrow \gamma \rho^0$, $\pi^\pm \rho^0 \rightarrow \gamma \pi^\pm$, $\rho^0 \rightarrow \gamma \pi^+ \pi^-$, $\pi^+ \pi^- \rightarrow \gamma \eta$, $\pi^\pm \eta \rightarrow \gamma \pi^\pm$, $\pi^+ \pi^- \rightarrow \gamma \gamma$ has been investigated. The dependencies of differential cross-sections of processes of production thermal photons on energy of colliding mesons (\sqrt{s}), transverse momentum (p_T) and on cosine of scattering angle of photons has been determined without and taking into account formfactor of meson and has been compared. Dominant process has been determined. Energetic spectrums of thermal photons produced in these processes has been determined. A comparison of differential cross sections of thermal photon production processes and prompt photon production of processes of Compton scattering of quark-gluon and annihilation of a quark-antiquark pair has been carried out.

Keywords: proton-proton collision, mesons, thermal photons, Feynman diagram, differential cross-section.

PACS: 13.75.Lb; 13.30.Eg; 13.20.Cz; 13.25.Cq

I. INTRODUCTION

At present meson photoproduction has become a major tool for studying the properties of strong interaction in a mode where this fundamental force cannot be considered through perturbation theory methods. This almost completely replaced meson-induced reactions, such as the elastic scattering of the pion that previously dominated the area.

The number of photons introduced by the decay scale of the meson with the total number of charged particles formed in the collision, while the number of photons produced by the quark and gluon reactions could be expected to scale with the square of the number of charged particles [1,2]. Another method is that the number of photons introduced by the quark-gluon plasma is obtained by integrating the rate R (the number of reactions per unit time per unit volume that the photon produces) in the space-time history of the collision. Roughly speaking, the output is the speed x volume x time. More photons come out of the final state of the meson [3,4].

However, decay reactions are used in the case of heavier nuclei, the study of the average properties of hadrons and the effects of FSI, for example, the study of scaling the behavior of reaction sections depending on the number of nuclear masses.

We considered thermal photons productions in these processes: $\pi^+ \pi^- \rightarrow \gamma \rho^0$, $\pi^\pm \rho^0 \rightarrow \gamma \pi^\pm$, $\rho^0 \rightarrow \gamma \pi^+ \pi^-$, $\pi^+ \pi^- \rightarrow \gamma \eta$, $\pi^\pm \eta \rightarrow \gamma \pi^\pm$, and $\pi^+ \pi^- \rightarrow \gamma \gamma$. The dependencies of differential

cross-section of processes on energy of colliding meson, transverse momentum of p_T and cosine of scattering angle of photons has been determined. The differential sections of the processes calculated without and taking into account the meson formfactor were compared.

Matrix elements, Manfelstam invariants and accounting of formfactor of mesons of considered priocesses was been given in previously in [5].

Purpose of the presented article is to determine influence of formfactor of mesons to differential cross-section of production of photons, to determine of doninant process of poroduction of thermal photons in mesons reactions. Energetic spectrums of thermal photons produced in these processes has been determined. A comparison of differential cross sections of thermal photon production processes and prompt photon production of processes of Compton scattering and annihilation of a quark-antiquark pair has been carried out [6].

II. DETERMINATION OF DOMINANT PROCESS OF

III. PRODUCTION OF THERMAL PHOTONS

a. comparison differential cross-sections of processes

Comparison of differential cross-sections of processes, calculated without and taking into account formfactor of mesons was carried out using the following formulas:

$$R_{if}(\sqrt{s}) = \frac{d\sigma_i(\sqrt{s})}{d\sigma_{if}(\sqrt{s})}, \quad R_{if}(p_T) = \frac{d\sigma_i(p_T)}{d\sigma_{if}(p_T)},$$

$$R_{ij}(\text{Cos}(\theta)) = \frac{d\sigma_i(\text{Cos}(\theta))}{d\sigma_{if}(\text{Cos}(\theta))}$$

where $i, j=1,2,3,\dots,6$ process number of production of thermal photons:

1. $\pi^+ \pi^- \rightarrow \gamma \rho^0$,
2. $\pi^\pm \rho^0 \rightarrow \gamma \pi^\pm$,
3. $\rho^0 \leftarrow \gamma + \pi^+ + \pi^-$,
4. $\pi^+ \pi^- \rightarrow \gamma \eta$,
5. $\pi^\pm \eta \rightarrow \gamma \pi^\pm$,

6. $\pi^+ \pi^- \rightarrow \gamma \gamma$, $\frac{d\sigma_i(\sqrt{s})}{dt}$, $\frac{d\sigma_i(p_T)}{dt}$ and

$\frac{d\sigma_i(\text{Cos}(\theta))}{dt}$ the differential cross-section of

processes on dependence \sqrt{s} , p_T , $\text{Cos}(\theta)$, correspondingly, calculated without taking into

account formfactor of mesons, $\frac{d\sigma_{if}(\sqrt{s})}{dt}$,

$\frac{d\sigma_{if}(p_T)}{dt}$ and $\frac{d\sigma_{if}(\text{Cos}(\theta))}{dt}$ differential cross-

sections of processes on dependence \sqrt{s} , p_T , $\text{Cos}(\theta)$,

correspondingly calculated taking into account formfactor of mesons.

Determination of dominant process of production of thermal photons was been carried out by formulas:

$$R_{ij}(\sqrt{s}) = \frac{d\sigma_i(\sqrt{s})}{d\sigma_j(\sqrt{s})}, \quad R_{ij}(p_T) = \frac{d\sigma_i(p_T)}{d\sigma_j(p_T)},$$

$$R_{ij}(\text{Cos}(\theta)) = \frac{d\sigma_i(\text{Cos}(\theta))}{d\sigma_j(\text{Cos}(\theta))}$$

I. NUMERICAL RESULTS AND THEIR DISCUSSION

a. Comparison of differential cross-sections of processes, calculated without and taking into account formfactor of mesons

1. process $\pi^+ \pi^- \rightarrow \gamma \rho^0$

Fig.1(a,b,c) represent the ratio of the dependencies of differential cross-sections of the $\pi^+ \pi^- \rightarrow \gamma \rho^0$ processes on the energy of colliding mesons, on transverse momentum, and on the cosine of the scattering angle of photon, calculated without and taking into account the formfactor of the mesons.

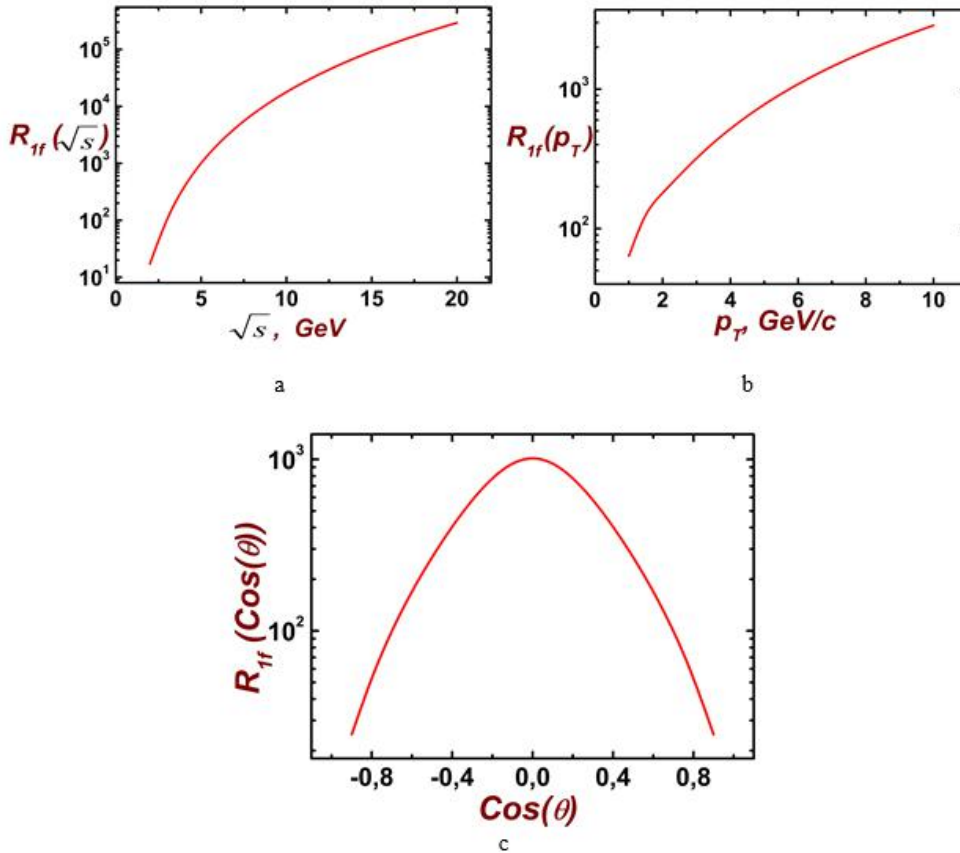


Fig. 1. (a,b,c) the rate of the dependencies of differential cross-sections of the $\pi^+ \pi^- \rightarrow \gamma \rho^0$ processes on the energy of colliding mesons (a), on the transverse momentum p_T (b), and on the cosine of scattering angle of photons (c), calculated without and taking into account the formfactor of the meson.

As can be seen from fig.1(a,b) the ratio of dependencies of differential cross-sections on energy of colliding meson, on momentum p_T calculated without and taking into account the formfactor of meson is significant at large energy values of colliding mesons and transverse momentum. As ratio of $R_{I_f} > 1$ in all values of energy \sqrt{s} and transverse momentum p_T means

$$\frac{d\sigma_1(\pi^+\pi^-\rightarrow\gamma\rho^0)}{dt} > \frac{d\sigma_{1f}(\pi^+\pi^-\rightarrow\gamma\rho^0)}{dt}$$

Ratio of dependencies of differential cross-sections of meson of process $\pi^+\pi^-\rightarrow\gamma\rho^0$ on cosine of scattering angle of photons calculated without and taking into account formfactor of mesons has symmetrical form relative to $\text{Cos}(\theta)=0$. It has a maximum at $\text{Cos}(\theta)=0$ and with an increase in the absolute value of the cosine of the angle of scattering

of photons decreases (fig.1(c)). Taking into account the formfactor of mesons in the dependence of the differential cross-section on the cosine of the scattering angle has a large effect at small values of the cosine of the angle and a small effect at the $\text{Cos}(\theta)=\pm 1$.

2. process $\pi^\pm\rho^0\rightarrow\gamma\pi^\pm$

In the fig.2 (a,b,c) is presented rate of dependencies of differential cross-sections of $\pi^\pm\rho^0\rightarrow\gamma\pi^\pm$ on energy, on transverse momentum and on cosine of scattering angle of photon, calculated without and talking into account formfactor of mesons.

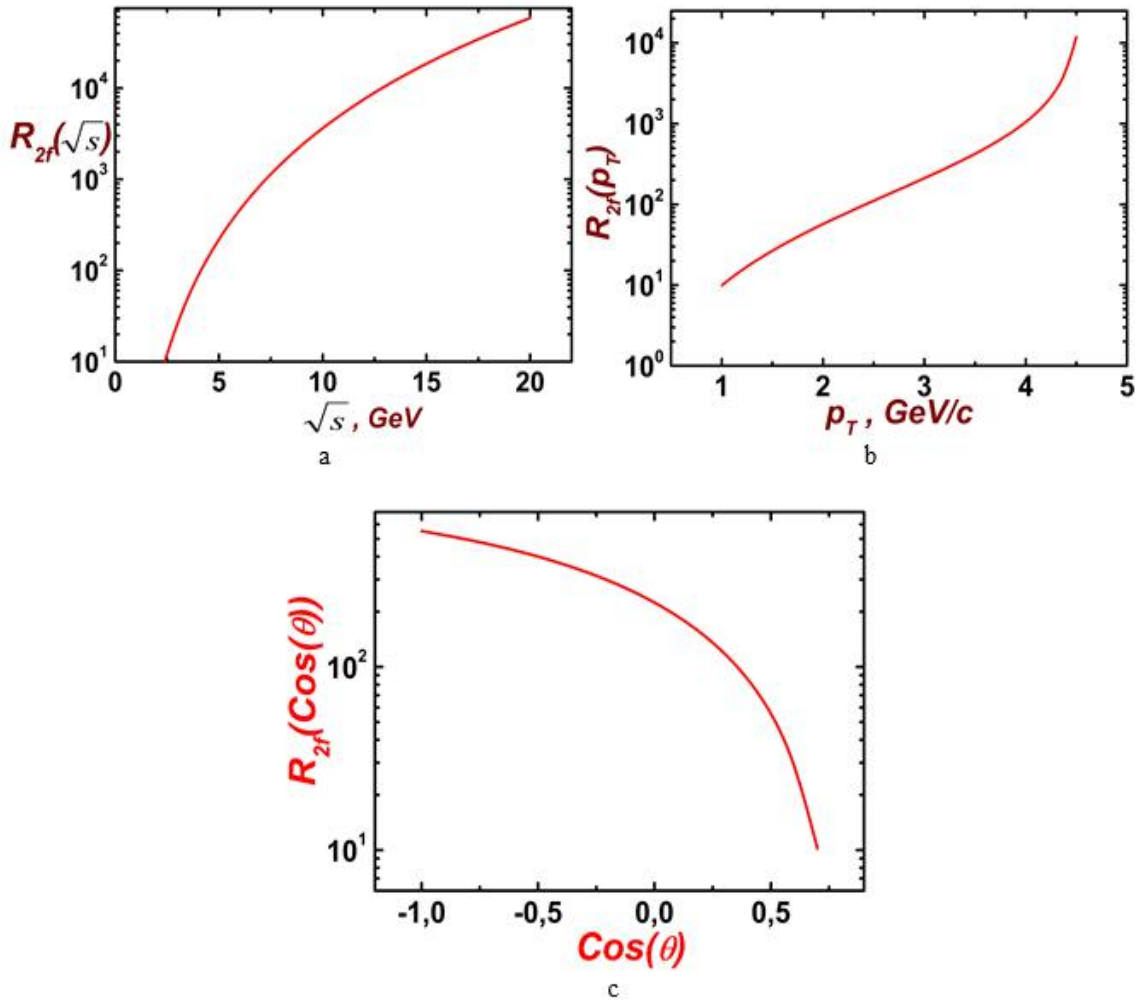


Fig.2. (a,b,c) The ratio of dependencies of differential cross-sections of process $\pi^\pm\rho^0\rightarrow\gamma\pi^\pm$ on energy colliding mesons (a), on transverse momentum (b), on cosine of scattering angle of photons (c), calculated without and talking into account formfactor of mesons.

Ratio of dependencies of differential cross-section on energy of colliding mesons and on transverse momentum decrease with increasing of energy of colliding mesons and transverse momentum. Ratio of dependencies of differential cross-section on cosine of scattering angle of photon decrease with increasing cosine of scattering angle.

As ratio of $R_f > 1$ in all values of energy \sqrt{s} and transverse momentum p_T means

$$\frac{d\sigma_1(\pi^\pm \rho^0 \rightarrow \gamma \pi^\pm)}{dt} > \frac{d\sigma_{1f}(\pi^\pm \rho^0 \rightarrow \gamma \pi^\pm)}{dt}$$

Thus, taking into account the meson formfactor reduces the differential cross-section of process.

3. process $\rho^0 \rightarrow \gamma \pi^+ \pi^-$

Fig.3 (a,b,c) represent the dependence of rate of the differential cross-section of $\rho^0 \rightarrow \gamma \pi^+ \pi^-$ process on energy of colliding mesons \sqrt{s} , on the transverse momentum p_T and on the cosine of the scattering angle of photons, calculated without and taking into account the formfactor of mesons.

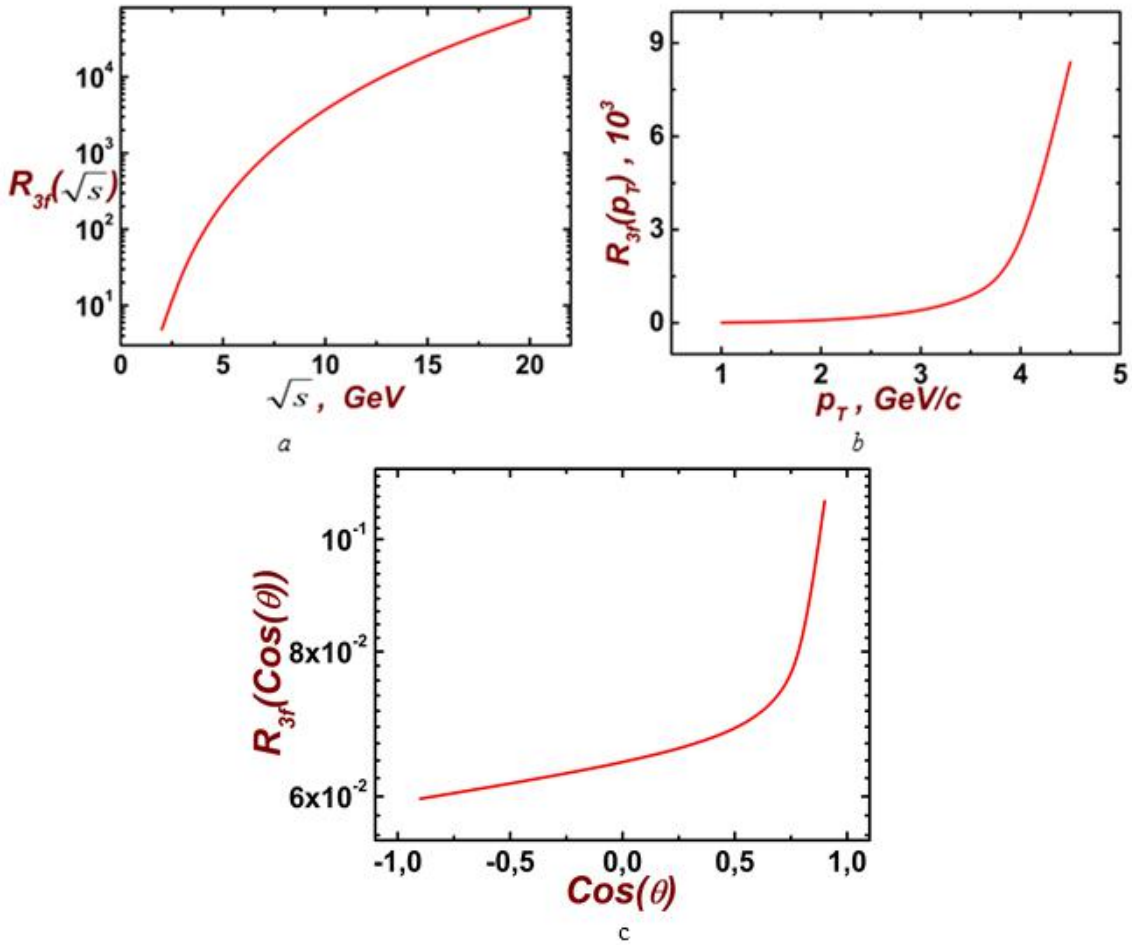


Fig.3. (a,b,c) the dependence of rate of the differential cross-section of $\rho^0 \rightarrow \gamma \pi^+ \pi^-$ process on the energy of colliding mesons \sqrt{s} (a), on the transverse momentum p_T (b) and on the cosine of the angle of the scattering photon (c), calculated taking into account the formfactor of mesons.

3. Determination of dominant process

1. Comparison of processes $\pi^+ \pi^- \rightarrow \gamma \rho^0$, $\pi^\pm \rho^0 \rightarrow \gamma \pi^\pm$ and $\pi^+ \pi^- \rightarrow \gamma \gamma$

1.1 Comparison of processes $\pi^+ \pi^- \rightarrow \gamma \rho^0$, $\pi^\pm \rho^0 \rightarrow \gamma \pi^\pm$

Fig.4(a,b,c) represent the ratio of dependencies differential cross-section of $\pi^+\pi^-\rightarrow\gamma\rho^0$ and $\pi^\pm\rho^0\rightarrow\gamma\pi^\pm$ on energy colliding mesons \sqrt{s} , transverse momentum p_T and cosine of scattering angle of photons.

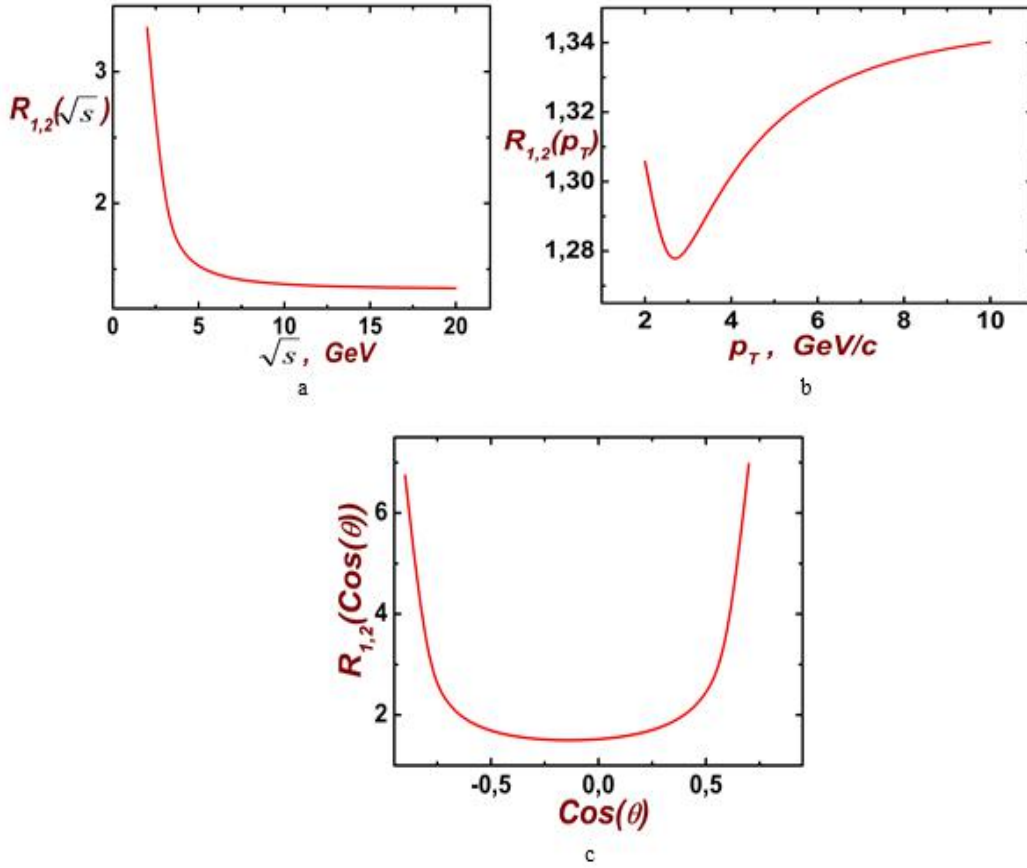


Fig.4. (a,b,c) the dependence ratio of differential cross-sections of the $\pi^+\pi^-\rightarrow\gamma\rho^0$ and

$\pi^\pm\rho^0\rightarrow\gamma\pi^\pm$ processes calculated without and taking into account the formfactor of mesons on the energy of colliding mesons (a), on the transverse momentum of photons (b) and on the cosine of the scattering angle of photons (c).

As see from fig.4 (a) ratio of dependencies of differential cross-section of $\pi^+\pi^-\rightarrow\gamma\rho^0$ and $\pi^\pm\rho^0\rightarrow\gamma\pi^\pm$ on energy of colliding mesons is significant at low energies of colliding mesons. Also rate of dependencies of differential cross-sections of $\pi^+\pi^-\rightarrow\gamma\rho^0$ and $\pi^\pm\rho^0\rightarrow\gamma\pi^\pm$ on energy of colliding mesons large 1 for all values of energy and consequently

$$\frac{d\sigma(\pi^+\pi^-\rightarrow\gamma\rho^0)}{dt} > \frac{d\sigma(\pi^\pm\rho^0\rightarrow\gamma\pi^\pm)}{dt}$$

1.2 Comparison of processes $\pi^+\pi^-\rightarrow\gamma\rho^0$ and $\pi^+\pi^-\rightarrow\gamma\gamma$

Fig.5 (a,b,c) represent the ratio of dependencies differential cross-section of processes $\pi^+\pi^-\rightarrow\gamma\rho^0$ and $\pi^+\pi^-\rightarrow\gamma\gamma$ on energy colliding mesons, transverse momentum p_T and cosine of the scattering angle of photons.

As see from fig.5(a) ratio of dependencies of differential cross-section of $\pi^+\pi^-\rightarrow\gamma\rho^0$ and $\pi^+\pi^-\rightarrow\gamma\gamma$ on energy of colliding mesons is significant at low values energies of colliding mesons. Moreover, ratio of dependencies of differential cross-sections of $\pi^+\pi^-\rightarrow\gamma\rho^0$ and $\pi^+\pi^-\rightarrow\gamma\gamma$ on energy of colliding mesons for all values of energy large 1 and consequently

$$\frac{d\sigma(\pi^+\pi^-\rightarrow\gamma\rho^0)}{dt} > \frac{d\sigma(\pi^+\pi^-\rightarrow\gamma\gamma)}{dt}$$

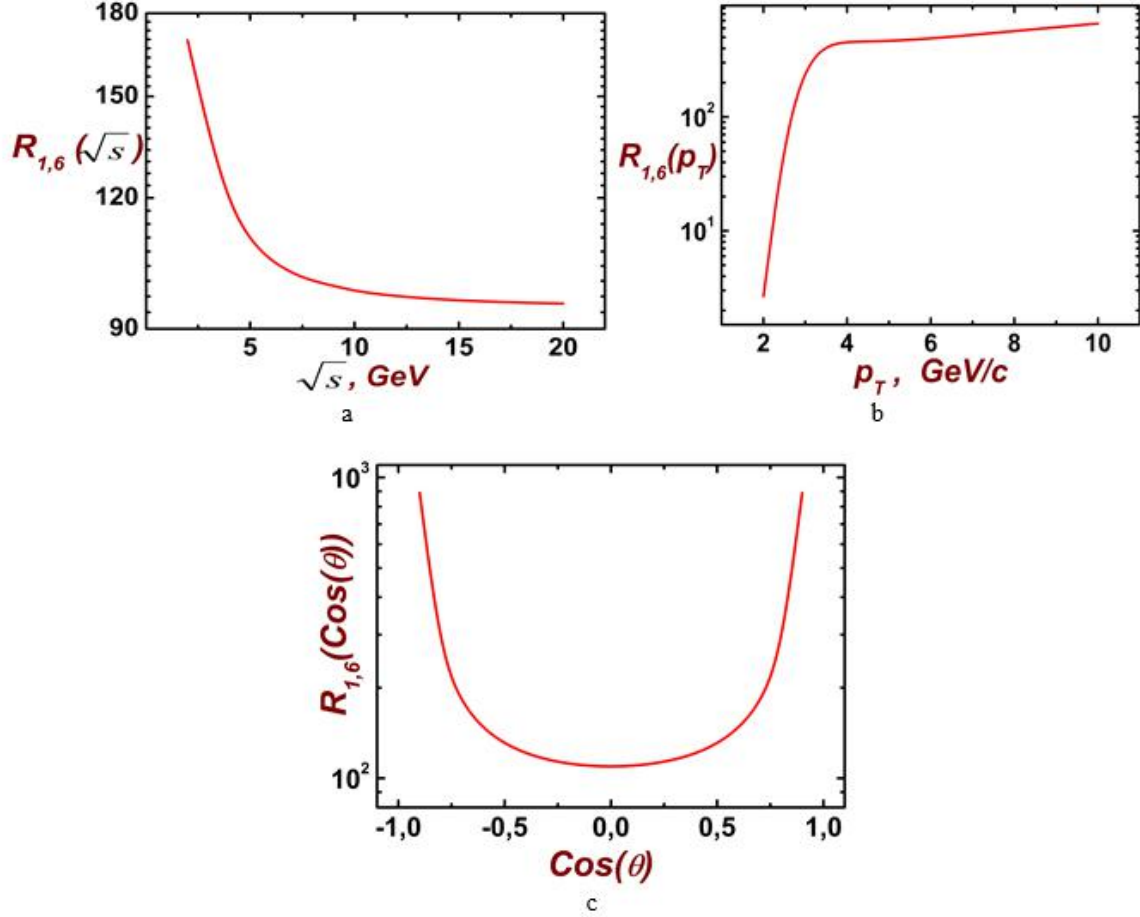


Fig. 5. (a,b,c) the dependence of the rate of differential cross-sections of the processes $\pi^+\pi^-\rightarrow\gamma\rho^0$ and $\pi^+\pi^-\rightarrow\gamma\gamma$ on the energy of colliding mesons (a), on transverse momentum p_T (b) and on cosine of the scattering angle of photons (c).

As see from fig.5 (b) ratio of dependencies of differential cross-section of $\pi^+\pi^-\rightarrow\gamma\rho^0$ and $\pi^+\pi^-\rightarrow\gamma\gamma$ on p_T is significant at big values of energies of colliding mesons. Also rate of dependencies of differential cross-sections of $\pi^+\pi^-\rightarrow\gamma\rho^0$ and $\pi^+\pi^-\rightarrow\gamma\gamma$ on p_T large 1 for all values of p_T and consequently

$$\frac{d\sigma(\pi^+\pi^-\rightarrow\gamma\rho^0)}{dt} > \frac{d\sigma(\pi^+\pi^-\rightarrow\gamma\gamma)}{dt}$$

In the fig.6 shown the dependencies of ratio of differential cross-section of process $\pi^+\pi^-\rightarrow\gamma\rho^0$, $\pi^\pm\rho^0\rightarrow\gamma\pi^\pm$ and $\pi^+\pi^-\rightarrow\gamma\gamma$ to their sum.

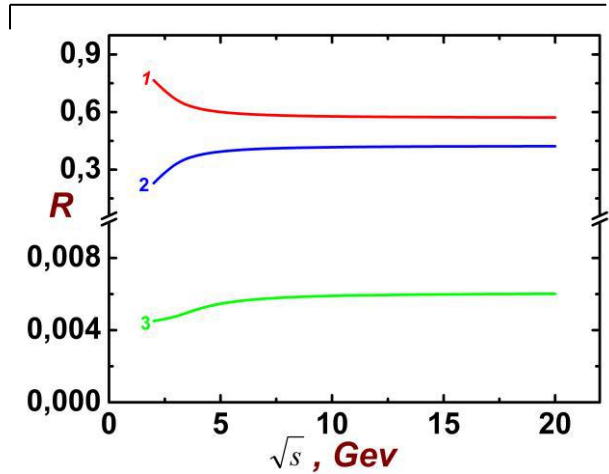


Fig. 6. Dependencies of ratio of differential cross-section of process $\pi^+\pi^-\rightarrow\gamma\rho^0$, $\pi^\pm\rho^0\rightarrow\gamma\pi^\pm$ and $\pi^+\pi^-\rightarrow\gamma\gamma$ to their sum on energy of colliding mesons \sqrt{s} , corresponding curve 1,2, and 3.

As seen from fig.6 contribution of process $\pi^+\pi^-\rightarrow\gamma\rho^0$ to total differential cross-section of production of thermal photons is significant.

Influence of contributions of all processes is significant at small value of energy of colliding mesons. Thus, the following ratio is satisfied:

$$\frac{d\sigma(\pi^+\pi^-\rightarrow\gamma\rho^0)}{dt} > \frac{d\sigma(\pi^\pm\rho^0\rightarrow\gamma\pi^\pm)}{dt} > \frac{d\sigma(\pi^+\pi^-\rightarrow\gamma\gamma)}{dt}$$

1.3 Comparison of processes $\pi^+\pi^-\rightarrow\gamma\eta$, $\pi^\pm\eta\rightarrow\gamma\pi^\pm$

$$\frac{d\sigma(\pi^+\pi^-\rightarrow\gamma\eta)}{dt} > \frac{d\sigma(\pi^\pm\eta\rightarrow\gamma\pi^\pm)}{dt}$$

Fig.7 (a,b,c) represent the ratio of dependencies of differential cross-section of processes $\pi^+\pi^-\rightarrow\gamma\eta$ and $\pi^\pm\eta\rightarrow\gamma\pi^\pm$ on energy of colliding mesons \sqrt{s} , transverse momentum p_T and cosine of scattering angle of photons.

As see from fig.7 (c) ratio of dependencies of differential cross-sections of processes $\pi^+\pi^-\rightarrow\gamma\eta$ and $\pi^\pm\eta\rightarrow\gamma\pi^\pm$ on cosine of scattering angle photon is large 1 and constant. It does not depend on the cosine of scattering angle of photons.

As see from fig.7 (a,b,c) at all dependencies of differential cross-section on energy of colliding mesons, transverse momentum p_T and cosine scattering angle of photons

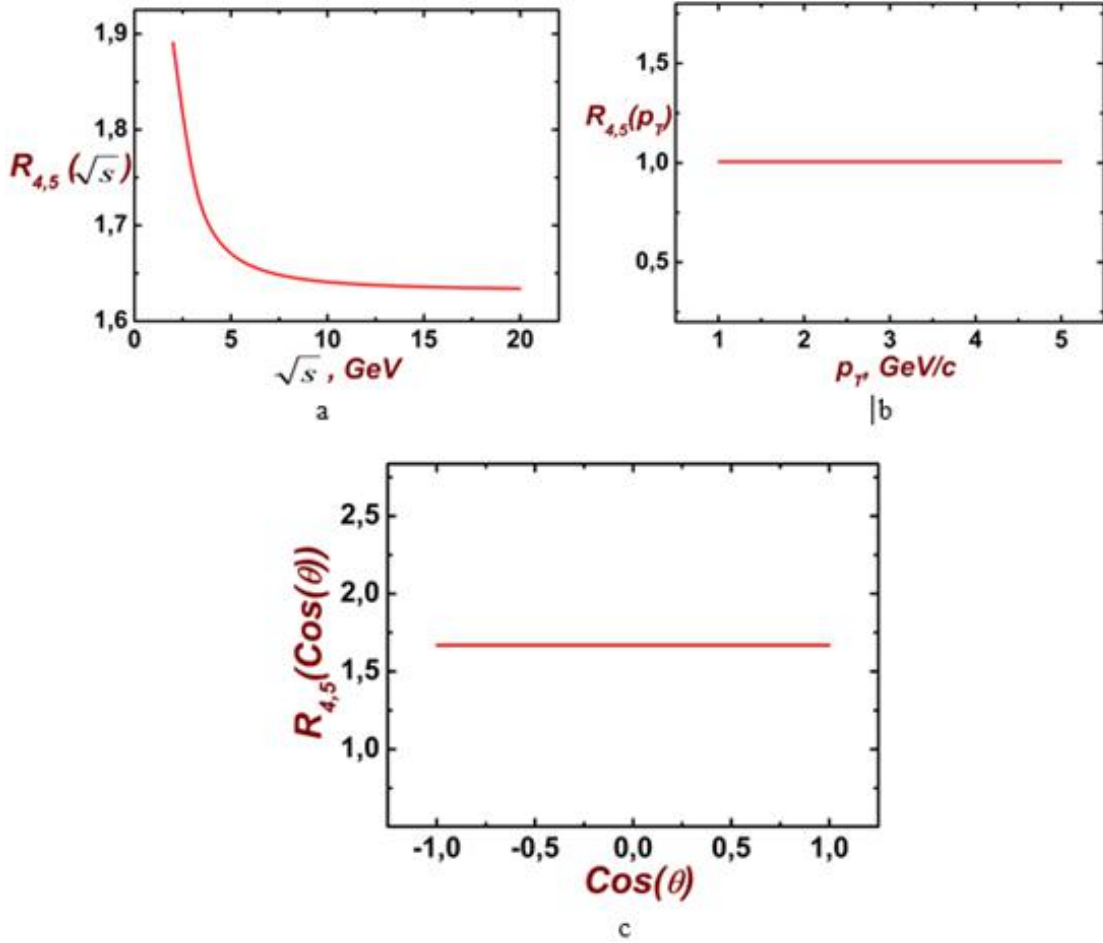


Fig.7. (a,b,c) the dependencies of the ratio of the differential cross-sections of the processes $\pi^+\pi^-\rightarrow\gamma\eta$ and $\pi^\pm\eta\rightarrow\gamma\pi^\pm$ on the energy of colliding mesons \sqrt{s} (a), on transverse momentum p_T (b) and on cosine of the scattering angle of photons (c).

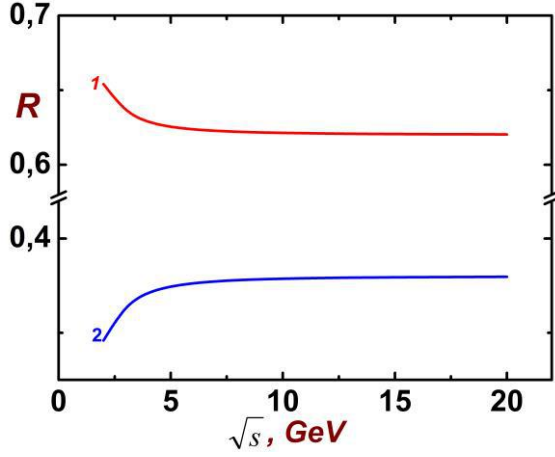


Fig.8. The dependencies of ratio of differential cross-section of process $\pi^+\pi^-\rightarrow\gamma\eta$ and $\pi^\pm\eta\rightarrow\gamma\pi^\pm$ to their sum on energy of colliding mesons, corresponding curve 1 and 2.

In the fig.8 shown the dependencies of ratio of differential cross-section of process $\pi^+\pi^-\rightarrow\gamma\eta$ and $\pi^\pm\eta\rightarrow\gamma\pi^\pm$ to their sum.

As seen from fig.8 contribution of process $\pi^+\pi^-\rightarrow\gamma\eta$ to total differential cross-section production of thermal photons is significant. Influence of contributions of all processes is significant at small value of energy of colliding mesons. Thus, the following ratio is satisfied:

$$\frac{d\sigma(\pi^+\pi^-\rightarrow\gamma\eta)}{dt} > \frac{d\sigma(\pi^\pm\eta\rightarrow\gamma\pi^\pm)}{dt}$$

c. Energy spectrum of produced thermal photons in processes

On fig.9 schematically has been shown thermal photon production processes with participation of mesons: $\pi^+\pi^-\rightarrow\gamma\rho^0$, $\pi^\pm\rho^0\rightarrow\gamma\pi^\pm$, $\pi^+\pi^-\rightarrow\gamma\eta$, $\pi^\pm\eta\rightarrow\gamma\pi^\pm$, $\pi^+\pi^-\rightarrow\gamma\gamma$.

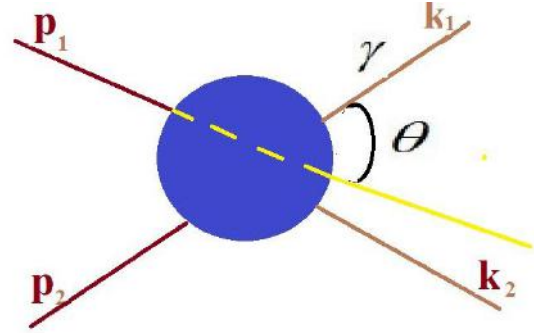


Fig. 9. Scheme of thermal photon production in processes

$$\begin{aligned} &\pi^+\pi^-\rightarrow\gamma\rho^0, \pi^\pm\rho^0\rightarrow\gamma\pi^\pm, \\ &\pi^+\pi^-\rightarrow\gamma\eta, \pi^\pm\eta\rightarrow\gamma\pi^\pm, \\ &\pi^+\pi^-\rightarrow\gamma\gamma. \end{aligned}$$

It has been introduced the following designations: $c' \equiv \cos\theta = \cos(k_1 \wedge p_1)$.

We write the law of conservation of momentum:

$$\vec{p}_1 + \vec{p}_2 = \vec{k}_1 + \vec{k}_2, \quad \vec{k}_2 = \vec{p}_1 + \vec{p}_2 - \vec{k}_1$$

and the law of energy conservation:

$$E_1 + E_2 - E_{k_1} - E_{k_2} = 0$$

The law of conservation of energy in 4-dimensional coordinates will be:

$$p_1^0 + p_2^0 - \sqrt{k_1^2} - \sqrt{(p_2 + p_1 - k_1)^2 + m_{k_2}^2} = 0$$

Last equation has been squared to determine the momentum of a thermal photons

$$p_1^0 + p_2^0 - k_1 - \sqrt{p_1^2 + k_1^2 - 2|p_1|k_1c + m_{k_2}^2} = 0$$

Let's take $x=k_1$ and square the previous expression

$$m_{p_1}^2 + m_{p_2}^2 - 2(p_2^0 + p_1^0)\sqrt{x^2} = -2|p_1|xc$$

$$m_{p_1}^2 + m_{p_2}^2 + 2|p_1|xc = 2(p_2^0 + p_1^0)\sqrt{x^2}$$

Let's square the previous expression again

$$\begin{aligned} &(m_{p_1}^2 + m_{p_2}^2)^2 + 4|p_1|xc(m_{p_1}^2 + m_{p_2}^2) + 4|p_1|^2x^2c^2 = 4(p_2^0 + p_1^0)^2x^2 \\ &(4|p_1|^2c^2 - 4(p_2^0 + p_1^0)^2)x^2 + 4|p_1|c(m_{p_1}^2 + m_{p_2}^2)x + (m_{p_1}^2 + m_{p_2}^2)^2 = 0 \end{aligned}$$

We get a quadratic equation with respect to the momentum of the produced thermal photons x , with coefficients:

$$a = 4|\vec{p}_1|^2 c^2 - 4(p_2^0 + p_1^0)^2, \quad b = 4|\vec{p}_1|c(m_{p_1}^2 + m_{p_2}^2), \quad c = (m_{p_1}^2 + m_{p_2}^2)^2$$

Considering the following expressions

$$p_1^0 = E_1^2 = \vec{p}_1^2 + m_{p_1}^2; \quad p_2^0 = E_2^1 = \vec{p}_2^2 + m_{p_2}^2 = m_{p_2}^2;$$

$$|\vec{p}_1|^2 = E_1^2 - m_{p_1}^2;$$

The solution to this quadratic equation will be as follows:

$$x_{1,2} = \frac{-4c(m_{p_1}^2 + m_{p_2}^2)\sqrt{E_1^2 - m_{p_1}^2} \pm \sqrt{16c^2(E_1^2 - m_{p_1}^2)(m_{p_1}^2 + m_{p_2}^2)^2 - 4(4c^2(E_1^2 - m_{p_1}^2) - 4c^2(E_1^2 + m_{p_1}^2)^2)(m_{p_1}^2 + m_{p_2}^2)^2}}{2(4c^2(E_1^2 - m_{p_1}^2) + 4c^2(E_1^2 + m_{p_1}^2)^2)}$$

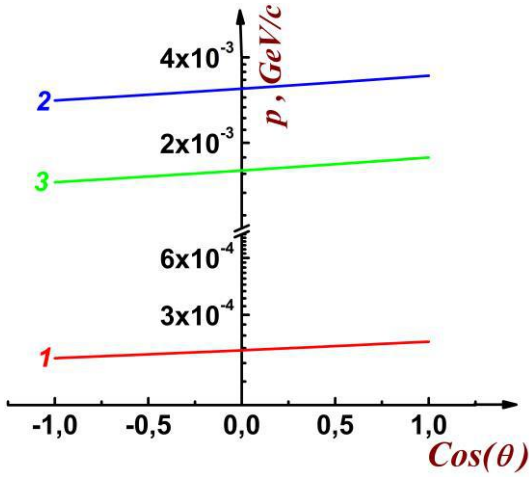


Fig. 10. The dependence of momentum of produced thermal photons in processes $\pi^+\pi^- \rightarrow \gamma\rho^0$, $\pi^+\pi^- \rightarrow \gamma\eta$, $\pi^+\pi^- \rightarrow \gamma\gamma$ (curve 1), $\pi^\pm\rho^0 \rightarrow \gamma\pi^\pm$ (curve 2), $\pi^\pm\eta \rightarrow \gamma\pi^\pm$ (curve 3) on cosine of scattering angle of photons.

We will consider those solutions of the equation that are not complex, i.e. the discriminant of the equation is greater than zero and is equal to zero, in this case the solution x_2 satisfies this condition. Data to estimate the dependence of energy of produced of thermal photons on the energy of colliding protons were taken $E_i=10$ GeV, $\vec{p}_2=0$. For processes $\pi^+\pi^- \rightarrow \gamma\rho^0$, $\pi^+\pi^- \rightarrow \gamma\eta$,

$\pi^+\pi^- \rightarrow \gamma\gamma$ m_{p_1}, m_{p_2} - mass of π - mesons, for processes $\pi^\pm\rho^0 \rightarrow \gamma\pi^\pm$, $\pi^\pm\eta \rightarrow \gamma\pi^\pm$, m_{p_1} - mass of π - meson, m_{p_2} - mass of ρ^0 or η mesons. In the fig.10 the dependence of momentum on cosine of scattering angle of thermal photons is presented.

As seen from fig.10 the dependence of momentum on cosine of scattering angle of photons is linear. Energy of produced photons also have linear dependence on cosine of scattering angle of photons. Energy of produced photons change in the interval of [0.177, 3.446] MeV, which corresponds to the temperature interval of [2.952, 3.995] 10^9 K.

CONCLUSIONS

The consideration of the formfactor of mesons in the calculations of the differential cross section of the processes of production of thermal photons showed that it reduces the differential cross section of the processes. Influence of formfactor of mesons to differential cross section of process decreases with increasing energy of colliding mesons. There is a significant influence of the form factor of meson on the differential cross section at small values of the energy of the colliding particles and the transverse momentum.

Thus, it has been shown that for processes $\pi^+\pi^- \rightarrow \gamma\rho^0$, $\pi^\pm\rho^0 \rightarrow \gamma\pi^\pm$ and $\pi^+\pi^- \rightarrow \gamma\gamma$ the following ratio is satisfied

$$\frac{d\sigma(\pi^+\pi^- \rightarrow \gamma\rho^0)}{dt} > \frac{d\sigma(\pi^\pm\rho^0 \rightarrow \gamma\pi^\pm)}{dt} > \frac{d\sigma(\pi^+\pi^- \rightarrow \gamma\gamma)}{dt}$$

Thus, it has been shown that for processes $\pi^+\pi^- \rightarrow \gamma\eta$, $\pi^\pm\eta \rightarrow \gamma\pi^\pm$ the following ratio is satisfied

$$\frac{d\sigma(\pi^+\pi^- \rightarrow \gamma\rho^0)}{dt} > \frac{d\sigma(\pi^\pm\rho^0 \rightarrow \gamma\pi^\pm)}{dt}$$

Energetic spectrum of produced photons indicate to temperature quark gluon plasma, formed at meson-meson collision. Transverse momentum of photons linear depends on cosine of scattering angle of photons. It is more likely to detect photons with a large transverse momentum at large values of the cosine of the scattering angle.

A comparison of differential cross sections of thermal photon production processes and prompt photon production of processes of Compton scattering and annihilation of a quark-antiquark pair [6] showed that they are of the same order. Thermal photons contribute significantly to the spectrum of photons at $P_T < 3 \text{ GeV}$

All mathematical calculations were performed in Mathematica 10 and FeynCalc. Feynman diagrams are constructed using JaxoDraw 2. The graphs are constructed using the Origin 9 program and edited using the Adobe Photoshop 8.

-
- [1] *J. Kapusta, P. Lichard, D. Seibert.* High energy photons from quark-gluon plasma versus hot hadronic gas. Nuclear Physics A 544, 485 (1992)
- [2] *J. Kapusta, P. Lichard, D. Seibert.* High-energy photons from quark-gluon plasma versus hot hadronic gas. Phys.Rev. D 44, 2774, 1991.
- [3] *V. Cerny, P. Lichard and J. Pisut.* Z. Phys. C31, 163 (1986). LIU Fuming Explore QCD phase transition with thermal photons. Nuclear Science and Techniques 24, 050524, 2013.
- [4] *P. Arnold, G.D. Moore, L.G. Yaffe.* Photon emission from ultrarelativistic plasmas. JHEP 11, 057 (2011)
- [5] *M.R. Alizada, A.I. Ahmadov.* Thermal photons production in proton-proton collisions at high energies. Part I. Differential cross-sections of processes, calculated without and taking into account formfactor of mesons. Azerbaijan Journal of Physics "Fizika", XIX, 1, 2023, section En.
- [6] *M.R. Alizada, A.I. Ahmadov, A.B. Arbuzov.* The investigation of direct photon production subprocesses $qg \rightarrow q\gamma$ at $q\bar{q} \rightarrow g\gamma$ proton-proton collision. Proceedings of Azerbaijan National Academy of Sciences, series of physico-technical and math sciences, physics and astronomy, 2021, 5, 11.

Received: 16.01.2023

INSTABILITY OF THERMOMAGNETIC WAVES IN CONDUCTING MEDIA

E.R. HASANOV^{1,2}, Sh.G. KHALILOVA², G.M. MAMMADOVA²

¹Baku State University Acad. Z. Khalilov, str.23, Baku, Azerbaijan Republic

²Institute of Physics, Ministry of Science and Education of Azerbaijan Republic, AZ-1143, H. Javid 131, Baku, shahlaganbarova@gmail.com

It is shown that when choosing the crystal symmetry, if the wave vector of the wave and the temperature gradient are oriented arbitrarily, waves of a thermomagnetic nature of the same frequency and growth rate are possibly excited.

Keywords: Gunn’s effect, thermomagnetic wave, conducting media, instability.

PACS: 78,55, 73.22.CD, 73.22

INTRODUCTION

It was shown in [1] that hydrodynamic motions in a nonequilibrium plasma, in which there is a constant temperature gradient ($\nabla T = const$), has oscillatory properties. This property of plasma is very different from ordinary plasma. Without an external magnetic field and hydrodynamic motions, transverse “thermomagnetic” waves are possible in it, in which only the magnetic field oscillates. In the presence of an external magnetic field, the wave vector of thermomagnetic waves is perpendicular to the magnetic field and lies in the plane ($\vec{H}, \vec{\nabla}T$). If a weak magnetic field appears in such a plasma, i.e. $\Omega\tau \ll 1$ (Ω -Larmor frequency of electrons, τ -time of collision of electrons) inside the plasma arises in addition to the external electric field, the electric is proportional to the temperature gradient, the electric

field is proportional to the magnetic field. Due to this complex electric field, thermomagnetic waves of a transverse $\vec{k} \perp \vec{\nabla}T$ (\vec{k} -wave vector) and longitudinal character $\vec{k} \parallel \vec{\nabla}T$ are excited. A theoretical study of these thermomagnetic waves in isotropic conducting media of the electric type of charge carriers was carried out in [2-5]. However, in anisotropic conducting media, there is no theoretical study of thermomagnetic waves. In this theoretical work, we will investigate thermomagnetic waves in anisotropic conducting media with selected samples.

BASIC EQUATIONS OF THE PROBLEM

In the presence of an external magnetic field and a temperature gradient in an isotropic solid, the total electric field has the form

$$\vec{E} = \zeta \vec{j} + \zeta' [\vec{j} \vec{H}] + \zeta'' (\vec{j} \vec{H}) \vec{H} + \Lambda \frac{\partial T}{\partial x} + \Lambda' [\vec{\nabla} T \vec{H}] + \Lambda'' ([\vec{\nabla} T \vec{H}]) \vec{H} \tag{1}$$

\vec{j} - current flux density

In anisotropic conducting media, all coefficients in equation (1) are tensors.

Then the equations for anisotropic conducting media will have the form:

$$E_i = \zeta_{ik} \vec{j}_k + \zeta'_{ik} [\vec{j} \vec{H}]_k + \zeta''_{ik} (\vec{j} \vec{H}) \vec{H}_k + \Lambda_{ik} \frac{\partial T}{\partial x_k} + \Lambda'_{ik} [\vec{\nabla} T \vec{H}]_k + \Lambda''_{ik} ([\vec{\nabla} T \vec{H}]) \vec{H}_k \tag{2}$$

Here ζ_{ik} is the tensor of the reciprocal of the ohmic resistance, Λ_{ik} is the differential thermoelectric power, and Λ'_{ik} is the Nernst-Ettinghausen coefficient. We will consider a solid external magnetic field $\vec{H}_0 = 0$. Then, in the equations, the terms containing are equal to zero. Taking into account Maxwell's equation, we obtain the following system of equations

$$\begin{cases} E'_i = \zeta_{ik} j'_k + \Lambda'_{ik} [\nabla T H]_k \\ rot \vec{E}' = -\frac{1}{c} \frac{\partial \vec{H}'}{\partial t} \\ rot \vec{H}' = \frac{4\pi}{c} \vec{j}' + \frac{1}{c} \frac{\partial \vec{E}'}{\partial t} \end{cases} \tag{3}$$

Assuming that all variable quantities are monochromatic in nature, i.e.

$$(E', H', j) \sim e^{i(\vec{k}\vec{r} - \omega t)} \tag{4}$$

From (3) it turns out:

$$E'_i = \zeta_{ik} j'_{ik} + \Lambda'_{ik} \left[\vec{\nabla} T \vec{H} \right]_k \quad (5)$$

$$j'_k = \frac{ic^2}{4\pi\varpi} \left[\vec{k} \left[\vec{k} \vec{E}' \right] \right]_k + \frac{i\varpi}{4\pi} E'_k$$

(ϖ - oscillation frequency).

THEORY

We (5) it turns out:

$$E'_i = \frac{ic^2}{4\pi\varpi} \zeta_{ik} \left(\vec{k} \vec{E}' \right)_k + \frac{i\varpi^2 - ic^2 k^2}{4\pi\varpi} \zeta_{ik} E'_k + \frac{c\Lambda'_{ik}}{\varpi} \left(\vec{\nabla} T E' \right)_k - \frac{c\Lambda'_{ik}}{\varpi} \left(\vec{k} \vec{\nabla} T \right)_k E'_i \quad (6)$$

To obtain the dispersion equation from (6), you first need to choose a coordinate system. We will choose the following coordinate system

$$k_1 \neq 0, \quad k_2 = k_3 = 0, \quad \frac{\partial T}{\partial x_2} \neq 0, \quad \frac{\partial T}{\partial x_3} = 0 \quad (7)$$

Taking into account (7), from (6) it turns out:

$$E'_i = \left(A \zeta_{ik} k_e k_k + B \zeta_{ik} + \frac{c\Lambda'_{ik}}{\varpi} k_e \frac{\partial T}{\partial x_k} \right) E'_k \quad (8)$$

When obtaining (8) from (7), we assumed that $\vec{k} \perp \vec{\nabla} T$ i.e. the resulting thermomagnetic waves are transverse.

$$\text{At } E'_i = \delta_{ik} E'_k, \quad \delta_{ik} = \begin{cases} 1, & i = k \\ 0, & i \neq k \end{cases} \quad (9)$$

From (8) we obtain the following dispersion equations in tensor form

$$N_{ik} = A \zeta_{ie} k_e k_k + B \zeta_{ik} + \frac{c\Lambda'_{ie}}{\varpi} k_e \frac{\partial T}{\partial x_k} \quad (10)$$

$$A = \frac{ic^2}{4\pi\varpi}, \quad B = \frac{i\varpi^2 - ic^2 k^2}{4\pi\varpi}$$

Expanding by components (10) it turns out:

$$\begin{aligned} \left| (N_{ik} - \delta_{ik}) \right| &= (N_{11} - I)(N_{22} - I)(N_{33} - I) + \\ &+ N_{31} N_{12} N_{23} + N_{21} N_{32} N_{13} - N_{31} N_{13} (N_{22} - I) - \\ &- N_{32} N_{23} (N_{11} - I) - N_{21} N_{12} (N_{33} - I) = 0 \end{aligned} \quad (11)$$

Here:

$$\begin{aligned} N_{11} &= \frac{i\varpi}{4\pi} \zeta_{11}, \quad N_{12} = \frac{(i\varpi^2 - ic^2 k^2) \zeta_{12} + 4\pi c \Lambda'_{12} k \nabla_2 T}{4\pi\varpi}, \quad N_{13} = \frac{i\varpi^2 - ic^2 k^2}{4\pi\varpi} \zeta_{13}, \quad N_{21} = \frac{i\varpi}{4\pi} \zeta_{21}, \\ N_{22} &= \frac{(i\varpi^2 - ic^2 k^2) \zeta_{22} + 4\pi c \Lambda'_{21} k \nabla_2 T}{4\pi\varpi}, \quad N_{23} = \frac{i\varpi^2 - ic^2 k^2}{4\pi\varpi} \zeta_{23}, \end{aligned} \quad (12)$$

$$N_{31} = \frac{i\varpi}{4\pi} \zeta_{31}, \quad N_{32} = \frac{(i\varpi^2 - ic^2 k^2) \zeta_{32} + 4\pi c \Lambda'_{31} k \nabla_2 T}{4\pi\varpi}, \quad N_{33} = \frac{i\varpi^2 - ic^2 k^2}{4\pi\varpi} \zeta_{33}$$

$$\begin{aligned} N_{11} &= \frac{i\varpi}{4\pi} \zeta_{11}, \quad N_{12} = \frac{(i\varpi^2 - ic^2 k^2) \zeta_{12} + 4\pi c \Lambda'_{12} k \nabla_2 T}{4\pi\varpi}, \quad N_{13} = \frac{i\varpi^2 - ic^2 k^2}{4\pi\varpi} \zeta_{13}, \quad N_{21} = \frac{i\varpi}{4\pi} \zeta_{21}, \\ N_{22} &= \frac{(i\varpi^2 - ic^2 k^2) \zeta_{22} + 4\pi c \Lambda'_{21} k \nabla_2 T}{4\pi\varpi}, \quad N_{23} = \frac{i\varpi^2 - ic^2 k^2}{4\pi\varpi} \zeta_{23}, \quad N_{31} = \frac{i\varpi}{4\pi} \zeta_{31}, \end{aligned}$$

$$N_{32} = \frac{(i\omega^2 - ic^2k^2)\zeta_{32} + 4\pi c\Lambda'_{32}k\nabla_2 T}{4\pi\omega}, \quad N_{33} = \frac{i\omega^2 - ic^2k^2}{4\pi\omega}\zeta_{33}$$

Putting (12) into (11), we obtain the following equation for the oscillation frequency inside an anisotropic body

$$\Psi_5\omega^5 + \Psi_4\omega^4 + \Psi_3\omega^3 + \Psi_2\omega^2 + \Psi_1\omega + \Psi = 0 \quad (13)$$

Solution (13) in a general form is not possible and therefore we will not write out the expression $\Psi, \Psi_1, \Psi_2, \Psi_3, \Psi_4, \Psi_5$.

To solve the dispersion equation (11), we will choose crystals satisfying the following conditions.

$$1) \quad N_{11} = N_{21} = N_{31}, \quad 2) \quad N_{21} = N_{32} = N_{22} \quad 3) \quad N_{13} = N_{23} = N_{33} \quad (14)$$

A crystal satisfying conditions (14) is diagonal.

Taking into account (14), from (11) we easily obtain

$$N_{11} + N_{22} + N_{33} = I \quad (15)$$

If

$$\zeta_{11} = \zeta_{22} = \zeta_{33} = \zeta \quad (16)$$

from (15) we get

$$\frac{3}{4\pi}\zeta\omega^2 - \frac{c^2k^2}{2\pi}\zeta + i\omega'_{21} = 0 \quad (17)$$

$$\omega'_{21} = -c\Lambda'_{21}k_1\nabla_2 T$$

From (17) we get:

$$\omega = \omega_0 + i\gamma = \frac{\sqrt{2}}{3} \left(\frac{6\pi|\omega'_{21}|}{\zeta} + c^2k^2 \right)^{1/2} + i \frac{\sqrt{2}}{3} \left(\frac{6\pi|\omega'_{21}|}{\zeta} - c^2k^2 \right)^{1/2} \quad (18)$$

It can be seen from (18) that at $c^2k^2 > \frac{6\pi\omega'_{21}}{\zeta}$, the exciting wave is of a purely electromagnetic nature.

When $c^2k^2\zeta < 6\pi|\omega'_{21}|$ the excited wave is growing thermomagnetic with a frequency

$$\omega_0 = \left(\frac{4\pi\omega'_{21}}{\zeta} \right)^{1/2} \left(1 + \frac{1}{12\pi} \frac{c^2k^2\zeta}{|\omega'_{21}|} \right) \text{ and increment } \gamma = \left(\frac{4\pi\omega'_{21}}{\zeta} \right)^{1/2} \left(1 - \frac{1}{12\pi} \frac{c^2k^2\zeta}{|\omega'_{21}|} \right)$$

For $\vec{k} \parallel \vec{\nabla}T$ from (11), consider the case

$$1) \quad N_{11} = N_{21} = N_{31}, \quad 2) \quad N_{13} = N_{32} = N_{33} = N_{23} = N_{13} \quad (19)$$

$$N_{11} = \frac{i\omega}{4\pi}\zeta_{11}, \quad N_{12} = \frac{(i\omega^2 - ic^2k^2)\zeta_{12} - 4\pi c\Lambda'_{12}k\nabla_2 T}{4\pi\omega}, \quad N_{13} = \frac{(i\omega^2 - ic^2k^2)\zeta_{13} - 4\pi c\Lambda'_{12}k\vec{\nabla}T}{4\pi\omega}, \quad N_{21} = \frac{i\omega}{4\pi}\zeta_{21},$$

$$N_{22} = \frac{(i\omega^2 - ic^2k^2)\zeta_{22} - 4\pi c\Lambda'_{22}k\vec{\nabla}T}{4\pi\omega}, \quad N_{23} = \frac{(i\omega^2 - ic^2k^2)\zeta_{23} - 4\pi c\Lambda'_{23}k\vec{\nabla}T}{4\pi\omega}, \quad N_{31} = \frac{i\omega}{4\pi}\zeta_{31},$$

$$N_{32} = \frac{(i\omega^2 - ic^2k^2)\zeta_{32} - 4\pi c\Lambda'_{32}k\vec{\nabla}T}{4\pi\omega}, \quad N_{33} = \frac{(i\omega^2 - ic^2k^2)\zeta_{33} - 4\pi c\Lambda'_{33}k\vec{\nabla}T}{4\pi\omega} \quad (20)$$

Taking into account (19-20) from (11) we get:

$$N_{11} - I + 2N_{11}N_{22} = 0 \quad (21)$$

$$\zeta_{11} = \zeta_{22} = \zeta$$

$$\frac{i\omega\zeta}{4\pi} - \frac{\omega^2\zeta^2}{8\pi^2} + \frac{k^2c^2\zeta^2}{8\pi^2} - \frac{i\omega'_{21}\zeta}{2\pi} - 1 \quad (22)$$

From solution (22) we obtain

$$\varpi_1 = \frac{i\pi}{\zeta} - \left(\frac{2\varpi'_{21}\zeta}{\pi} \right)^{1/2} \frac{\pi}{\zeta} + \frac{i\pi}{\zeta} \left(\frac{2\varpi'_{21}\zeta}{\pi} \right)^{1/2} \quad (23)$$

$$\varpi_2 = \frac{i\pi}{\zeta} + \left(\frac{2\varpi'_{21}\zeta}{\pi} \right)^{1/2} \frac{\pi}{\zeta} - \frac{i\pi}{\zeta} \left(\frac{2\varpi'_{21}\zeta}{\pi} \right)^{1/2}$$

From (23) it can be seen that a wave with a frequency $\varpi_0 = -\left(\frac{2|\varpi'_{21}|}{\pi\zeta} \right)^{1/2}$ is increasing, a wave with a frequency $\varpi_0 = -\left(\frac{2|\varpi'_{21}|}{\pi\zeta} \right)$ can grow if $2\|\varpi'_{21}\|\zeta < \frac{\pi}{2}$

For an arbitrary orientation of the wave vector relative to the temperature gradient, from tensor (10), we obtain

$$\begin{aligned} N_{11} &= \frac{i\varpi^2\zeta_{11} + \varpi_{11}}{4\pi\varpi}, \quad N_{12} = \frac{(i\varpi^2 - ic^2k^2)\zeta_{12} - \varpi_{11} + \varpi_{22}}{4\pi\varpi}, \quad N_{13} = \frac{(i\varpi^2 - ic^2k^2)\zeta_{13} + \varpi_{13}}{4\pi\varpi}, \\ N_{21} &= \frac{i\varpi^2\zeta_{21} + \varpi_{21}}{4\pi\varpi}, \\ N_{22} &= \frac{(i\varpi^2 - ic^2k^2)\zeta_{22} + \varpi_{22}}{4\pi\varpi}, \quad N_{23} = \frac{(i\varpi^2 - ic^2k^2)\zeta_{23} + \varpi_{23}}{4\pi\varpi}, \quad N_{31} = \frac{i\varpi^2\zeta_{31} + \varpi_{31}}{4\pi\varpi}, \\ N_{32} &= \frac{(i\varpi^2 - ic^2k^2)\zeta_{32} + \varpi_{32}}{4\pi\varpi}, \quad N_{33} = \frac{(i\varpi^2 - ic^2k^2)\zeta_{33} - \varpi_{33}}{4\pi\varpi}, \quad \varpi_{ik} = -4\pi c \Lambda'_{ik} (\vec{k} \vec{\nabla} T) \end{aligned} \quad (24)$$

Choosing a crystal

From (11), taking into account (24), we obtain the following dispersion equation for determining the frequency and growth rate of the excited waves inside an anisotropic crystal

$$\begin{aligned} \frac{i\varpi^2\zeta_{11} - \varpi_{11}}{4\pi\varpi} \left(\frac{i\varpi^2\zeta_{12} - ic^2k^2\zeta_{12} - \varpi_{11} - \varpi_{12} + 1}{4\pi\Omega} + 1 \right) = \\ \frac{i\varpi^2\zeta_{22} - ic^2k^2\zeta_{22} + \varpi_{22}}{4\pi\varpi} \left(\frac{i\varpi^2\zeta_{11} - \varpi_{11} - 1}{4\pi\varpi} \right) \end{aligned} \quad (25)$$

At $\varpi_{12} = \varpi_{11} + \varpi_{22}$ and $\zeta_{12} = \zeta_{11} + \zeta_{22}$ from (25) we get

$$\varpi^2 = \frac{1}{2} \left(c^2k^2 + i \frac{\varpi_{12}}{\zeta} \right) \quad (26)$$

Solution (26) gives

$$\varpi = \frac{ck}{2} \left(\frac{\varpi_{12}}{c^2k^2\zeta} \right)^{1/2} (1+i) \quad (27)$$

$$\text{or } \Omega = \Omega_0 + i\gamma$$

$$\varpi_0 = \left(\frac{\varpi_{12}}{4\zeta} \right)^{1/2}, \quad \gamma = \left(\frac{\varpi_{12}}{4\zeta} \right)^{1/2} \quad (28)$$

For any orientation of the wave vector with respect to the temperature gradient, the frequency and growth rate of the excited thermomagnetic are the same.

DISCUSSION OF THE RESULTS

In anisotropic conducting media of the electric type of charge carriers in an external electric field in the presence of a constant temperature gradient,

longitudinal $\vec{k} \parallel \vec{\nabla}T$ and transverse $\vec{k} \perp \vec{\nabla}T$ waves of a thermomagnetic nature are excited. The frequency and growth rate of this wave depend on the conductivity of the medium. The conductivity of a medium is easily expressed in terms of the diagonal values of the conductivity. This creates a favorable condition for experimental verification of the exciting waves. If the wave vector of the excited waves has an arbitrary direction relative to a constant temperature gradient, then the frequency and growth rate have the same values. When calculating, we choose crystals of different symmetry. Of course, the conditions for the

excitation and growth of the wave will be different if we choose different symmetries from the tensor (11).

CONCLUSION

It is proved that in anisotropic conducting media of electric type of charge carriers, different waves of a thermomagnetic nature are excited. With the longitudinal $\vec{k} \parallel \vec{\nabla}T$ and transverse $\vec{k} \perp \vec{\nabla}T$ orientation of the wave vector relative to the temperature gradient, waves of a thermomagnetic nature with different frequencies and increments are excited.

-
- [1] *E.R. Hasanov, A.V.Islamzade, H.Sh.Hasanov. Thermomagnetic Waves In Anisotropic Conductors International Journal On Technical And Physical Problems Of Engineering, March 2016, Vol.8, N1, (50-54).*
- [2] *E.R. Hasanov, I.I. Mustafayeva. Non-linear fluctuations of concentration of charge carriers and an electric field in semiconductors 13th International Conference on "Technical and Physical Problems of Electrical Engineering", 21-23 September, 2017, N38, p. (39-43).*
- [3] *E.R. Hasanov, F.F. Aliev. Nonlinear Oscillation Task for the Concentration of Field Carriers in Semiconductors with Deep Traps IOSR Journal of Applied Physics, Volume 10, Issue 1 Ver. II (Jan.-Feb. 2018), p. (36-42).*
- [4] *E.R. Hasanov, Sh.G. Khalilova, E.O. Mansurova, N.M. Tabatabaei. Unstable thermomagnetic waves in anisotropic medium of electronic type of charge carriers. International Journal on "Technical and Physical Problems of Engineering" (IJTPE) Turkey, March 2020, Issue 42, Volume 12, Number 1 Pages 49-52.*
- [5] *E.R. Hasanov, Sh.G. Khalilova, Z.A. Tagiyeva, V.M. Hajiyeva, S.S. Ahadova. Excitation of thermomagnetic and recombination waves in impurity with two types of current carriers International Journal on "Technical and Physical Problems of Engineering"(IJTPE), march 2021, Issue 46, Volume 13, N 21, pp. 57-61.*

Received: 01.02.2023

ANALYSIS OF FLUCTUATION CONDUCTIVITY IN $Y_{0.3}Cd_{0.7}Ba_2Cu_3O_{7-\delta}$

V.M. ALIYEV, G.I. ISAKOV, J.A. RAHIMOV¹, V.I. EMINOVA, S.Z. DAMIROVA,
G.A. ALIYEVA²

*Institute of Physics Ministry of Science and Education of Azerbaijan,
AZ 1143, Baku, H. Javid Ave., 131*

¹*Azerbaijan Medical University, AZ 1022, Baku, st. Bakikhanov, 23*

²*Institute of NCP Ministry of Science and Education of Azerbaijan, Baku, Azerbaijan, AZ
1025, Baku, Khojaly ave., 30
v_aliev@bk.ru*

A study was made of the influence of substitution of up to 50% of yttrium for cadmium in $YBa_2Cu_3O_{7-\delta}$ polycrystals on the mechanism of formation of excess conductivity. It has been established that such a substitution led to a significant increase in the resistivity of $Y_{0.3}Cd_{0.7}Ba_2Cu_3O_{7-\delta}$ and the value of the critical transition temperature T_c to the superconducting state decreases. The mechanism of formation of fluctuation conductivity (T) near T_c is considered within the framework of the Aslamazov-Larkin theory. The Ginzburg temperature, the critical temperature in the mean field approximation, and the 3D-2D crossover temperature were determined. It is shown that the doping of $YBa_2Cu_3O_{7-\delta}$ with cadmium leads to the coherence length along the c axis by a factor of 1.96. An analysis of the excess conductivity of the $Y_{0.3}Cd_{0.7}Ba_2Cu_3O_{7-\delta}$ sample within the framework of the local pair model made it possible to determine the temperature dependences of the pseudogap and its maximum value.

Keywords: superconductivity, pseudogap, excess conductivity, coherence length, composition.

PACS: 74.25.Fy, 74.20.Mn, 74.72.+h, 74.25.+g, 74.25.Jb

In recent years, the group of works [1–5] devoted to the analysis of pseudogap effects in HTSC compounds has appeared. Pseudogap (PG) is a unique phenomenon characteristic of HTSC with an active CuO_2 plane (cuprates) in the doping region less than optimal. It manifests itself in studies of the phenomena of tunneling, photoemission, heat capacity [2, 4] and other properties of HTSC. It is assumed that at a certain temperature $T^* \gg T_c$ (T_c is the critical temperature of the superconducting transition) the density of states on the Fermi surface is redistributed: on a part of this surface the density of states decreases. Below the temperature T^* , the compound is in a pseudogap state. In these works, possible conduction mechanisms in the modes of the normal, superconducting, and pseudogap states in HTSC are also discussed.

Recently, the work [6], devoted to the study of the pseudogap state in $Pb_{0.55}Bi_{1.5}Sr_{1.6}La_{0.4}CuO_{6+\delta}$ (Pb - $Bi2201$) appeared. A series of Pb - $Bi2201$ single crystals was obtained, on which a wide range of investigations were conducted to identify the pseudogap state. The results of studies on three different experimental methods indicate that the appearance of a pseudogap at $T \cong 132$ K should be perceived only as a phase transition. Thus, the authors confirmed the assumption that at the temperature decreasing, the HESC material must undergo two phase transitions: first the appearance of a pseudogap, and then a transition to the superconducting state.

However, as noted by A. Abrikosov [7], the pseudogap state cannot really be considered as some kind of new phase state of matter, since the PG is not separated from the normal state by a phase transition. So the question of a possible phase transition at $T = T^*$ also remains open. At the same time, it can be said that a crossover occurs at $T = T^*$ [1]. Below this

temperature, due to reasons not yet established to date, the density of quasiparticle states at the Fermi level begins to decrease. Actually for this reason, this phenomenon is called "pseudogap". For the first time, this result was obtained in experiments on the study of NMR in a weakly doped $Y123$ system, in which an anomalous decrease of the Knight shift [2] during cooling, which is directly related to the density of states at the Fermi level in the Landau theory, was observed. Note that earlier in [8] we analyzed the fluctuation conductivity $Y_{1-x}Cd_xBa_2Cu_3O_{7-\delta}$ ($x=0 \div 0.4$).

Thus, the aim of this work is to study the normal state of $YBa_2Cu_3O_{7-\delta}$ (sampb. Y1) and $Y_{0.3}Cd_{0.7}Ba_2Cu_3O_{7-\delta}$ (sampb. Y2) in the temperature range $T^* > T > T_c$, to determine their physical characteristics, as well as to study the possibility of the occurrence of the PG states in these compounds. The analysis was carried out on the basis of the study of excess conductivity above T_c in the framework of the local pair (LP) model [3,4] taking into account the Aslamazov – Larkin fluctuation theory [8] near T_c .

EXPERIMENTAL RESULTS AND THEIR PROCESSING

The method for obtaining $Y_{0.3}Cd_{0.7}Ba_2Cu_3O_{7-\delta}$ is described in [9].

The temperature dependences of the specific resistivity ρ of the samples \square Y1 and Y2 are showed in Fig.1. The critical temperatures of the SC transition T_c were determined from the maximum obtained by differentiating the curve $\rho(T)$. Critical temperature of investigated samples is $T_{c1} = 92.63$ K (Y1) and $T_{c2} = 89.23$ (Y2), respectively (Fig.1). In this case, the resistivity of the sample $Y_{0.3}Cd_{0.7}Ba_2Cu_3O_{7-\delta}$ $Y_{0.3}Cd_{0.7}Ba_2Cu_3O_{7-\delta}$ in the normal phase at 300 K increases almost 15 times compared to $YBa_2Cu_3O_{7-\delta}$.

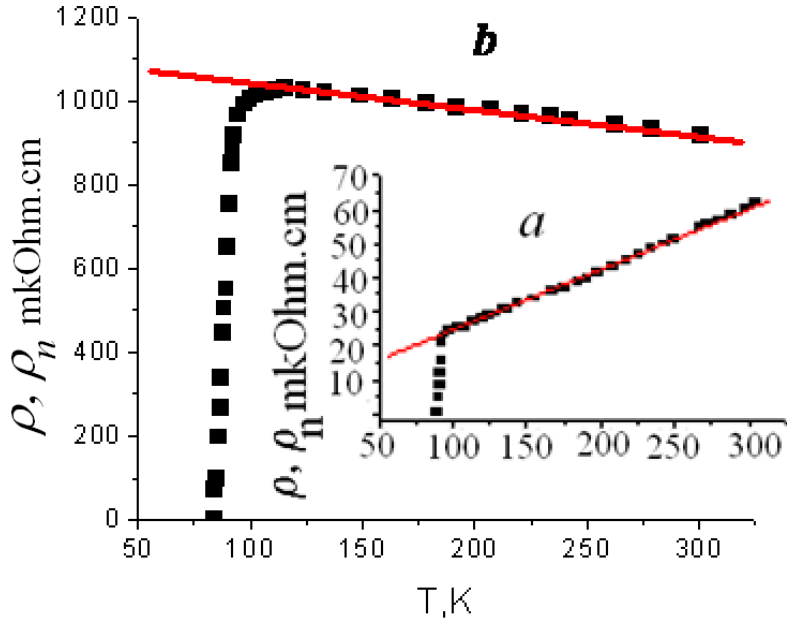


Fig. 1. Temperature dependences of the resistivity ρ of the samples: a- $YBa_2Cu_3O_{7-\delta}$ (Y1) [8] and b- $Y_{0.3}Cd_{0.7}Ba_2Cu_3O_{7-\delta}$ (Y2). Direct represent dependences $\rho_n(T)$ extrapolated to the region of low temperatures.

FLUCTUATION CONDUCTIVITY

The linear course of the temperature dependence of the specific resistance of samples Y1 and Y2 in the normal phase is well extrapolated by the expressions $\rho_n(T) = (D + \kappa T + BT^2)$ and $\rho_n(T) = (\rho_0 + \kappa T + BT^2)$ (here D, B and k are some constants). This linear relationship, extrapolated to the low temperature range, was used to determine excess conductivity $\Delta\sigma(T)$ according to:

$$\Delta\sigma(T) = \rho^{-1}(T) - \rho_n^{-1}(T). \quad (1)$$

The analysis of the behavior of excess conductivities was carried out in the framework of the local pair model [4, 11].

Assuming the possibility of the formation of local pairs [3,4] in the Y2 sample at a temperature below $T^* = 116,39K$ (Y2), the experimental results near T_c are obtained and analyzed taking into account the appearance of fluctuation Cooper pairs (FCP) above T_c in the framework of the Aslamazov-Larkin theory (AL) [9].

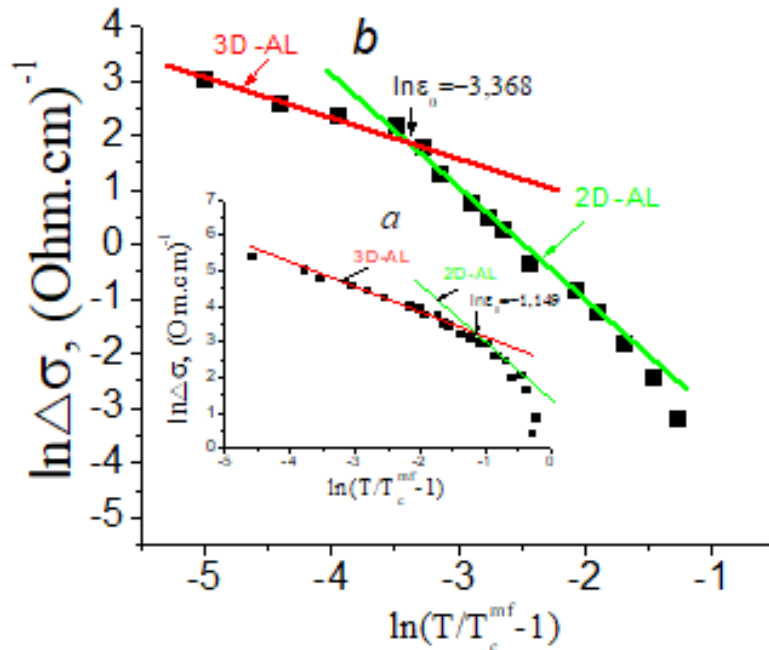


Fig.2. Dependences of the logarithm of excess conductivity on $\ln(T/T_c^{mf}-1)$ of samples Y1[8] and Y2. Solid lines – calculation within the framework of the Aslamazov-Larkin theory.

The Fig. 2 shows dependence of the logarithm of the excess conductivity of the samples Y1 (1) and Y2 (2) on the logarithm of the reduced temperature $\varepsilon = (T / T_c - 1)$. According to the theory of AL, as well as Hikami – Larkin (HL) developed for HTSC [10], in the region of $T > T_c$ (but near T_c), the fluctuation coupling of charge carriers occurs, leading to the appearance of fluctuation conductivity (FC). In this region, the temperature dependence of excess conductivity on temperature is described by the expressions:

$$\Delta\sigma_{\text{AJ3D}} = C_{3D} \{e^2/[32\hbar\xi_c(0)]\}\varepsilon^{-1/2}, \quad (2)$$

$$\Delta\sigma_{\text{AJ2D}} = C_{2D} \{e^2/[16\hbar d]\}\varepsilon^{-1}, \quad (3)$$

respectively for three-dimensional (3D) and two-dimensional (2D) region. The scaling coefficients C are used to combine the theory with experiment [4].

Thus, by the angle of inclination α of dependences $\ln(\Delta\sigma)$ as a function of $\varepsilon = \ln(T / T_c - 1)$ (see Fig. 3), we can distinguish 2D ($\text{tg}\alpha = -1$) and 3D ($\text{tg}\alpha = -1/2$) regions of phase transition. It can also

determine the crossover temperature T_0 (the transition temperature from $\Delta\sigma_{2D}$ to σ_{3D}) and the tangents of the slopes of the dependences $\Delta\sigma(T)$ corresponding to the exponents ε in equations (2) and (3). The corresponding values of the parameters 2D and 3D regions determined from the experiment for sample Y1 are 2D ($\text{tg}\alpha = -1.04$) and 3D ($\text{tg}\alpha = -0.44$) and for Y2 2D ($\text{tg}\alpha = -1.1$) and 3D ($\text{tg}\alpha = -0.49$).

On basis of value the temperature of the crossover T_0 , which corresponds to $\ln\varepsilon_0$, according to Fig. 2, it can determine the coherence length of local pairs along the c axis [12,13]:

$$\xi_c(0) = d\sqrt{\varepsilon_0}, \quad (4)$$

here $d \approx 11.7\text{\AA}$ is the distance between the inner conducting planes in Y-Ba-Cu-O [13]. The values of $\xi_c(0) = 1,1\text{\AA}$ ($\ln\varepsilon_0 \approx -1.149$) for Y1 and $\xi_c(0) = 2,16$ ($\ln\varepsilon_0 \approx -3.368$) for Y2 was obtained, accordingly.

The parameters of the $Y_{0,3}Cd_{0,7}Ba_2Cu_3O_{7-\delta}$ and $YBa_2Cu_3O_{7-\delta}$ samples obtained from fluctuation conductivity analysis are given in Table 1.

Table 1.

Parameters of $Y_{0,3}Cd_{0,7}Ba_2Cu_3O_{7-\delta}$ and $YBa_2Cu_3O_{7-\delta}$ samples obtained from fluctuation conductivity analysis

YBCO (Cd)	$\rho(300K)$, мкОм·см	$\rho(100K)$, мкОм·см	T_c , K	T_c^{mf} , K	T_G , K	T_0 , K	$\xi_c(0)$, Å	Лит.
Y1 (x=0)	60	24	90,2	91,99	92,1	92,8	1,1	[8]
Y2(x=0,7)	923	1051	84,6	87,1	88	89,6	2,16	-

ANALYSIS OF THE MAGNITUDE AND TEMPERATURE DEPENDENCE OF THE PSEUDOGAP

As noted above, in the cuprates at $T < T^*$, the density of electron states of quasiparticles on the Fermi level decreases [14] (the cause of this phenomenon is not yet fully elucidated), which creates conditions for the formation of a pseudogap in the excitation spectrum and it leads ultimately to the formation of an excess conductivity. The magnitude and temperature dependence of the pseudogap in the investigated samples was analyzed using the local pair model, taking into account the transition from Bose-Einstein condensation (SCB) to the BCS mode predicted by the theory [10] for HTSC when the temperature decreases in the interval $T^* < T < T_c$. Note that excess conductivity exists precisely in this

temperature range, where fermions supposedly form pairs - the so-called strongly coupled bosons (PRS). The pseudogap is characterized by a certain value of the binding energy $\varepsilon_b \sim 1/\xi^2(T)$, causing the creation of such pairs [10,13], which decreases with temperature, because the coherence length of the Cooper pairs $\xi(T) = \xi(0)(T/T_c - 1)^{-1/2}$, on the contrary, increases with decreasing temperatures. Therefore, according to the LP model, the SCB are transformed into the FCP when the temperature approaches T_c (BEC-BCS transition), which becomes possible due to the extremely small coherence length $\xi(T)$ in cuprates.

From our studies, we can estimate the magnitude and temperature dependence of PG, based on the temperature dependence of excess conductivity in the entire temperature range from T^* to T_c according to [3,13]:

$$\Delta\sigma(\varepsilon) = \left\{ \frac{A(1 - T/T^*)[\exp(-\Delta^*/T)]e^2}{16\hbar\xi_c(0)\sqrt{2\varepsilon_0^* \cdot sh(2\varepsilon/\varepsilon_0^*)}} \right\} \quad (5)$$

where the $(1 - T/T^*)$ determines the number of pairs formed at $T \leq T^*$; and the $\exp(-\Delta^*/T)$ determines the number of pairs destroyed by thermal fluctuations below the BEC-BCS transition temperature. The coefficient A has the same meaning as the coefficients C_{3D} and C_{2D} in (2) and (3).

The solution of equation (5) gives the value of Δ^* :

$$\Delta^*(T) = T \cdot \ln \left\{ \frac{A(1-T/T^*)e^2}{\Delta\sigma(T)16\hbar\xi_c(0)\sqrt{2\varepsilon_0^*} \cdot sh(2\varepsilon/\varepsilon_0^*)} \right\} \quad (6)$$

where $\Delta\sigma(T)$ is the experimentally determined excess conductivity.

On fig. Figure 3 shows the dependences of the logarithm of the excess conductivity of the sample Y2 on the reciprocal temperature. The choice of such coordinates is due to the strong sensitivity of the linear section $\ln\Delta\sigma(1/T)$ to the value $\Delta^*(T_c)$ in equation (5),

which allows you to estimate this parameter with high accuracy (this is necessary to find the coefficient A) [3,14,16]. Dependences $\ln\Delta\sigma(1/T)$ were calculated according to the method tested in [12]. As can be seen from fig. 3, the $\ln\Delta\sigma(1/T)$ values calculated for sample Y2 with parameters:

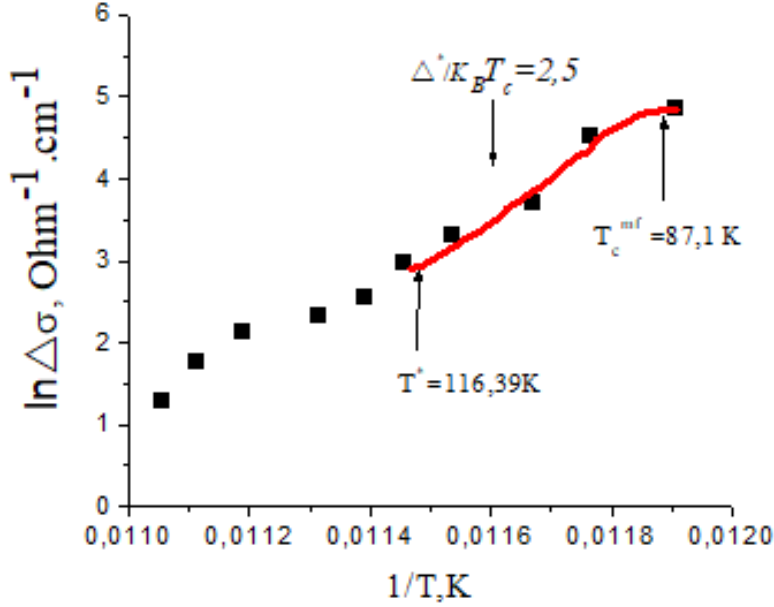


Fig.3. Dependences of the logarithm of excess conductivity on the reciprocal temperature polycrystal $Y_{0.3}Cd_{0.7}Ba_2Cu_3O_{7.8}$ solid lines – approximation eq. 6 with parameters given in the text.

$A=1,847 \pm 0,1$, $T^*=116,39K$, $\zeta_c(0)=2,16 \text{ \AA}$ are in good agreement with the experimental data.

The temperature dependence and the value of the pseudogap parameter $\Delta^*(T)$ (Fig.4) were calculated based on equation (6) with the parameters given above. As

Noted in [3,4,14], the value of the coefficient A is selected from the condition of the coincidence of the temperature dependence $\Delta\sigma$ (eq.(5), assuming $\Delta^* = \Delta^*(T)$) with experimental data in the region of 3D fluctuations near T_c . According to [14,16], the optimal approximation for an HTSC material is achieved at the values $2\Delta^*(T_c)/K_B T_c = 5$. As a result, from the LP analysis for Y2 $\Delta^*(T_c^{mf})= 89.23 \cdot 2.5 = 223.075K$, which is consistent with the experimental data (Fig.4).

From the presented data in Fig.4, it is also seen that as T decreases, the pseudogap value first increases, then, after passing through a maximum, decreases.

This decrease is due to the transformation of the SCB in the PCF as a result of the BEC-BCS transition, which accompanied by an increase in excess conductivity at $T \rightarrow T_c$. Such a behavior of Δ^* with decreasing temperature was first found on YBCO films [3.14] with different oxygen contents, which seems to be typical of cuprate HTSC [14].

The pseudogap parameters of the $Y_{0.3}Cd_{0.7}Ba_2Cu_3O_{7.8}$ sample obtained from fluctuation conductivity analysis are given in Table 2.

Parameter of pseudogap analysis of HTSC material $Y_{0.3}Cd_{0.7}Ba_2Cu_3O_{7.8}$

Table 2.

YBCO	T^* , K	A^*	T_m , K	D^* , K	$\Delta^*(T_m)$, K	$\Delta^*(T_G)$, K
Y2(x=0.5)	142,6	16,6	122,6	2,5	660	385

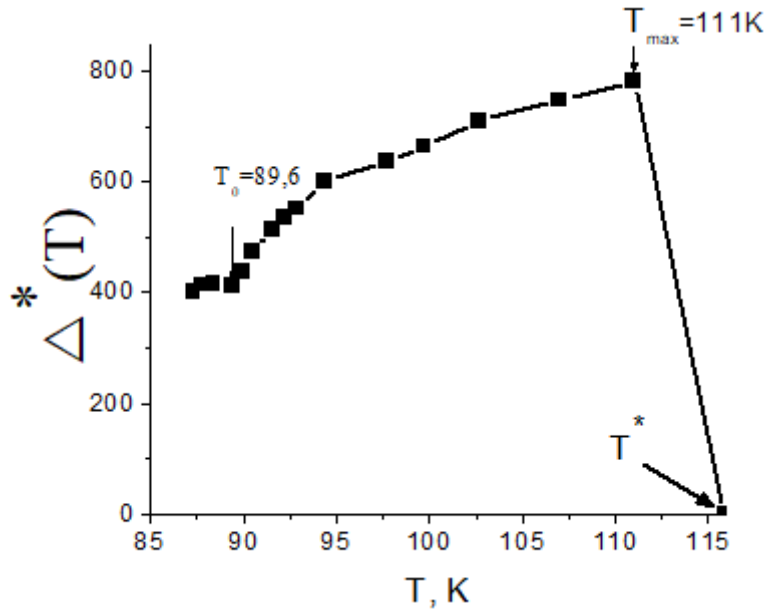


Fig.4. Temperature dependences of the calculated value of the sample pseudogap Y2 with parameters given in the text. The arrows show the maximum values of the pseudogap.

CONCLUSION

Thus, we can conclude that, in the $Y_{0.3}Cd_{0.7}Ba_2Cu_3O_{7-\delta}$ studied by us, the formation of local pairs of charge carriers at $T \gg T_c$ is possible, which creates conditions for the formation of a pseudogap [10-12] with the subsequent establishment

of the phase coherence of fluctuation Cooper steam at $T > T_c$ [14,17].

The study showed that near T_c the fluctuation conductivity is well described in terms of the Aslamazov-Larkin fluctuation theory: 3D-AL. Above the 3D-2D crossover temperature, the 2D-AL theory is applicable.

- | | |
|--|--|
| <p>[1] E.B. Amitin, K.R. Zhdanov, A.G. Blinov et al. FNT, 31, 4, (2005), 323-326.</p> <p>[2] M.V. Sadovsky. UFN, 171, (2001), 539-564.</p> <p>[3] M.R. Trunin. UFN, 175, 10, (2005), 1017-1037.</p> <p>[4] A.L. Soloviev, V.M. Dmitriev. FNT, 32, 6, (2006), 753-760.</p> <p>[5] A.L. Solovjov, M.A. Tkachenko, R.V. Vovk, A. Chroneos. Physica C, 501, (2014), 24-31.</p> <p>[6] He Rui-Hua., M. Hashimoto, H. Karapetyan et al. Science, 331, (2011), 1579-1583</p> <p>[7] A.A. Abrikosov. UFN, 174, 11, (2004), 1233-1239.</p> <p>[8] L.G. Aslamazov and A.L. Larkin. Physics Letters, 26A, 6, (1968), 238-239.</p> <p>[9] S.A. Aliev, S.S. Ragimov, V.M. Aliev. Fizika, 2004, 10, 4, (2004) 42-43.</p> | <p>[10] V.M. Loktev, V.M. Turkowski. Fizika Nizkikh Temperatur, 30, 3, (2004), 247-260.</p> <p>[11] S. Hikami, A.I. Larkin. Modern Phys. Lett., v. B2, (1988) 693-697.</p> <p>[12] B. Oh, K. Char, A.D. Kent, et al. Phys. Rev. B37, 13, (1988) 7861-7864.</p> <p>[13] A.L. Soloviev, V.M. Dmitriev. FNT, 35, 3, (2009) 227-264.</p> <p>[14] A.A. Kordyuk. FNT, 41, 5, (2015), 417-444.</p> <p>[15] D.D. Prokofiev, M.P. Volkov, Yu.A. Boikov. FTT, 45, 7, (2003) 1168-1176</p> <p>[16] V.V. Florentiev, A.V. Inyushkin, A.N. Taldenkov et al. Superconductivity: Physics, Chemistry, Technology, 1990, 3, 10, part 2, (1990) 2302-2319.</p> <p>[17] R. Peters and J. Bauer. Phys. Rev. B 92, 014511 – Published 22 July 2015.</p> |
|--|--|

Received: 23.01.2023

INVESTIGATION OF INFLUENCE OF BARRIER DISCHARGE PLASMA ON BARIUM TITANATE PARTICLE DOPED POLYETHYLENE BY DSC METHOD

T.D. IBRAGIMOV, I.S. RAMAZANOVA, U.V. YUSIFOVA, F.F. YAHYAYEV

Institute of Physics, Ministry of Science and Education of Azerbaijan

131, H. Javid ave., Baku, AZ 1143

tdibragimov@mail.ru

Composite films based on high-density polyethylene and barium titanate particles before and after treatment with a dielectric barrier gas discharge were studied by differential scanning calorimetry. The values of critical temperatures, changes in entropy, enthalpy, and degree of crystallinity before and after the action of the gas discharge are found. It is shown that the critical temperature after the action of a gas discharge decreases during heating, and increases during cooling, except for the concentration of barium titanate particles of 5 vol. %. In addition, the change in entropy and enthalpy during discharge processing increases as well as the degree of crystallinity. As the filler concentration increases, the change in enthalpy, entropy, and the degree of crystallinity decrease.

Keywords: barium titanate, high density polyethylene, dielectric barrier discharge plasma; enthalpy, entropy, crystallinity.

PACS: 77.84.Lf, 77.65.-j

1. INTRODUCTION

Surface modification by electric discharge plasma is one of the most interesting applications compared with other techniques which require vacuum conditions. Under electric discharge plasma treatment, the polymeric surface undergoes a functionalization process which includes the formation of various polar groups containing oxygen [1-2]. Authors of the work [3] used the corona discharge plasma technique to modify the properties of low density polyethylene film. The results obtained show good treatment homogeneity and an improvement of adhesion properties by the functionalization and etching of the film surface. In the work [4], low pressure glow discharge O₂ plasma has been used in order to improve adhesion properties and make it useful for technical applications of low-density polyethylene (LDPE) film using differential scanning calorimetry. The results show that low pressure O₂ plasma improves wettability in LDPE films and no significant changes can be observed at longer exposure times. The fluorine-containing polymer composite filled with piezo-ceramics were prepared by a hot pressing method in the work [5]. According to the obtained experimental results, the stability of the electret charge of a composite based on F42 + PZT-5A is better than a composite based on F3 + PZT-8. The polyethylene porous films were treated by dielectric surface barrier discharge plasma in the work [6]. The significant increase of the surface energy and its polar component of polyethylene porous films were observed. The LDPE films modified by barrier discharge plasma were investigated to improve surface properties and adhesion of LDPE in the work [7]. It was shown that the topography of modified LDPE was significantly changed and the surface of modified polymer exhibited higher roughness in comparison with unmodified polymer. In the paper [8] plasma processing of polymer films and particles is examined by coating and noncoating plasmas. The authors

believe that the difference by a factor of three in the etching rate between films in ammonia plasma is the consequence of their quasi-crystalline arrangement, compared to the amorphous PE films. In the paper [9], modification of the surface properties of PE films is studied using air dielectric barrier discharge plasma at atmospheric pressure. It is shown that air plasma can dramatically improve the wettability of PE surfaces. High-density polymer composites with semiconductor or dielectric fillers were prepared by the hot pressing method [10]. The results of the study indicate that, with increasing filler volume fraction, the thermal conductivity of the samples also increased.

Two possible mechanisms have been proposed in the article [11]: an increase in surface energy, and the anchor effects imparted by plasma etching. Independently from these mechanisms, reactions between free radicals, generated by plasma irradiation and adhesives are also likely to affect the adhesive properties of polymer materials. In the work [12], an atmospheric pressure glow-like dielectric barrier discharge in argon with small admixtures of hexamethyldisiloxane is employed for the deposition of thin polydimethylsiloxane films. This paper shows that the deposition rate and the chemical composition of the deposited films are strongly affected at which plasma-polymerization is performed. Two special groups of plasma polymers that have received increased attention are treated in detail in review [13].

A technology for generating craze-formation centers in polymers under the action of the electric discharge plasma and consider questions associated with a method for varying the geometrical sizes of crazes in the work [14]. The paper [15] presents a brief description of the plasma chemical method for synthesizing semiconducting polymers.

Low-pressure plasma co-polymerisation of binary gas mixtures of ethylene and ammonia was investigated in the work [16] in order to deposit N-rich plasma polymer coatings for biomedical applications. Authors of the work [17] used an atmospheric pressure apparatus to deposit novel

families plasma polymers using mixtures of three different hydrocarbon precursors in nitrogen at varying respective gas flow ratios. The crystallization of “polymer–ferroelectric/piezoelectric ceramic” composites under the action of an electric discharge plasma and temperature is investigated in the work [18]. It is shown that this process results in strong oxidation of polymer chains.

The review article [19] presents various methods of plasma treatment of polymers. In particular, the dielectric barrier discharge method is described in detail. Plasma treatment serves mainly to modify the surface of polymers to increase adhesion.

The work is devoted to studying the effect of a gas discharge on high density polyethylene doped with particles of barium titanate by differential scanning calorimetric method.

2. MATERIALS AND METHODS

We used high density polyethylene (HDPE) as a matrix. Melting and softening points of polymer are 130-135°C and 80-90°C, correspondingly. The barium titanate particles with sizes of 600 nm (US, Research Nanomaterials, In.) were added into the fine powder of polyethylenewith different concentrations (5 vol. %, 10 vol. %, 20 vol.% and 30 vol.%). Then obtained mixture was shaken in a vortex mixer for 1 hour at room temperature, followed by sonication with dispergator Ultrasonic Cleaner NATO CD-4800 (China) for 4 hours. Disc-shaped samples of composites were obtained by hot pressing at temperature of 165°C and pressure of 15 MPa. Pressing time after reaching the selected temperature is 15-20 minutes. The diameter and thickness of the obtained films were 4 cm and 100 µm, respectively.

The electric discharges were used as non-thermal non-equilibrium plasma, which is termed surface micro-discharges (SMD). The generation of SMDs at ambient pressure is obtained from the dielectric-barrier discharge (DBD) technology which is related to the corona discharge family. The DBD treatment carried out on the set up described earlier in the work [18]. In this case, the voltage of electric charge in the cells equals 8 kV.

The differential scanning calorimeter DSC 204 F1 (firm Netzsch, Germany) with the CC200 F1 cooling system regulating the flow of liquid nitrogen was used to determine thermophysical parameters. Argon was served to purge and to protect the cell at the pressure of 50 kPa. The DSC204F1 and Proteus Analysis software programmes were used to process the results. The rate of temperature change was 10 K/min in the temperature range between 20°C and 150°C. Exposure time was 30 min.

The critical temperature T_{cr} , at which the composite changes from one state to another, is determined by the local maximum of the heat flow while the change in enthalpy ΔH is determined by the expression

$$\Delta H = k \cdot \Delta A, \quad (1)$$

where the k-coefficient characteristic of this device, A - the area under the corresponding peak. The entropy change ΔS during transition is defined as

$$\Delta S = \frac{\Delta H}{T_{cr}}, \quad (2)$$

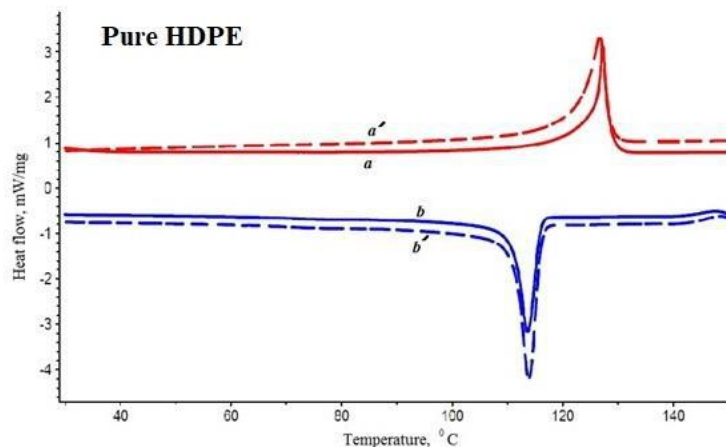
The degree of crystallinity K is found according to the expression:

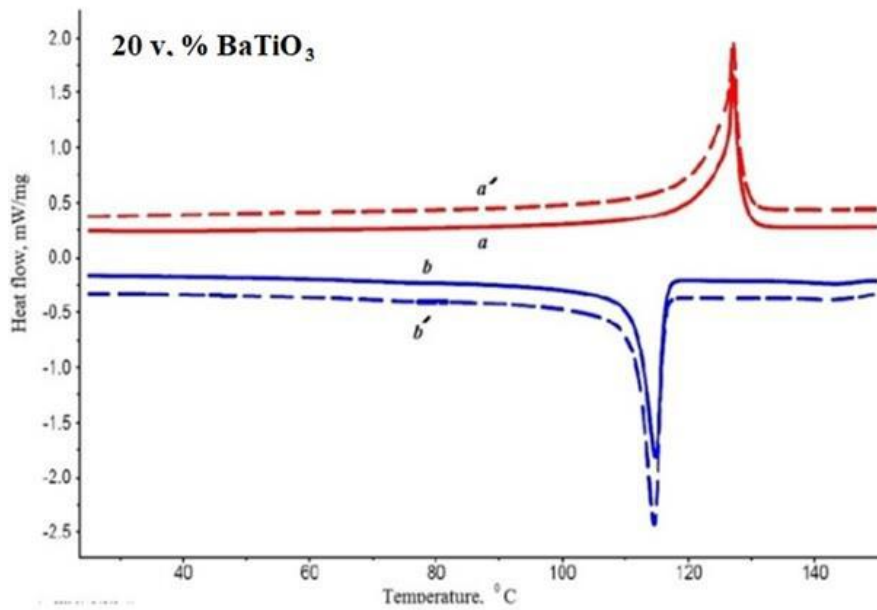
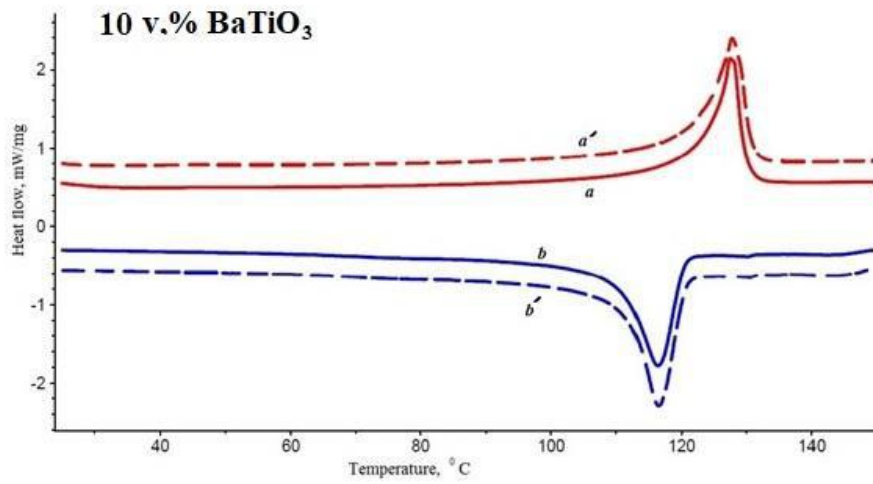
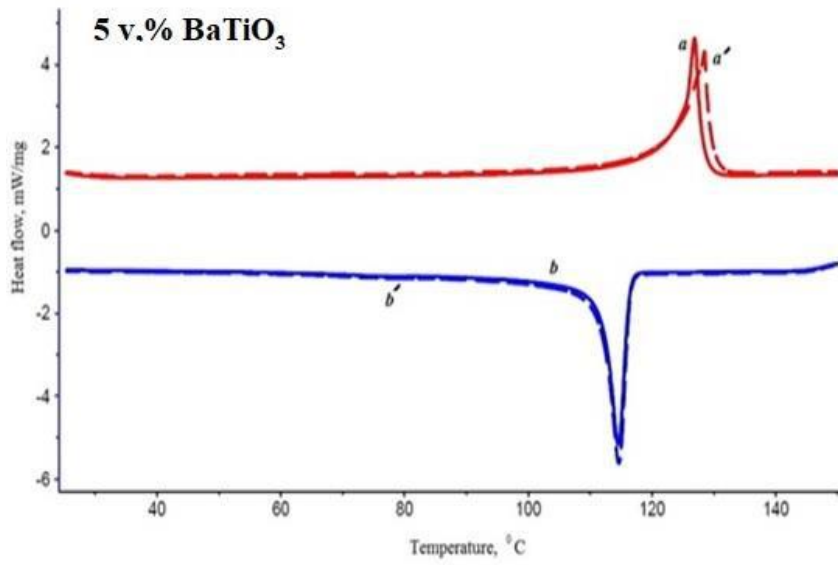
$$K = \frac{|\Delta H_h + \Delta H_c|}{\Delta H(100\% \text{ cryst})} 100\%, \quad (3)$$

where ΔH_h and ΔH_c are changes of enthalpy at heating and cooling processes, correspondingly; $\Delta H(100\% \text{ cryst})$ is the change of enthalpy at 100% crystallites of matrix. For high-density polyethylene, the enthalpy change at 100% crystallization is taken to be equal to 293 J/g.

3. RESULTS AND DISCUSSION

Figure 1 shows DSC curves for both pure polymer and composites with different filler concentrations before and after discharge treatment.





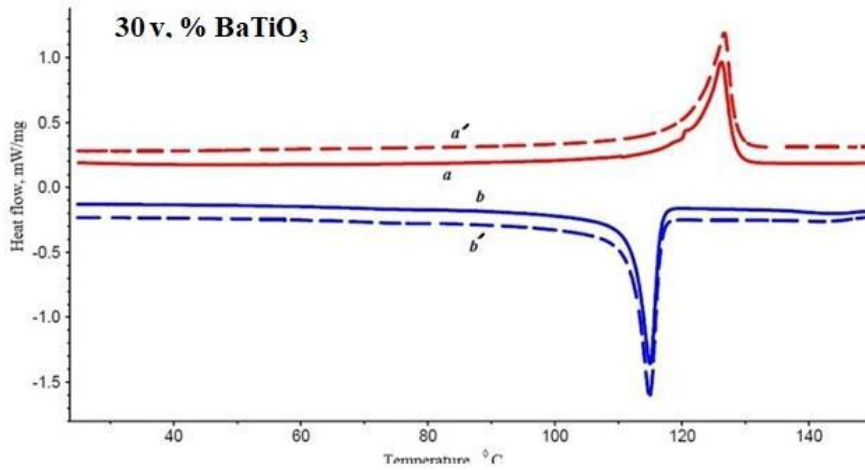


Fig. 1. Heat flow versus temperature for composites at various filler concentrations: (a) untreated sample at heating regime, (a') plasma treated sample at heating regime, (b) untreated sample at cooling regime, (b') plasma treated sample at cooling regime.

As can be seen, the peaks of the curves corresponding to cooling regime, shifts to low temperatures. This indicates that the transition to the solid state of the composite occurs at lower temperatures. To more clearly determine the change

for different filler concentrations, we plot the dependence of the critical temperature T_{cr} on the filler concentration and scanning regime. The corresponding graph is shown in Figure 2.

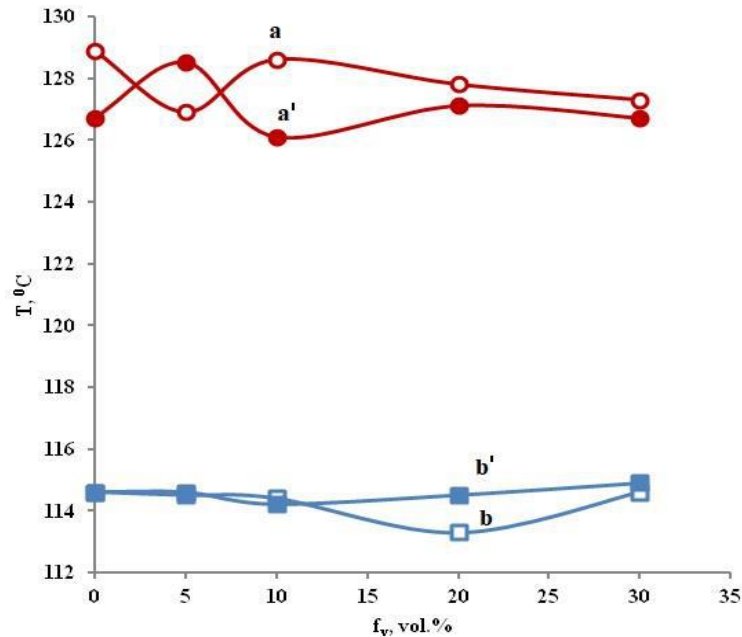


Fig. 2. Dependence of critical temperature on filler concentration: (a) untreated sample at heating regime, (a') plasma-treated sample at heating regime, (b) untreated sample at cooling regime, (b') plasma-treated sample at cooling regime.

As can be seen, the critical transition temperature of pure polyethylene and composites decreases after gas discharge treatment at the heating regime, except for the composite with concentration of 5 vol. %. A similar result, namely, an increase in the critical temperature at low filler concentrations, was obtained in the processing of low density polyethylene film by low pressure O_2 plasma treatment [4]. Probably, the increase in the critical temperature at concentration of 5 vol. % is associated with a more uniform distribution of particles in the polymer matrix. At

cooling regime, a higher concentration of filler induces the transition to solid state at higher temperatures.

Figure 3 shows the dependence of the change in enthalpy on the concentration of the filler during melting and solidification of the samples.

As can be seen, the change in enthalpy during melting and solidification decreases with increasing filler concentration. At the same time, it is sharper at low concentrations while it is slower at high concentrations.

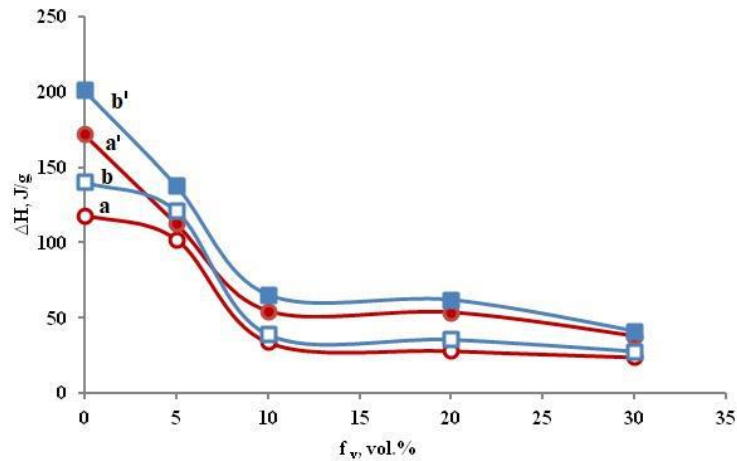


Fig. 3. The dependence of the change in enthalpy on the volume concentration of the filler during melting and solidification of the samples: (a) untreated sample at heating regime, (a') plasma-treated sample at heating regime, (b) untreated sample at cooling regime, (b') plasma-treated sample at cooling regime.

The values of the enthalpy change during the solidification process at the same filler concentrations are less than during the melting process. In addition, gas discharge treatment of the samples increases the enthalpy change.

It is known that the enthalpy of fusion (melting) of a substance is the energy that is absorbed as heat from the body when it changes from solid state to liquid state (an endothermic process) and it occurs without raising the temperature for crystalline substances. It serves to disorganize the intermolecular bonds that hold molecules together. During curing, the reverse process (exothermic) occurs in which heat is removed from the substance. In this case, intermolecular bonds are restored, and the temperature does not change. For crystalline substances, the change in enthalpy during melting and solidification has the same value. The degree of crystallinity of polymers is small, so the above regularities do not apply to them. Enthalpy is an extensive quantity, that is, for a composite system; it is equal to the sum of the enthalpies of its independent parts. Likewise, the enthalpy change of the composite is also the sum of

the matrix and filler changes. The total change in the enthalpy of barium titanate particles is small, associated with a change in the symmetry group near the same temperature. But the volume fraction of the matrix, which has a sharp change in enthalpy, decreases. Therefore, the overall enthalpy change of the composite is reduced. These conclusions are in good agreement with the experimental curves of the change in enthalpy as a function of concentration.

The used technique of the barrier discharge plasma modifies the composite not only on the surface, but also in the bulk. This type of discharge is accompanied by the formation of accelerated electrons and ions, recombination radiation, active gas products and the appearance of surface electron-ion effects. The process occurs as a consequence of some breaks on the polymer chain; this situation allows the occurrence of some phenomena such as cross-linking, free radical formation, etc., with dramatic effects on the final performance of polymeric materials. The surface of composites could be oxidized when it is exposed to oxygen environment.

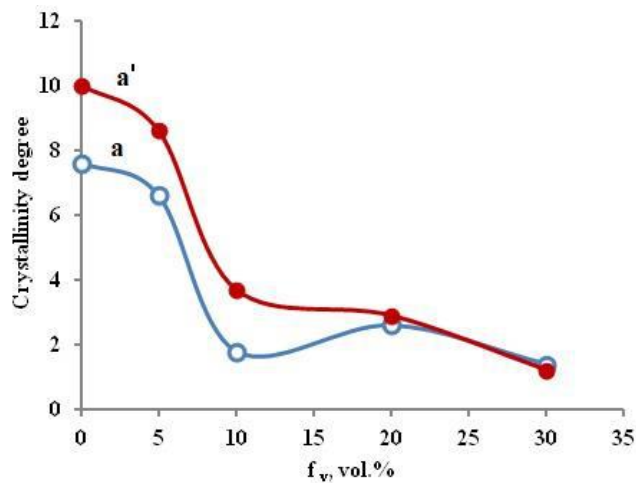


Fig. 4. Dependence of the degree of crystallinity on the volume concentration of the filler before (a) and after (a') action of the gas discharge.

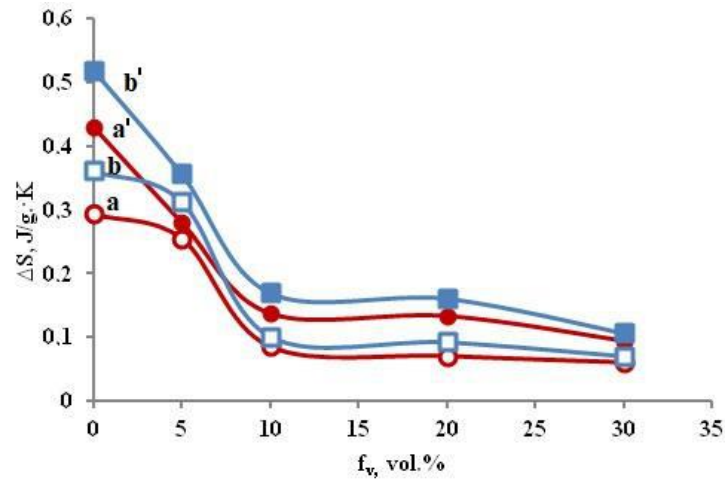


Fig. 5. The dependence of the change in entropy on the volume concentration of the filler during melting and solidification of the samples: (a) untreated sample at heating regime, (a') plasma-treated sample at heating regime, (b) untreated sample at cooling regime, (b') plasma-treated sample at cooling regime.

According to [4, 18, 19], additional oxidized species appear and oxygen atomic concentration increases. In particular, ketone $[-(C=O)-]$ and acetal $[-(O-C-O)-]$ carbons are formed while the latter represents carboxyl $[-(C-O)-O-]$ carbon. The formation of new connections contributes to the increase in the crystallinity of the composite. This corresponds to the experimental curves of crystallinity depending on the concentration (Fig. 4). At the same time, the decrease in the degree of crystallinity before and after processing is associated with a decrease in the volume fraction of polyethylene with an increase in the volume concentration of the filler.

Figure 5 shows the dependences of the enthalpy change during the transition from one aggregate state to another before and after the action of the gas discharge.

The entropy of melting and solidification is a measure of the disorder of the substance accompanying the melting or solidification, not only in the sense of changing the arrangement of atoms and their configuration, but also in the sense of changing the nature of the chemical bonds. The greater importance of the entropy of solidification compared to the entropy of melting is explained by the more ordered state of the composite in the solid phase during cooling. This is also consistent with the lower temperature transition. As it was said above, the total

change in enthalpy, similar to the entropy of the filler, is small. But the volume fraction of the matrix, which has a sharp change in entropy, decreases with an increase in the concentration of the filler. Therefore, the overall change in entropy of the composite also decreases. Since the degree of crystallinity increases after exposure to a gas discharge, the degree of ordering or disordering increases accordingly, that is, the enthalpy of solidification and melting.

4. CONCLUSIONS

It is shown that the critical temperature after the action of a gas discharge decreases during the heating process and increases during the cooling one, except for the volume concentration of barium titanate particles of 5 vol. % which is associated with a more uniform distribution of particles in the polymer matrix. With an increase in the concentration of the filler, the volume fraction of the matrix decreases leading to a decrease in entropy and entropy, and degree of crystallinity. In addition, the change in entropy and enthalpy during discharge processing increases as well as the degree of crystallinity owing to the increase of oxygen atomic concentration and formation of novel bonds.

- [1] J.M. Grace and L.J. Gerenser. Plasma treatment of polymers, *J. Dispersion Sci. Technol.* 24 (2003) 305-341.
- [2] S. Guimond and M.R. Wertheimer. Surface degradation and hydrophobic recovery of polyolefins treated by air corona and nitrogen atmospheric pressure glow discharge, *J. Appl. Polym. Sci.* 94 (3) (2004) 1291-1303.
- [3] M. Pascual, R. Sanchis, L. Sanchez, D. Garcia, and R. Balart. Surface modification of low density polyethylene (LDPE) film using corona discharge plasma for technological applications, *Journal of Adhesion Science and Technology* 22 (2008) 1425-1442.
- [4] M.R. Sanchis, V. Blanes, M. Blanes, D. Garcia, R. Balart. Surface modification of low density polyethylene (LDPE) film by low pressure O_2 plasma treatment, *European Polymer Journal* 42 (7) (2006), 1558-1568.
- [5] L. Parali. The electret effects of crystallized polymer-ferroelectric composite under

- electric discharge plasma, *Journal of Electrostatics*, 76 (2015) 89-94.
- [6] *I. Novak, G.K. Elyashevich, I. Chodak, A.S. Olifirenko, B.M. Steviar, M. Spirkova, N. Saprykina, E. Vlasova, A. Kleinova.* Polymer matrix of polyethylene porous films functionalized by electrical discharge plasma, *European Polymer Journal* 44 (2008) 2702–2707.
- [7] *I. Novak, M. Steviar, A. Popelka, I. Chodak, J. Mosnacek, M. Spirkova, I. Janigova, A. Kleinova, J. Sedliacik, M. Slouf.* Surface Modification of polyethylene by diffuse barrier discharge plasma. *Polymer Engineering and Science* (2012) 1-8.
- [8] *F. Arefi-Khonsaria, M. Tatouliana, F. Bretagnola, O. Bouloussab, F. Rondelez.* Processing of polymers by plasma technologies. *Surface & Coatings Technology* 200 (2005) 14 – 20.
- [9] *W. Kun, L. Jian, R. Chunsheng, W. Dezheng, W. Younian.* Surface modification of polyethylene (PE) films using dielectric barrier discharge plasma at atmospheric pressure. *Plasma Science and Technology*, 10 (4), (2008), 433-437.
- [10] *L. Parali, M.A. Kurbanov, A.A. Bayramov, F.N. Tatarard, I.S. Ramazanova & G.X. Huseynova.* Effects of electric discharge plasma treatment on the thermal conductivity of polymer–metal nitride/carbide composites. *Journal of Electronic Materials* 44 (11) (2015) 4322–4333.
- [11] *M. Tahara, N.K. Cuong, Y. Nakashima.* Improvement in adhesion of polyethylene by glow-discharge plasma. *Surface and Coatings Technology* 174–175 (2003) 826-830.
- [12] *R. Morent, N. De Geyter, T. Jacobs, S. Van Vlierbergh, P. Dubruel, C. Leys, E. Schacht.* Plasma-polymerization of HMDSO using an atmospheric Pressure dielectric barrier discharge plasma process. *Polym.* 6 (2009) 537–542.
- [13] *H. Biederman D. Slavinská.* Plasma polymer films and their future prospects. *Surface and Coatings Technology*. 125(1–3) (2000), 371–376.
- [14] *M.A. Kurbanov, V.A. Gol'dade, S.V. Zotov, I.S. Ramazanova, A.F. Nuraliev, F.F. Yakhyaev, U.V. Yusifova & B.G. Khudayarov.* Generation of craze-formation centers in polymer films under the action of electric discharge plasma. *Technical Physics* 63 (2018) 965–969.
- [15] *A.I. Drachev, A.B. Gil'man.* The synthesis of semiconducting polymers in a low-temperature plasma. *Russian Journal of Physical Chemistry A, Focus on Chemistry* 82 (2008) 1733–1741.
- [16] *F. Truica-Marasescu, M.R. Wertheimer.* Nitrogen-rich plasma-polymer films for biomedical applications plasma process. *Polym.* 5 (2008) 44–57.
- [17] *P.-L. Girard-Lauriault, P. Desjardins, Wolfgang E.S. Unger, A. Lippitz, M.R. Wertheimer.* Chemical characterisation of nitrogen-rich plasma-polymer films deposited in dielectric barrier discharges at atmospheric pressure plasma process. *Polym.* 5 (2008) 631–644.
- [18] *M.A. Kurbanov, I.S. Sultanakhmedova, É.A. Kerimov, Kh.S. Aliev, G.G. Aliev, and G.M. Geidarov.* Plasma crystallization of polymer–ferroelectric/piezoelectric ceramic composites and their piezoelectric properties. *Physics of the Solid State*, 51 (6) (2009) 1223–1230.
- [19] *Y. Kusano.* Atmospheric pressure plasma processing for polymer adhesion: a review. *The Journal of Adhesion*, 90 (2014) 755–777.

Received: 08.02.2023

THE WIGNER DISTRIBUTION FUNCTION OF A SEMICONFINED HARMONIC OSCILLATOR MODEL WITH A POSITION-DEPENDENT MASS AND FREQUENCY IN AN EXTERNAL HOMOGENEOUS FIELD. THE CASE OF PARABOLIC WELL

SHAKIR M. NAGIYEV, SHOYQIYYA A. AMIROVA

*Institute of Physics Ministry of Science and Education of Azerbaijan,
AZ 1143, Baku, H. Javid Ave., 131*

The phase space representation for a semiconfined harmonic oscillator model with the position-dependent mass and frequency in an external homogeneous field is constructed in terms of the Wigner distribution function. It is expressed through the Bessel function and Laguerre polynomials. Some of the special cases and limits are also discussed.

Keywords: Harmonic oscillator; external homogeneous field; position-dependent mass; Wigner function; limit relations.

PACS: 03.65.-w; 02.30. Hq; 03.65.Ge

1. INTRODUCTION

As is known, one of the formulations of quantum mechanics is its formulation in the phase space [1-5]. This formulation uses concepts that are common to both quantum and classical mechanics. It makes it possible to describe the picture of quantum phenomena using, as far as possible, the classical language. This formulation deals only with c-numerical quantities and equations, and not with operators, which sometimes simplifies the mathematical description of a given quantum system. The main tools of the phase formulation of quantum mechanics are quantum distribution functions. To pass to this formulation from the Schrödinger operator

formalism, it is necessary to replace the operators of physical quantities with their Weyl transformations [6], and the wave functions with quantum distribution functions.

Among the various quantum distributions functions that exist, the Wigner quantum distribution function is well known. Wigner function W depends on momentum p and coordinates x particles and in the general case on time t , those $W = W(p, x, t)$. Introduced in 1932, the Wigner function is widely used to describe various physical quantum systems. The Wigner quantum distribution function is expressed in terms of the Schrödinger wave function $\psi(x, t)$ using the formula:

$$W(x, p, t) = \frac{1}{2\pi\hbar} \int \psi^*(x - \frac{x'}{2}, t) \psi(x + \frac{x'}{2}, t) e^{-ipx'/\hbar} dx. \tag{1.1}$$

At present there exist a lot of papers with computation of the Wigner function of the various constant [7-10] and position-dependent mass [11-17] quantum relativistic and nonrelativistic harmonic oscillator models.

On the other hand, it is also well known that the construction and study of models of dynamic quantum physical systems with coordinate-dependent mass has long attracted the attention of scientists [18–37]. Such quantum systems play an important role in studying the physical and electronic properties of semiconductors [22], quantum wells and quantum dots [23], clusters ^3He [24], quantum liquids [25], graded alloys, semiconductor heterostructures [26], etc.

The aim of this work is to construct the Wigner quantum distribution function for a linear oscillator model with a position-dependent mass and frequency in an external homogeneous field [38].

2. WIGNER QUANTUM DISTRIBUTION FUNCTION FOR A LINEAR HARMONIC OSCILLATOR WITH CONSTANT MASS IN A UNIFORM EXTERNAL FIELD

Let us write the Schrödinger equation describing the motion of a linear harmonic oscillator with a constant mass in a uniform external field

$$\left(\frac{\hat{p}^2}{2m_0} + \frac{m_0\omega_0^2 x^2}{2} + gx \right) \psi^{HO}(x) = E^{HO} \psi^{HO}(x), \tag{2.1}$$

where $\hat{p} = -i\hbar\partial_x$ is the momentum operator, m_0 and ω_0 are constant mass and frequency of the oscillator, equation (2.1) is defined on the entire real axis $-\infty < x < \infty$.

It is well known that the exact solution of Eq. (2.1) is expressed in terms of the Hermite polynomials

$$\psi_n^{HO}(x) = c_n^{HO} e^{-\frac{1}{2}(\xi + \xi_0)^2} H_n(\xi + \xi_0), n = 0, 1, 2, 3 \dots, \tag{2.2}$$

and the discrete energy spectrum corresponding to the wave functions is equidistant

$$E_n^{\text{HO}} = \hbar\omega_0 \left(n + \frac{1}{2} \right) + \frac{m_0\omega_0^2 x^2}{2}, \quad n = 0,1,2,3 \dots \quad (2.3)$$

Here we use the following notation

$$\xi = \lambda_0 x, \quad \xi_0 = \lambda_0 x_0, \quad x_0 = \frac{g}{m_0\omega_0^2}, \quad \lambda_0 = \sqrt{\frac{m_0\omega_0}{\hbar}}. \quad (2.4)$$

From the orthonormalization condition for wave functions (2.2)

$$\int_{-\infty}^{\infty} \psi_n^{*\text{HO}}(x) \psi_m^{\text{HO}}(x) dx = \delta_{nm} \quad (2.5)$$

we find the normalization constant as follows

$$c_n^{\text{HO}} = \sqrt[4]{\frac{\lambda_0^2}{\pi}} \frac{1}{\sqrt{2^n n!}}. \quad (2.6)$$

Substituting (2.2) into (1.1) leads to the following expression for the Wigner function for a linear harmonic oscillator in an external uniform field

$$W_n^{\text{HO}}(p, x) = \frac{(-1)^n}{\pi\hbar} e^{-(\xi+\xi_0)^2 - \eta^2} L_n(2\eta^2 + 2(\xi + \xi_0)^2), \quad (2.7)$$

where $L_n(x)$ are Laguerre polynomials, and $\eta = p/\lambda_0\hbar$. Formula (2.7) can also be written in operator form [11].

$$W_n^{\text{HO}}(p, x) = \frac{1}{\pi\hbar} \frac{1}{2^n n!} H_n \left(\xi + \xi_0 - \frac{i}{2} \partial_\eta \right) H_n \left(\xi + \xi_0 + \frac{i}{2} \partial_\eta \right) e^{-(\xi+\xi_0)^2 - \eta^2}. \quad (2.8)$$

2. THE LINEAR HARMONIC OSCILLATOR WITH POSITION DEPENDENT MASS AND FREQUENCY IN THE EXTERNAL HOMOGENEOUS FIELD WITH A LIMITED PARABOLIC WELL

Linear harmonic oscillator model with a position dependent mass $M(x) = \frac{a^2 m_0}{(a+x)^2}$ and frequency $\omega = \omega_0 \left(1 + \frac{x}{a} \right)$, ($a+x > 0$) in an external uniform field $V_{ext}(x) = g(x)$, considered in [38] is described by the Schrödinger equation

$$[H_0 + V_{eff}(x)]\psi(x) = E\psi(x), \quad a+x > 0. \quad (3.1)$$

Here H_0 is the free Hamiltonian with a position dependent mass

$$H_0 = \frac{1}{2} \hat{p} \frac{1}{M(x)} \hat{p} + V_{free}(x), \quad (3.2)$$

and $V_{free}(x)$ is the contribution from the free Hamiltonian to the potential energy, which depends on the mass function $M(x)$ and on the real parameters $A_f, B_f \in R(-\infty, \infty)$ (see [38,39,40]). It has a form

$$V_{free}(x) = A_f \frac{\hbar^2 M'^2}{2M^3} - B_f \frac{\hbar^2 M''}{4M^2}. \quad (3.3)$$

The effective potential is equal to the sum of the interaction potential $V(x)$ and free potential, i.e.

$$V_{eff}(x) = V(x) + V_{free}(x). \quad (3.4)$$

Interaction potential $V(x)$ we choose in the form

$$V(x) = \begin{cases} \frac{M(x)\omega^2 x^2}{2} + gx, & x+a > 0, \\ \infty, & x+a < 0, \end{cases} \quad (3.5)$$

where g is a force and $M(x)\omega^2(x) = m_0\omega_0^2$.

In this case, when $M(x) = \frac{a^2 m_0}{(a+x)^2}$ we have $V_{free}(x) = V_0 = \text{const}$. The solution of the equation (3.1) with the potential (3.4)

$$\psi_n^g(x) = c_n^g \left(1 + \frac{x}{a}\right)^{A_n} e^{-b^2\left(1+\frac{x}{a}\right)} L_n^{2A_n+1} \left(2b^2 \left(1 + \frac{x}{a}\right)\right), n = 0, 1, 2, \dots, N_g, \quad (3.6)$$

is expressed in terms of the Laguerre polynomials [38]

$$L_n^\alpha(x) = \frac{(\alpha+1)_n}{n!} {}_1F_1(-n, \alpha + 1; x), \quad (3.7)$$

in the following way, where $b = \lambda_0 a$, $A_n = b^2 - n - 1 - b\xi_0$, $N_g = b^2 - 1 - b\xi_0$. The corresponding to the wave functions (3.7) discrete energy spectrum has the form

$$E_n^g = \hbar\Omega_0 \left(n + \frac{1}{2}\right) - \frac{\hbar^2}{2m_0 a^2} n(n+1) - \frac{m_0 \omega_0^2 x_0^2}{2} + V_0, \quad (3.8)$$

where $\Omega_0 = \omega_0 \left(1 - \frac{\xi_0}{b}\right)$ is a renormalized oscillator frequency.

Let us now find the normalization constant c_n^g in (3.7) from the condition

$$\int_{-a}^{\infty} |\psi_n^g(x)|^2 dx = 1. \quad (3.9)$$

To calculate this integral (3.9), we use the formula [41]

$$\int_0^{\infty} x^{\alpha-1} e^{-cx} L_m^\gamma(cx) L_n^\lambda(cx) dx = \frac{(\gamma+1)_n (\lambda-\alpha+1)_n}{m! n! c^\alpha} \Gamma(\alpha) {}_3F_2(-m, \alpha, \alpha - \lambda; \gamma + 1; \alpha - \lambda - n; 1), \quad (3.10)$$

$\text{Re}\alpha > 0$, $\text{Re}c > 0$. In our case we have $\alpha = \gamma = \lambda = 2A_n + 1$, $m = n, c = 1$. As a result, we find

$$c_n^g = (2b^2)^{A_n + \frac{1}{2}} \sqrt{\frac{\lambda_0 n! (2A_n + 1)}{b \Gamma(2A_n + n + 1)}}. \quad (3.11)$$

4. COMPUTATION OF THE WIGNER DISTRIBUTION FUNCTION OF A SEMICONFINED LINEAR HARMONIC OSCILLATOR MODEL WITH POSITION-DEPENDENT MASS AND FREQUENCY IN AN EXTERNAL HOMOGENEOUS FIELD

For our calculations, we will substitute expression (3.7) for the wave function into the definition of the Wigner distribution function

$$W_n^g(p, x) = \frac{|c_n^g|^2}{\pi \hbar} e^{-2b^2\left(1+\frac{x}{a}\right)} \int_{y_1}^{y_2} \left[\left(1 + \frac{x}{a}\right)^2 - \frac{y^2}{a^2} \right]^{A_n} L_n^{2A_n+1} \left(2b^2 \left(1 + \frac{x-y}{a}\right)\right) \times \\ \times L_n^{2A_n+1} \left(2b^2 \left(1 + \frac{x+y}{a}\right)\right) e^{-\frac{2ipy}{\hbar}} dy. \quad (4.1)$$

Integration limits in (4.1) y_1 and y_2 we find from the condition that the argument of the wave function varies in the region $x > -a$, therefore, we have $x - y > -a$ and $x + y > -a$. Hence it follows that $y_1 = -(x + a), y_2 = (x + a)$. Since the boundaries of integration in (4.1) are finite, this integral converges.

We introduce a dimensionless variable $t = y/(x + a)$ and imagine $W_n^g(p, x)$ as

$$W_n^g(p, x) = \sigma_n \cdot I_n, \quad (4.2)$$

$$\sigma_n = \frac{|c_n^g|^2}{\pi \hbar \lambda_0} e^{-\rho b - 2A_n} (b + \xi)^{2A_n+1} = \frac{1}{\pi \hbar} e^{-\rho} [2b(b + \xi)]^{2A_n+1} \cdot \frac{n! (2A_n + 1)}{\Gamma(2A_n + n + 2)},$$

$$I_n = \int_{-1}^1 (1 - t^2)^{A_n} L_n^{2A_n+1}(\rho - \rho t) L_n^{2A_n+1}(\rho + \rho t) e^{-2i\eta(b+\xi)t} dt,$$

where $\rho = 2b(b + \xi), \eta = p/\lambda_0 \hbar$. Using equality

$$t e^{-2i\eta(b+\xi)t} = \frac{i}{2(b + \xi)} \partial_\eta e^{-2i\eta(b+\xi)t}$$

rewrite I_n in operator form

$$I_n = L_n^{2A_n+1}(\rho - ib\partial_\eta)L_n^{2A_n+1}(\rho + ib\partial_\eta) \int_{-1}^1 (1-t^2)^{A_n} e^{-2i\eta(b+\xi)t} dt. \quad (4.3)$$

Here integration can be carried out using the formulas [41]

$$\int_{-a}^a (a^2 - x^2)^{\beta-1} e^{i\lambda x} dx = \sqrt{\pi} \Gamma(\beta) \left(\frac{2a}{\lambda}\right)^{\beta-1/2} J_{\beta-1/2}(a\lambda), \text{Re}\beta > 0, \quad (4.4)$$

where $J_\beta(x)$ is the Bessel function. As a result, we obtain the following operator relation

$$I_n = \sqrt{\pi} \Gamma(A_n + 1) L_n^{2A_n+1}(\rho - ib\partial_\eta) L_n^{2A_n+1}(\rho + ib\partial_\eta) [\eta(b + \xi)]^{-A_n-1/2} J_{A_n+1/2}(2\eta(b + \xi)). \quad (4.5)$$

Taking into account (4.5), we can now write the Wigner function in operator form, i.e.

$$W_n^g(p, x) = \frac{|C_n^g|^2}{\hbar\sqrt{\pi}\lambda_0} \Gamma(A_n + 1) b^{-2A_n} e^{-\rho} L_n^{2A_n+1}(\rho - ib\partial_\eta) L_n^{2A_n+1}(\rho + ib\partial_\eta) \times \\ \times \left(\frac{b+\xi}{\eta}\right)^{A_n+1/2} J_{A_n+1/2}(2\eta(b + \xi)). \quad (4.6)$$

4.1. GROUND STATE WIGNER FUNCTION

From (3.16) we extract the Wigner function of the ground state, which has the form

$$W_0^g(p, x) = \frac{1}{\hbar\sqrt{\pi}} (2A_0 + 1) \frac{\Gamma(2A_0+1)}{\Gamma(2A_0+2)} \left(\frac{4b^2(b+\xi)}{\eta}\right)^{A_0+1/2} e^{-\rho} J_{A_0+1/2}(2\eta(b + \xi)). \quad (4.7)$$

Now taking into account the following well-known relation for the Gamma functions [43]

$$\Gamma(2z) = \frac{2^{2z-1}}{\sqrt{\pi}} \Gamma(z) \Gamma\left(z + \frac{1}{2}\right), \quad (4.8)$$

we can simplify expression (4.7). As a result we obtain the following analytical expression for the ground state Wigner distribution function

$$W_0^g(p, x) = \frac{2}{\hbar} \frac{1}{\Gamma(2A_0+1/2)} \left(\frac{b^2(b+\xi)}{\eta}\right)^{A_0+1/2} e^{-\rho} J_{A_0+1/2}(2\eta(b + \xi)) \quad (4.9)$$

or explicitly

$$W_0^g(p, x) = \frac{2}{\hbar} \frac{1}{\Gamma(b^2-b\xi_0-1/2)} e^{-b^2-b\xi_0} \left(\frac{b^2(b+\xi)}{\eta}\right)^{b^2-b\xi_0-1/2} J_{b^2-b\xi_0-1/2}(2\eta(b + \xi)), \quad (4.10)$$

where $A_n = A_0 - n$, $A_0 = b^2 - b\xi_0 - 1$.

For the case of the absence of the external field $g = 0$ and $\xi_0 = 0$, and the Wigner function of the ground state (4.8) slightly simplifies as follows:

$$W_0^0(p, x) = \frac{2}{\hbar} \frac{1}{\Gamma(b^2-1/2)} e^{-b^2-b\xi_0} \left(\frac{b^2(b+\xi)}{\eta}\right)^{b^2-1/2} J_{b^2-1/2}(2\eta(b + \xi)). \quad (4.11)$$

Taking into account that the Wigner function of the ground state (4.2) is exactly computed in terms of the Bessel functions, then one can try to compute its analytical expression for arbitrarily excited states n . For this, one needs to go to the expression (4.2). Its integrand mainly consists of the product of two Lagerre polynomials with different arguments. One applies there the following known finite sum for such kind of products [42]

$$L_n^\alpha(x) L_n^\alpha(y) = \frac{\Gamma(\alpha+n+1)}{n!} \sum_{k=0}^n \frac{(xy)^k}{k! \Gamma(\alpha+k+1)} L_{n-k}^{\alpha+2k}(x+y). \quad (4.12)$$

Its substitution at (4.2) yields

$$I_n = \frac{\Gamma(2A_n+n+2)}{n!} \sum_{k=0}^n \frac{\rho^{2k}}{k! \Gamma(2A_n+n+2)} L_{n-k}^{(2A_n+n+2)}(2\rho) \int_{-1}^1 (1-t^2)^{A_n+k} e^{-2i\eta(b+\xi)t} dt. \quad (4.13)$$

Applying again the integral formula (4.4), for I_n we get

$$I_n = \sqrt{\pi} \frac{\Gamma(2A_n+n+2)}{n!} [\eta(b+\xi)]^{A_n-1/2} \sum_{k=0}^n Q_k, \quad (4.14)$$

where

$$Q_k = \frac{\Gamma(A_n+k+1)}{k! \Gamma(2A_n+k+2)} \left[\frac{4b^2(b+\xi)}{\eta} \right]^k L_{n-k}^{(2A_n+2k+1)}(2\rho) J_{A_n+k+1/2}(2\eta(b+\xi)). \quad (4.15)$$

So the Wigner distribution function of the semiconfined quantum harmonic oscillator model with position dependent mass and frequency in the presence of the external homogeneous field takes a form

$$W_n^g(p, x) = \frac{1}{\hbar\sqrt{\pi}} (A_n + 1) e^{-\rho} \times \\ \times \sum_{k=0}^n \frac{\Gamma(A_n+k+1)}{k! \Gamma(2A_n+k+2)} \left[\frac{2b\rho}{\eta} \right]^{A_n+k+1/2} L_{n-k}^{(2A_n+2k+1)}(2\rho) J_{A_n+k+1/2}(2\eta(b+\xi)), \quad (4.16)$$

or explicitly

$$W_n^g(p, x) = \frac{1}{\hbar\sqrt{\pi}} (2b^2 - 2b\xi_0 - 2n - 1) e^{-2b(b+\xi)} \sum_{k=0}^n \frac{\Gamma(b^2 - b\xi_0 - n + k)}{k! \Gamma(2b^2 - 2b\xi_0 - 2n + k)} \times \\ \times \left[\frac{4b^2(b+\xi)}{\eta} \right]^{b^2 - b\xi_0 - n + k - 1/2} L_{n-k}^{2b^2 - 2b\xi_0 - 2n + 2k - 1}(2b(b+\xi)) J_{b^2 - b\xi_0 - n + k - 1/2}(2\eta(b+\xi)). \quad (4.17)$$

Absence of the external field again slightly simplifies (4.17) due to that $g = 0$ ($\xi_0 = 0$):

$$W_n^0(p, x) = \frac{1}{\hbar\sqrt{\pi}} (2b^2 - 2n - 1) e^{-2b(b+\xi)} \sum_{k=0}^n \frac{\Gamma(b^2 - n + k)}{k! \Gamma(2b^2 - 2n + k)} \times \\ \times \left[\frac{4b^2(b+\xi)}{\eta} \right]^{b^2 - n + k - 1/2} L_{n-k}^{2b^2 - 2n + 2k - 1}(2b(b+\xi)) J_{b^2 - n + k - 1/2}(2\eta(b+\xi)). \quad (4.18)$$

We obtained an exact expression for the Wigner distribution function of our model of the linear harmonic oscillator with position dependent mass and frequency in the external homogeneous field.

5. LIMIT CASE $a \rightarrow \infty$ (or $b \rightarrow \infty$)

In this section, we will find the limit of the wave function (3.6) and the Wigner distribution function (4.6). In doing so, we will proceed from asymptotic formulas valid for $|x| \ll 1$ and $|z| \rightarrow \infty$:

$$\sqrt{1+x} = 1 + \frac{1}{2}x - \frac{1}{8}x^2, \quad \ln(1 \pm x) \cong \pm x - \frac{1}{2}x^2, \\ \Gamma(z+1) \cong \sqrt{2\pi z} e^{z \ln z - z}, \quad (5.1)$$

as well as the limit formula for Laguerre polynomials [44]

$$\left(\frac{\alpha}{2}\right)^{\frac{n}{2}} L_n^\alpha(\alpha + \sqrt{2\alpha}x) = \frac{(-1)^n}{n!} H_n(x). \quad (5.2)$$

5.1. Limit of wave functions. To calculate the limit of the wave function (3.6) at $a \rightarrow \infty$, first, we find the asymptotics of each of the factors separately in (3.6).

a) In c_n^g for the Gamma function we have

$$\Gamma(2A_n + k + 2) = \Gamma(2b^2 - 2b\xi_0 - n) \cong \frac{\sqrt{\pi}}{b} e^{\sigma_1},$$

$$\sigma_1 \cong (2b^2 - 2b\xi_0 - n) \ln 2b^2 + \xi_0^2 - 2b^2.$$

Hence,

$$C_n^g \cong \frac{\sqrt[4]{\lambda_0^2}}{\pi} \sqrt{n!} (2b^2)^{-n/2} e^{-b^2 - \frac{1}{2}\xi_0^2}. \quad (5.3)$$

$$b \left(1 + \frac{\xi}{b}\right)^{A_n} = e^{A_n \ln\left(1 + \frac{\xi}{b}\right)} \cong e^{\sigma_2}, \sigma_2 \cong b\xi - \frac{1}{2}\xi^2 - \xi\xi_0. \quad (5.4)$$

Substituting (5.3) and (5.4) into (3.6), we have for $b \rightarrow \infty$

$$\psi_n^g(x) \cong \frac{\sqrt[4]{\lambda_0^2}}{\pi} \sqrt{n!} e^{-\frac{1}{2}(\xi + \xi_0)^2} (2b^2)^{-n/2} L_n^{2b^2 - 2b\xi_0 - 2n - 1} (2b^2 + 2b\xi). \quad (5.5)$$

Now to calculate the limit

$$Z_n = \lim_{b \rightarrow \infty} (2b^2)^{-n/2} L_n^{2b^2 - 2b\xi_0 - 2n - 1} (2b^2 + 2b\xi), \quad (5.6)$$

we introduce the notation $P_n = 2b^2 - 2b\xi_0 - 2n - 1$, $\alpha = 2b^2$, $z = 2b^2 + 2b\xi$ and obtain the recurrent formula for the Laguerre polynomials $L_n^{\alpha}(z)$.

Since for the Laguerre polynomials $L_n^{\alpha}(z)$ the recurrence relation is valid [42]

$$(n + 1)L_{n+1}^{\alpha}(z) - (2n + \alpha + 1 - z)L_n^{\alpha}(z) + (n + \alpha)L_{n-1}^{\alpha}(z) = 0, \quad (5.7)$$

then, the recurrence relation for $L_n^{P_n}(z)$ will have

$$(n + 1)L_{n+1}^{P_{n+1}}(z) - (2n + P_n + 1 - z)L_n^{P_{n+1}}(z) + (n + P_{n+1})L_{n-1}^{P_{n+1}}(z) = 0, \quad (5.8)$$

We now prove by mathematical induction the following limit relation

$$Z_n = \lim_{\alpha \rightarrow \infty} (\alpha)^{-n/2} L_n^{\alpha - \sqrt{2\alpha}\xi_0 - 2n - 1} (\alpha + \sqrt{2\alpha}\xi_0) = \frac{(-1)^n}{n!} H_n(\xi + \xi_0). \quad (5.9)$$

Proof. First we write explicitly the Laguerre and Hermite polynomials for the first few values n

$$L_0^{\alpha}(z) = 1, L_1^{\alpha}(z) = 1 + \alpha - z, L_2^{\alpha}(z) = \frac{1}{2} [(1 + \alpha - z)(3 + \alpha - z) - 1 - \alpha],$$

$$H_0(z) = 1, H_1(z) = 2z, H_2(z) = 4z^2 - 2. \quad (5.10)$$

We will also need a recurrence relation for the Hermite polynomial

$$H_{n+1}(z) = 2zH_n(z) - 2nH_{n-1}(z). \quad (5.11)$$

Using these expressions, we directly obtain that for $n = 1$ and $n = 2$ relation (5.9) is true:

$$Z_1 = \lim_{\alpha \rightarrow \infty} (\alpha)^{-1/2} L_1^{\alpha - \sqrt{2\alpha}\xi_0 - 3} (\alpha + \sqrt{2\alpha}\xi_0) = -\sqrt{2}(\xi + \xi_0) = -\frac{1}{\sqrt{2}} H_1(\xi + \xi_0)$$

$$Z_2 = \lim_{\alpha \rightarrow \infty} (\alpha)^{-1} L_2^{\alpha - \sqrt{2\alpha}\xi_0 - 5} (\alpha + \sqrt{2\alpha}\xi_0) = (\xi + \xi_0)^2 - \frac{1}{2} = \frac{1}{4} H_2(\xi + \xi_0). \quad (5.12)$$

Let us now prove that relation (5.9), which is valid in the cases $n = 1$ и $n = 2$, also performed for an arbitrary $n > 2$. For this, we assume that relation (5.9) holds for the polynomials $L_{n+1}^{P_{n+1}}(z)$ and $L_{n-1}^{P_{n+1}}(z)$ at some n . Then it also holds for $L_{n+1}^{P_{n+1}}(z)$. Indeed, we multiply by $\alpha^{-\frac{n+1}{2}}$ both sides of the recurrence relation for Laguerre polynomials $L_{n+1}^{P_{n+1}}(z)$ (5.8)

$$Z_{n+1} = \lim_{\alpha \rightarrow \infty} \alpha^{-\frac{n+1}{2}} L_{n+1}^{\alpha - \sqrt{2\alpha}\xi_0 - 2n - 3} (\alpha + \sqrt{2\alpha}\xi_0) =$$

$$= \frac{(-1)^{n+1}}{(n+1)! \sqrt{2^{n+1}}} [2(\xi + \xi_0)H_n(\xi + \xi_0) - 2nH_{n-1}(\xi + \xi_0)]. \quad (5.13)$$

According to (5.11), the last expression is

$$Z_{n+1} = \frac{(-1)^{n+1}}{(n+1)! \sqrt{2^{n+1}}} H_{n+1}(\xi + \xi_0). \quad (5.14)$$

This completes the proof.

5.2. Limit of the Wigner distribution function for the ground state.

To calculate this limit, we find the asymptotics of each of the factors in (4.10). We have

$$\text{a) } \frac{1}{\Gamma(b^2 - b\xi - 1/2)} \cong \frac{1}{\sqrt{2\pi}} (b^2)^{-A_0} e^{b^2 - \frac{1}{2}\xi_0^2}, \quad (5.15a)$$

$$\text{b) } \left[\frac{b^2(b+\xi)}{\eta} \right]^{b^2 - b\xi_0^2 - 1/2} \cong \left(\frac{b^3}{\eta} \right)^{A_0 + 1/2} e^{b\xi - \frac{1}{2}\xi^2 - \xi\xi_0}, \quad (5.15b)$$

$$\text{c) } J_{b^2 - b\xi_0 - 1/2}(2\eta(b + \xi)) \cong \frac{1}{b\sqrt{2\pi}} \left(\frac{\eta}{b} \right)^{A_0 + 1/2} e^{b^2 + b\xi - \eta^2 - \xi_0^2 - \xi\xi_0}. \quad (5.15c)$$

Note that the asymptotic behavior of the Bessel function in (5.15c) was found using the asymptotic formula (7.13, 8(14)) for $J_p(x)$, given in [42]

$$J_p(x) \cong \frac{1}{\sqrt{2\pi^4} \sqrt{p^2 - x^2}} \exp\left(\sqrt{p^2 - x^2} - p \operatorname{Arch} \frac{p}{x}\right), p > x > 0, p \rightarrow \infty. \quad (5.16)$$

We emphasize that there is a typo in the formula (7.13, 8(14)) in [42]: instead of $\operatorname{Arsh} \frac{p}{x}$ should stand $\operatorname{Arch} \frac{p}{x}$. We took this correction into account in formula (4.16). To obtain (5.15c) we left in (5.16) the main terms in powers b^{-1} :

$$\begin{aligned} \sqrt[4]{p^2 - x^2} &\cong b, \quad \sqrt{p^2 - x^2} \cong A_0 + \frac{1}{2} - 2\eta^2, \\ \operatorname{Arch} \frac{p}{x} &\cong \ln\left(\frac{b}{\eta}\right) - \frac{\xi + \xi_0}{b} + \frac{\xi^2 - 1 - 2\eta^2 - \xi_0^2}{2b^2}. \end{aligned}$$

As a result of substituting asymptotics (5.15) into (3.21), we find that the limit of the Wigner distribution function of the ground state coincides with formula (2.7) for $n = 0$, i.e.

$$\lim_{b \rightarrow \infty} W_0^g(p, x) = \frac{1}{\pi\hbar} e^{-\eta^2 - (\xi + \xi_0)^2} = W_0^{\text{HO}}(p, x). \quad (5.17)$$

5.3. Limit of the Wigner distribution function for n excited state. To calculate the limit of $W_n^g(p, x)$ it is convenient to start from equality (4.6). Let's rewrite it in the form

$$W_n^g(p, x) = L_n^{2A_n+1}(\rho - ib\partial_\eta) L_n^{2A_n+1}(\rho + ib\partial_\eta) \Omega_n^g(p, x), \quad (5.18)$$

where

$$\Omega_n^g(p, x) = \frac{1}{\hbar\sqrt{\pi}} \frac{n!(2A_n+1)\Gamma(A_n+1)}{\Gamma(2A_n+n+2)} e^{-\rho} \left(\frac{4b^3}{\eta}\right)^{A_n+1/2} \left(1 + \frac{\xi}{b}\right)^{A_n+1/2} J_{A_n+1/2}(2\eta(b + \xi)). \quad (5.19)$$

As above, we find the asymptotics of each factor (5.19) as $b \rightarrow \infty$. We have

$$\begin{aligned} \text{a) } \Gamma(A_n + 1) &\cong \sqrt{2\pi} (b^2)^{A_n+1/2} e^{\gamma_1}, \gamma_1 = -b^2 + \frac{\xi_0^2}{2}, \\ \text{b) } \frac{\Gamma(2A_n+1)}{\Gamma(2A_n+n+2)} &\cong \frac{1}{\Gamma(2A_n+n+1)} \cong \frac{1}{2b\sqrt{\pi}} (2b^2)^{-2A_n-n} e^{\gamma_2}, \gamma_2 = 2b^2 - \xi_0^2, \\ \text{c) } \left(1 + \frac{\xi}{b}\right)^{A_n+1/2} &\cong e^{\gamma_3}, \gamma_3 = b\xi - \frac{\xi^2}{2} - \xi\xi_0, \end{aligned} \quad (5.20)$$

$$d) J_{A_n+1/2}(2\eta(b + \xi)) \cong \frac{1}{b\sqrt{2\pi}} \left(\frac{\eta}{b}\right)^{A_0+1/2} e^{\gamma_4}, \gamma_4 = b^2 + b\xi - \eta^2 - \frac{1}{2}(\xi + \xi_0)^2.$$

So for $\Omega_n^g(p, x)$ we get the following asymptotics

$$\Omega_n^g(p, x) \cong \frac{1}{\pi\hbar} n! (2b^2)^{-n} e^{-\eta^2 - \frac{1}{2}(\xi + \xi_0)^2} = n! (2b^2)^{-n} W_0^{\text{HO}}(p, x), \quad (5.21)$$

whose substitution into (4.18) gives

$$\lim_{b \rightarrow \infty} W_n^g(p, x) = n! \lim_{b \rightarrow \infty} (2b^2)^{-n} L_n^{2A_n+1}(\rho - ib\partial_\eta) L_n^{2A_n+1}(\rho + ib\partial_\eta) W_0^{\text{HO}}(p, x). \quad (5.22)$$

So that $\rho \pm ib\partial_\eta = \alpha + \sqrt{2\alpha} \left(\xi \pm \frac{i}{2}\partial_\eta\right)$, where $\alpha = 2b^2$, according to (4.9) will have

$$\begin{aligned} \lim_{b \rightarrow \infty} (2b^2)^{-n} L_n^{2A_n+1}(\rho - ib\partial_\eta) L_n^{2A_n+1}(\rho + ib\partial_\eta) &= \\ = \frac{1}{2^{n(n!)^2}} H_n\left(\xi + \xi_0 - \frac{i}{2}\partial_\eta\right) H_n\left(\xi + \xi_0 + \frac{i}{2}\partial_\eta\right). \end{aligned} \quad (5.23)$$

Taking into account (5.22) and (5.23) we find

$$\lim_{b \rightarrow \infty} W_n^g(p, x) = \frac{1}{\pi\hbar 2^{n(n!)^2}} H_n\left(\xi + \xi_0 - \frac{i}{2}\partial_\eta\right) H_n\left(\xi + \xi_0 + \frac{i}{2}\partial_\eta\right) e^{-\eta^2 - (\xi + \xi_0)^2}, \quad (5.24)$$

i.e. at $b \rightarrow \infty$ the Wigner function of the model of a linear harmonic oscillator with position dependent mass and frequency in an external uniform field transforms into the Wigner function for a linear harmonic oscillator with constant mass and frequency in an external uniform field.

In this work, we have found an exact expression for the Wigner function of a quantum linear harmonic oscillator with position dependent mass and frequency in an external uniform field in the case of a semiconfined quantum parabolic well. Although the wave function of the considered system is defined on the half-line $(-a; \infty)$, integration in the definition of the Wigner function is carried out in the finite region $(- (x + a); x + a)$.

-
- | | |
|---|--|
| <p>[1] <i>E.P. Wigner</i>. On the quantum correction for thermodynamic equilibrium, <i>Phys.Rev.</i>, 40 749 1932.</p> <p>[2] <i>M. Hillery, R.F. O'Connell, M.O. Scully and E.P. Wigner</i>. Distribution functions in physics: Fundamentals, <i>Phys. Rep.</i>, 106 121, 1984.</p> <p>[3] <i>H.-W. Lee</i>. Theory and application of the quantum phase-space distribution functions, <i>Phys. Rep.</i> 259, 1995, 147-211.</p> <p>[4] <i>V.I. Tatarskiĭ</i>. The Wigner representation of quantum mechanics, <i>Sov. Phys. Usp.</i>, 26 311, 1983.</p> <p>[5] <i>K. Husimi</i>, Some formal properties of the density matrix, <i>Proc. Phys.-Math. Soc. Japan</i>, 22 264, 1940.</p> <p>[6] <i>H. Weyl</i>. "Quantenmechanik und Gruppentheorie" <i>Z. Phys</i> 46 (1927) 1-33.</p> <p>[7] <i>R.W. Davies and K.T.R. Davies</i>. On the Wigner distribution function for an oscillator, <i>Ann.Phys. (N.Y.)</i>, 89 261-273, 1975.</p> <p>[8] <i>N.M. Atakishiyev, Sh.M. Nagiyev and K.B. Wolf</i>. Wigner distribution functions for a relativistic linear oscillator, <i>Theor.Math,Phys.</i>, 114 322 (1998).</p> <p>[9] <i>E. I. Jafarov, S. Lievens, S. M. Nagiyev, J. Van der Jeught</i>. The Wigner functions of q-deformed harmonic oscillator model, <i>J.Phys. A: Math. Theor.</i>, 40 5427-5441, 2007.</p> | <p>[10] <i>E. I. Jafarov, S. Lievens and J. Van der Jeught</i>. The Wigner distribution functions for the one-dimensional parabolic oscillator, <i>J.Phys. Theor.</i>, 41 235301, 2008.</p> <p>[11] <i>S.M. Nagiyev, G.H. Guliyeva and E.I. Jafarov</i>. The Wigner functions of the relativistic finite-difference oscillator in an external field, <i>J.Phys. A: Math. Theor.</i>, 42 454015, 2009.</p> <p>[12] <i>K. Li, J. Wang, S. Dulat and K. Ma</i>. Wigner functions for Klein-Gordon oscillators in non-commutative space, <i>Int.J.Theor.,Phys.</i>, 49 134-143, 2010.</p> <p>[13] <i>M. Kai, W. Jian-Hua and Y. Yi</i>. Wigner function for the Dirac oscillator in spinor space, <i>Chinese Phys.C</i>, 35 11-15, 2011.</p> <p>[14] <i>J. Van der Jeugt</i>. A Wigner distribution function for finite oscillator systems, <i>J.Phys. A: Math. Theor.</i>, 46 475302, 2013.</p> <p>[15] <i>S. Hassanabadi and M. Ghominejad</i>. Wigner function for Klein-Gordon oscillator in commutative and non-commutative space, <i>Eur. Phys. J. Plus</i>, 131 212, 2016.</p> <p>[16] <i>Z.-d. Chen and G. Chen</i>. Wigner function of the position-dependent effective Schrodinger equation, <i>Phys. Scr.</i>, 73 354-358, 2006.</p> <p>[17] <i>A. de Souza Dutra and J.A. de Oliveira</i>. Wigner distribution for a class of isospectral position-dependent mass systems, <i>Phys. Scr.</i>, 78 035009, 2008.</p> |
|---|--|

- [18] *E.I. Jafarov, S.M. Nagiyev, R. Oste, J. Van der Jeugt*. “Exact solution of the position-dependent effective mass and angular frequency Schrödinger equation: harmonic oscillator model with quantized confinement parameter”, *J. Phys. A: Math. Theor.*, 53:48, 2020, 485301, 14 pp.
- [19] *D.J. BenDaniel, C.B. Duke*. “Space-charge effects on electron tunneling”, *Phys. Rev.*, 152:2, 1966, 683–692.
- [20] *O. Von Roos*. “Position-dependent effective masses in semiconductor theory”, *Phys. Rev. B*, 27:12, 1983, 7547–7552.
- [21] *J.-M. L’evy-Leblond*. “Position-dependent effective mass and Galilean invariance”, *Phys. Rev. A*, 52:3, 1995, 1845–1849.
- [22] *G. Bastard*. *Wave Mechanics Applied to Semiconductor Heterostructure*, Les Edition de Physique, Paris, 1988.
- [23] *P. Harrison*. *Quantum Wells, Wires and Dots: Theoretical and Computational Physics*, John Wiley and Sons, New York, 2000.
- [24] *M. Barranco, M. Pi, S. M. Gatica, E.S. Hern’andez, J. Navarro*. “Structure and energetics of mixed ^4He - ^3He drops”, *Phys. Rev. B*, 56:14, 1997, 8997–9003.
- [25] *F. Arias de Saavedra, J. Boronat, A. Polls, A. Fabrocini*. “Effective mass of one ^4He atom in liquid ^3He ”, *Phys. Rev. B*, 50:6, 1994, 4248–4251.
- [26] *T. Gora, F. Williams*. “Theory of electronic states and transport in graded mixed semiconductors”, *Phys. Rev.*, 177:3, 1969, 1179–1182.
- [27] *Q.-G. Zhu, H. Kroemer*. “Interface connection rules for effective-mass wave functions at an abrupt heterojunction between two different semiconductors”, *Phys. Rev. B*, 27:6, 1983, 3519–3527.
- [28] *H. Raibongshi, N. N. Singh*. “Construction of exactly solvable potentials in the D-dimensional Schrödinger equation with coordinate-dependent mass using the transformation method”, *TMF*, 183:2, 2015, 312–328.
- [29] *N. Amir, S. Iqbal*. “Algebraic solutions of shape-invariant position-dependent effective mass systems”, *J. Math. Phys.*, 57:6, 2016, 062105.
- [30] *B. Roy*. “Lie algebraic approach to singular oscillator with a position-dependent mass”, *Europhys. Lett.*, 72:1, 2005, 1–6.
- [31] *J. Yu, S.-H. Dong*. “Exactly solvable potentials for the Schrödinger equation with spatially dependent mass”, *Phys. Lett. A*, 325, 2004, 194–198.
- [32] *J.R.F. Lima, M. Vieira, C. Furtado, F. Moraes, C. Filgueiras*. “Yet another position-dependent mass quantum model”, *J. Math. Phys.*, 53:7, 2012, 072101.
- [33] *C. Quesne, V. M. Tkachuk*. “Deformed algebras, position-dependent effective masses and curved spaces: an exactly solvable Coulomb problem”, *J. Phys. A: Math. Gen.*, 37:14, 2004, 4267–4281, arXiv: math-ph/0403047.
- [34] *J. F. Cariñena, M. F. Rañada, M. Santander*. “Quantization of Hamiltonian systems with a position dependent mass: Killing vector fields and Noether momenta approach”, *J. Phys. A: Math. Theor.*, 50:46, 2017, 465202, 20 pp.
- [35] *E. I. Jafarov, S. M. Nagiyev, A. M. Jafarova*. “Quantum-mechanical explicit solution for the confined harmonic oscillator model with the von Roos kinetic energy operator”, *Rep. Math. Phys.*, 86:1, 2020, 25–37.
- [36] *E. I. Jafarov, Sh. M. Nagiyev*. “Angular part of the Schrödinger equation for the potential Oto as a harmonic oscillator with coordinate-dependent mass in a homogeneous gravitational field”, *TMF*, 207:1, 2021, 58–71.
- [37] *A. de Souza Dutra, A. de Oliveira*. “Two-dimensional position-dependent massive particles in the presence of magnetic fields”, *J. Phys. A: Math. Theor.*, 42:2, 2009, 025304, 13 pp.
- [38] *Shakir M. Nagiyev, Shovqiyya A. Amirova*, Model of a linear harmonic oscillator with a position-dependent mass in the external homogeneous field. The case of a parabolic well, *AJP Physics* 28:4, 2022 section En, 36-41.
- [39] *S.M. Nagiyev*. On two direct limits relating pseudo-Jacobi polynomials to Hermite polynomials and the pseudo-Jacobi oscillator in a homogeneous gravitational field. *Theor. Math. Phys.* 210, 2022, 121.
- [40] *S.M. Nagiyev, C. Aydin, A.I. Ahmadov, S.A. Amirova*. “Exactly solvable model of the linear harmonic oscillator with a positiondependent mass under external homogeneous gravitational field”, *Eur. Phys. J. Plus.*, 540: 137, 2022,13.
- [41] *A.P. Prudnikov, Yu.A. Brychkov, O. I. Marichev*, “Integrals and series”, vol. 2: Special functions, Nauka, M., 1983.
- [42] *H. Bateman and A. Erd’elyi*. “Higher Transcendental Functions”: 2 (McGraw Hill Publications, New York, 1953).
- [43] *H. Bateman and A. Erd’elyi*. “Higher Transcendental Functions”: 1 (McGraw Hill Publications, New York, 1953).
- [44] *R. Koekoek, P.A. Lesky and R.F. Swarttouw*. “Hypergeometric Orthogonal Polynomials and their q-Analogues”, (Springer, Berlin 2010).

Received: 27.02.2023

METHODS FOR SYNTHESIS OF NANOTUBES AND STRUCTURE (review article)

A.M. ALIYEVA

*Institute of Physics Ministry of Science and Education,
AZ 1143, Baku, H. Javid Ave., 131*

Carbon nanotubes are discussed in this review structure and synthesis methods. Carbon nanotubes synthesis by variety methods and each of the mechanisms have precise features that can be specify properties of carbon nanotubes. Arc discharge, laser ablation and chemical vapor deposition are most common methods and mechano thermal, electrolysis and flame are others ways for synthesis carbon nanotubes.

Keywords: Carbon nanotubes, synthesis methods of carbon nanotubes, cvd, arc discharge, mechano thermal.

PACS : 73.63.Fg, 73.22.- f, 78.67.Ch, 61.46.Fg

Introduction

Nanoscience is the study, understanding and control of phenomena and manipulation of material at the nanoscale, so nanoscience is the world of atoms, molecules, macromolecules, quantum dots, and macromolecular assemblies. Research in nanoscience is an interdisciplinary knowledge which means that it is a whole knowledge on fundamental properties of nanosized objects but not limited to physics, chemistry, biology, medicine, engineering, and materials science. Nanotechnology describes many diverse technologies and tools, which do not always appear to have much in common! Therefore, it is better to talk about nanotechnologies, in the plural (2). Carbon nanotubes (CNTs), composed of graphene/graphite sheets, have been used since the 1990s and become one of the most important materials owing to its massive applications in energy, environmental and life sciences.

Carbon nanotube (CNT) is one form of carbon, with nanometersized diameter and micrometer-sized length (where the length to diameter ratio exceeds 1000). The atoms are arranged in hexagons, the same arrangement as in graphite. The structure of CNT consists of enrolled cylindrical graphitic sheet (called graphene) rolled up into a seamless cylinder with diameter of the order of a nanometer. It is understood that CNT is the material lying in between fullerenes and graphite as a quite new member of carbon allotropes (3).

In the [1] article authors studied the structure of carbon nanotubes. Carbon nanotubes are members of the fullerene structural family, which also includes buckyballs. Whereas buckyballs are spherical in shape, a CNT is cylindrical, the ends of some CNTs are open; the others are closed with full fullerene caps. CNTs name is derived from their size, since the diameter of a CNT is on the order of a few nanometers (approximately 50,000 times smaller than the width of a human hair), while they can be up to several micrometer in length. Commercial applications for CNT have been rather slow to develop, however, primarily because of the high production costs of the best quality CNTs.

The current huge interest in CNTs is a direct consequence of the synthesis of buckminsterfullerene C_{60} , and other fullerenes, in 1985. The discovery that carbon could form stable, ordered structures other than graphite and diamond stimulated researchers worldwide to search for other new forms of carbon. The search was given new impetus when it was shown in 1990 that C_{60} could be produced in a simple arc evaporation apparatus readily available in all laboratories. It was using such an evaporator that the Japanese scientist "Sumio Iijima" discovered fullerene-related CNTs in 1991 (4). The tubes contained at least two layers (multi-walled carbon nanotubes MWCNTs), often many more, and ranged in outer diameter from about 3 nm to 30 nm. They were invariably closed at both ends.

A scanning of some MWCNT is shown in 1993; a new class of CNT was discovered, with just a single layer. These (single-walled carbon nanotubes SWCNTs) are generally narrower than the multi-walled tubes, with diameters typically in the range 1–2 nm, and tend to be curved rather than straight.

It was soon established that these new fibers had a range of exceptional properties, and this led to increase of research into CNTs. It is important to note, however, that nanoscale tubes of carbon, produced catalytically, had been known for many years before Iijima's discovery. The main reason why these early tubes did not excite wide interest is that they were structurally rather imperfect, so did not have particularly interesting properties. Recent research has focused on improving the quality of produced CNTs (5).

Structure of CNTs

Carbon nanotubes are sheets of graphite that have been rolled into a tube. A graphene sheet can be rolled more than one way, producing different types of CNTs, (graphene is an individual graphite layer).

CNTs are considered as nearly one-dimensional structures (1D buckytube shape) according to their high length to diameter ratio.

Most important structures are SWCNTs and MWCNTs. A SWCNT is considered as a cylinder with only one wrapped graphene sheet while MWCNTs are similar to a collection of concentric SWCNTs. The length and diameter of these structures differ a lot from those of SWCNTs and, of course, their properties are also very different. The bondings in CNTs is sp^2 and consist of honeycomb lattices and are seamless structure, with each atom joined to three neighbors, as in graphite. The tubes can therefore be considered as rolled up graphene sheets.

The type of CNT depends on how the graphene sheet is oriented on rolling. This can be specified by a vector (called chiral vector), which

defines how the graphene sheet is rolled up. Fig. 1 showing how a hexagonal sheet of graphite is rolled to form a CNT in a vector structure classification.

The vector is determined by two integers (n,m) . Two atoms in a planar graphene sheet are chosen and one is used as origin. The chiral vector C is pointed from the first atom toward the second one and is defined by the relation (6)

$$C = na_1 + ma_2$$

Where: n and m are integers. a_1 and a_2 are the unit cell vectors of the two-dimensional lattice formed by the graphene sheets. The direction of the CNT axis is perpendicular to this chiral vector.

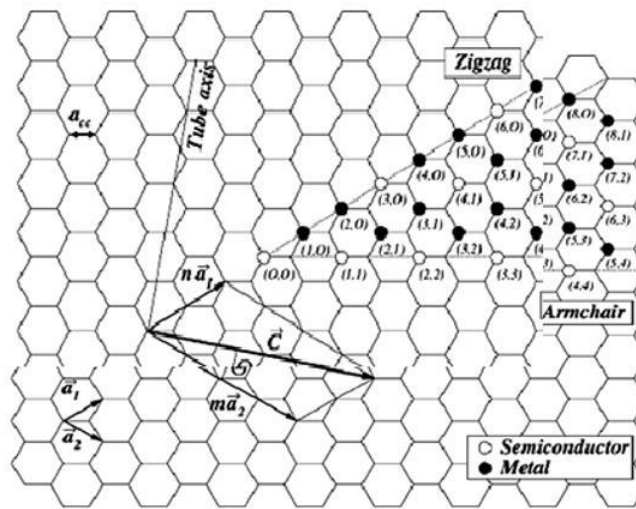


Fig. 1. The 2D graphene sheet diagram showing a vector structure classification used to define CNT structure.

Carbon nanotubes are only described by the pair of integers (n,m) which is related to the chiral vector. It can be seen from Figs. 1–3 three types of CNTs are revealed with these values:
 $m = 0$ for all zig-zag tubes and ($h = 30^\circ$);
 $n = m$ for all armchair tubes and ($h = 0^\circ$);
 Otherwise, when n, m they are called chiral tube and ($0^\circ < h < 30^\circ$).

The value of (n,m) determines the chirality of CNT and affects the optical, mechanical and electronic properties. CNTs with $|n - m| = 3i$ are

metallic like as in $(10,10)$ tube, and those with $|n - m| = 3i \pm 1$ are semiconducting like as in $(10,0)$ tube, (i is an integer)

The armchair and zig-zag tubes structures have a high degree of symmetry. These terms refer to the arrangement of hexagons around the circumference. While the chiral tube structure, which in practice is the most common, meaning that it can exist in two mirror-related forms.

The three distinct ways in which a graphene sheet can be rolled into a tube are shown in Fig. 2.

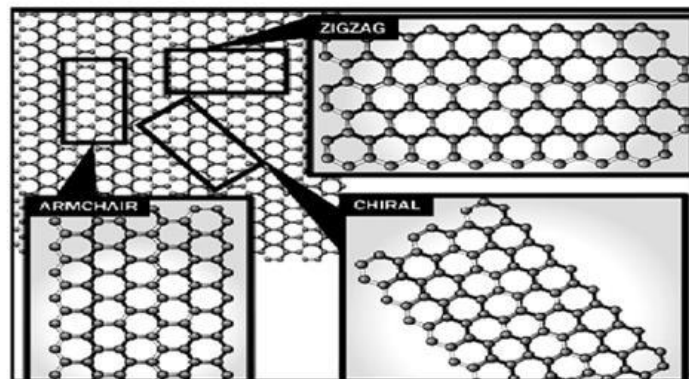


Fig. 2. Schematic diagram showing the way of formation different CNTs chirality structures.

For example; to produce a CNT with the indices, say, the sheet is rolled up so that the atom labelled (0,0) is superimposed on the one labelled. CNTs structural types are shown in Fig. 3 .

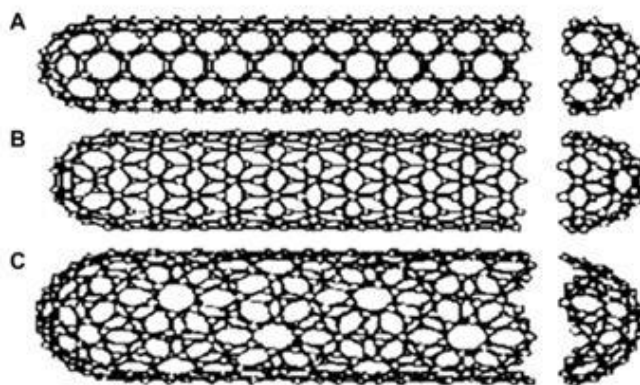


Fig. 3. CNTs structure with different chiralities. The difference in structure is easily shown at the open end of the tubes. (A) armchair structure, (B) zig-zag structure, (C) chiral structure.

The terminating cap of CNT is formed from pentagons and hexagons. The smallest cap that fits on to the cylinder of the carbon tube seems to be the well-known C_{60} hemisphere. The smallest experimental value of CNT diameter of 0.7 nm is in good agreement with this cap (6). However, some authors have recently studied CNTs at the theoretical limit of 0.4 nm in diameter. These CNTs are sometimes capped with a C_{20} dodecahedron.

Specific surface area gives good information of CNT characteristics and properties. Using some geometrical calculations, the theoretical external specific surface area for CNTs have been determined. For one side of graphene sheet, the value obtained is $1315 \text{ m}^2\text{g}^{-1}$ but using different multi-walled geometries and nanotubes bundles the value decreases to $50 \text{ m}^2\text{g}^{-1}$.

The easiest way to visualise how CNTs are built up is to

start with graphite, the most stable form of crystalline carbon. Graphite consists of layers of carbon atoms. Within the layers, the atoms are arranged at the corners of hexagons which fill the whole plane (in the idealized case without defects). The carbon atoms are strongly (covalently) bound to each other (carbon-carbon distance 0.14 nm). The layers themselves are rather weakly bound to each other (weak long-range van der Waals-type interaction, interlayer distance of 0.34 nm). The weak interlayer coupling gives graphite the property of a seemingly very soft material, the property which allows using graphite in a pen to write with.

The nature of the bonding of a CNT is described by applied quantum chemistry, specifically, orbital hybridisation. The chemical bonding of CNTs is composed entirely of sp^2 bonds, similar to those of graphite. This bonding structure, which is stronger than the sp^3 bonds found in diamond, provides the molecules with their unique strength. CNTs naturally align

themselves into ropes held together by van der Waals forces. Under high pressure, CNTs can merge together, trading some sp^2 bonds for sp^3 bonds, giving great possibility for producing strong, unlimited length wires through high pressure CNT linking (7).

In their (8) paper authors investigated the synthesis of carbon nanotubes.

Chemical vapor deposition (CVD): CVD is a technique in which the vaporized reactants react chemically and forms a nanomaterial product that is deposited on the substrate Figure 4.

Sources for carbon: The precursor for carbon nanotubes are hydrocarbon gases such as acetylene, ethylene, methane, etc. .

Substrate used: Substrates are materials on which the CNTs are grown. The commonly used substrates in CVD method are zeolite, silica, silicon plate coated with iron particles, etc.

Catalyst used: To produce single-walled carbon nanotubes metal catalyst nanoparticles such as iron, cobalt, nickel, molybdenum, iron-molybdenum alloys, etc. are used.

Sources for CVD used: Based on the heating source, the CVD can be:

- Thermal activated CVD which is heated by IR radiation, RF heater, etc.
- Photo assisted CVD which is heated by Arc lamps, CO_2 laser, Argon ion laser, Nd:YAG laser, etc.
- Plasma assisted CVD which is heated by microwave radiation, etc.

Conditions maintained: The following conditions are maintained inside the furnace.

- Temperature: $500-900^\circ\text{C}$.
- Inert gas atmosphere: Argon gas.

Procedure for synthesis of CNTs by thermal CVD method

CNTs are synthesized by thermal CVD method by using hydrocarbon gas as carbon source. In this method, a quartz tube is placed inside a furnace

maintained at high temperature (500–900°C) heated by RF heater. A crucible containing the substrate coated with catalyst nanoparticles is placed inside quartz tube filled with inert gas such as argon gas.

The hydrocarbon gas (carbon source) is pumped into the quartz tube which undergoes pyrolysis reaction and forms vapor carbon atoms. These carbon atoms bind

to the substrate and join to each other by Vanderwaal force of attraction and grow as multi-walled carbon nanotubes (MWCNTs) on the substrate [23]. To synthesize single-walled carbon nanotubes catalyst nanoparticles of Fe, Co, Ni are used. The obtained CNTs are further purified to get the pure form of CNTs.

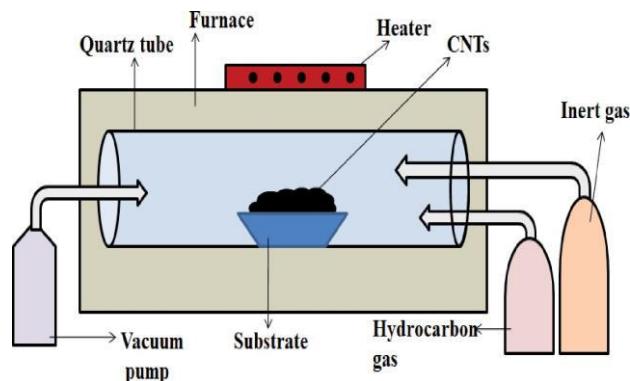


Fig.4. CVD method.

Electric arc discharge method

Carbon nanotubes are synthesized by electric arc discharge method which is also called Plasma Arcing method.

Electrodes: Pure graphite rods (both positive and negative electrode). The positive electrode is adjustable from outside to maintain the gap between the two electrodes.

Diameter of electrodes: 5–20 μm . **Gap between electrodes:** 1 mm. **Current:** 50–120 amperes.

Voltage: 20–25 V.

Inert gas pressure: 100–500 torr (No CNT formed below 100 torr). Inert gas is used for cooling and condensation of atoms to form the CNTs. Inert gas determines the structure of carbons to be present in CNTs. Commonly used inert gas is helium gas.

Temperature: 3000–3500°C.

Reactor: It contains a quartz chamber which is connected to vacuum pump and a diffusion pump to inert gas supply. Initially the chamber is made vacuum by the vacuum pump and then the chamber is filled with helium gas by the diffusion pump [9].

Procedure for synthesis of CNTs by Electric arc discharge method

In this method, a potential of 20–25 V is applied across the pure graphite electrodes separated by 1 mm distance and maintained at 500 torr pressure of flowing helium gas filled inside the quartz chamber figure 5. When the electrodes are made to strike each other under these conditions it produces an electric arc. The energy produced in the arc is transferred to the anode which ionizes the carbon atoms of pure graphite anode and produces C^+ ions and forms plasma (Plasma is atoms or molecules in vapor state at high temperature). These positively charged carbon ions move towards cathode, get reduced and deposited and grow as CNTs on the cathode. As the CNTs grow, the length of the anode decreases, but the electrodes are adjusted and always maintain a gap of 1 mm between the two electrodes. If proper cooling of electrodes is achieved uniform deposition of CNTs are formed on the cathode which is achieved by inert gas maintained at proper pressure [10]. By this method multi-walled carbon nanotubes are synthesized and to synthesize single-walled carbon nanotubes catalyst nanoparticles of Fe, Co, and Ni are incorporated in the central portion of the positive electrode. The obtained CNTs are further purified to get the pure form of CNTs.

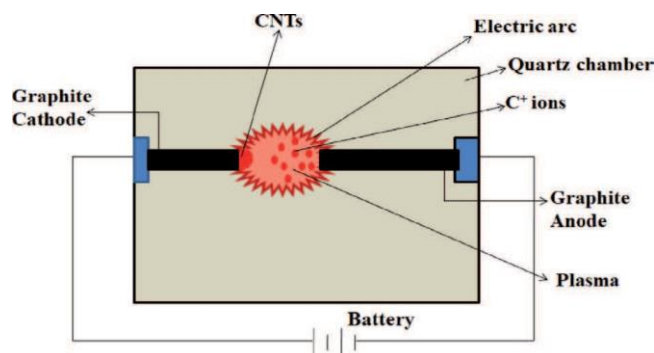


Fig. 5. Electric arc method.

Laser ablation method

Physical vapor deposition (PVD): PVD is a technique by which a material can be vaporized into gaseous form and then deposited on the surface of a substrate.

Target source: The most common carbon source target used is solid graphite which is irradiated by laser source and vaporized into vapor carbon atoms.

Laser source: Laser source used for vaporization of target material into target vapor atoms can be continuous laser source such as CO₂ laser or pulsed laser source such as Nd:YAG laser (Neodymium doped Yttrium Aluminum Garnet, Nd:Y₃Al₅O₁₂).

Substrate used: The substrate used in this method is the water cooled copper collector on which the vaporized carbon atoms deposit and grow as CNTs.

Inert gas atmosphere: Argon gas is commonly used as inert gas which flows at a constant flow rate towards the water cooled copper collector.

Procedure for synthesis of CNTs by Laser Ablation method

Laser Ablation method is a Physical Vapor Deposition method in which graphite target is vaporized by laser source Figure 6. In this method the graphite target is placed at the center of quartz chamber filled with argon gas and maintained at 1200°C. The graphite target is vaporized by either continuous laser source or pulsed laser source. The vaporized target atoms (carbon) are swept toward cooled copper collector by the flow of argon gas. The carbon atoms are deposited and grown as CNTs on cooled copper collector. In case of continuous laser beam, the carbon atoms are continuously vaporized whereas in case of pulsed laser beam the amount of CNTs produced can be monitored as each shot of pulsed laser beam is directly proportional to the amount of carbon atoms vaporized [11]. By this method multi-walled carbon nanotubes are synthesized and to synthesize single-walled carbon nanotubes catalyst nanoparticles of Fe, Co, Ni are used.

The obtained CNTs are further purified to get the pure form of CNTs.

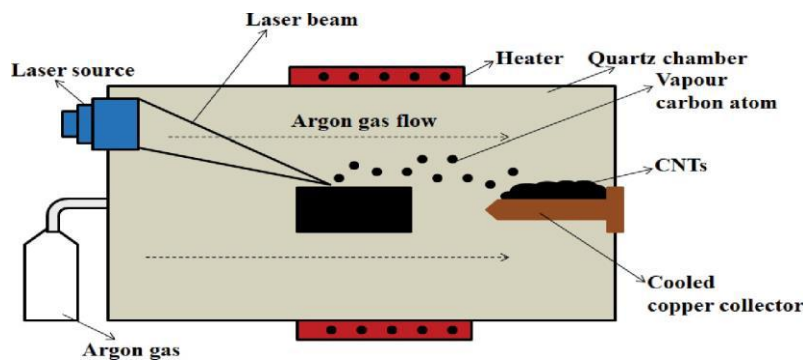


Fig. 6. Laser ablation method—schematic representation.

Procedure for pulsed laser deposition method

Pulsed Laser deposition is a thin film deposition technique in which the target material is vaporized by pulsed laser beam and vaporized target atoms are made to deposit on substrates Figure 7. The furnace contains a target at bottom and substrate mounted on the top. A pulsed laser beam from

Nd:YAG laser source is made to strike the target to produce vaporized target atoms called the plume (plume is vaporized atoms at high temperature) [12]. The plume moves towards the substrate and it is deposited and grown as CNTs. Each shot of laser is directly related to the amount of material ablated, thus deposition rate can be controlled and calibrated.

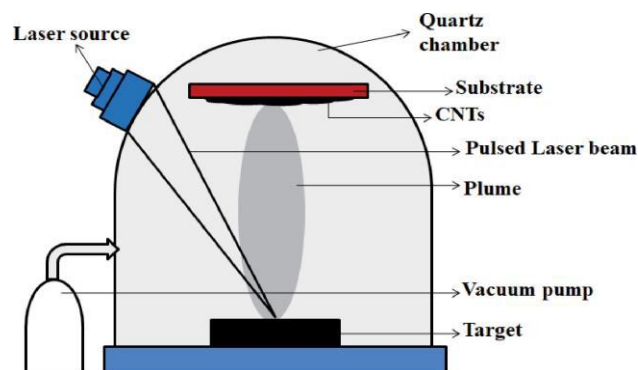


Fig. 7. Pulsed laser ablation method—Schematic representation.

The synthesis methods were investigated by Seyed Oveis Mirabootalebi, Gholam-Hosein Akbari Fakhrabadi. Authors (13).

First synthesis of cnt was done accidentally by arc discharge (1) and now synthesis methods of carbon nanotubes are different and various. Generally, produce type can specified properties of cnt (15); precursor (which can be solid, liquid, or gas), heat source, time, temperature, atmosphere of reactions and commonly; mechanism, determinate traits of cnt. Most common methods for synthesis of carbon nanotube are arc discharge, laser ablation and chemical vapor depositio n (15-19). Some of other methods for synthesis of carbon nanotubes include: dipping graphite in cold water (21), mechano-thermal (20), synthesis with decomposition Sic, torsion of graphene layers, with solar energy, synthesis with heat treatment of polymer, pyrolysis, with liquid phase and electrolysis.

Electrolysis method

This method based on liquid phase which was invention in 1995. with electrowinning of alkali or alkaline-earth metals from their chloride salts, cnt deposited on substrate (22).

By applying DC voltage between two electrodes in chamber of molten alkali-alkaline earth metals, could be produced multi walled carbon nanotubes. Relation (1) show formation lithium carbide (23).



By forming lithium carbide (Li_2C_2), synthesise of cnt can be started in liquid phase. Generally; diameter of cnt in this method was 2-10 nm and length of them is 0/5 micrometer or more was reported and amorphous carbon, carbon nanofibers, nanographites and encapsulate cnt are byproducts of this method (24). Obtained Cnt usually are multi walled, but also in some researches, produced single walled cnt (26)

Different salts, applied for producing cnt such as NaCl, LiCl, KCl, and LiBr (25). Current density, electrolysis regimes, time, molten salt and temperature are the controller parameters of reaction. By optimizing condition of process, the reaction yields up to 20- 40% increase for producing multi walled carbon nanotubes].

Electrolysis can be done in low temperature, don't need to advanced equipment, possibility to controlling process of synthesise, have high quality, having low energy consumption and also don't suitable for mass production.

CVD method

Cvd method known as simple way with gas precursor that containing carbon such as CO_2 or C_2H_2 , C_2H_4 and other hydrocarbons and temperature of cvd changing amount 350-1000 °C. Different parameters influence on cnt growth; such as: time and temperature of reaction, diameter of catalyst,

rate and type of reactant gas .

Classification methods of cvd, based on energy source and categorization in various types; for example when heat source is thermal resistance, flame or infrared lamps, this cvd called thermalcvd and also mechanism and catalyst of process effective in nominated of cvd.

Common methods for synthesis cnt are: plasma enhanced PE-CVD², aerosol CVD AA-CVD³, with aerogel, with alcohol catalyst assisted AC-CVD⁴, with laser LCVD⁵, water assisted WA-CVD⁶, hot filament HF-CVD⁷, oxygen assisted, with plasma radio frequency RF-PE-CVD⁸⁸, with plasma microwave MPE-CVD⁹ and catalytic CVD or CCVD¹⁰[23,40,41]. Figure (2) show variety methods of cvd for synthesis carbon nanotubes.

Using plasma leading to increase velocity of reactions and Main properties of plasma enhanced is lower temperature than other methods, whilst minimum temperature of normal cvd 500°C reported, synthesis temperature of carbon nanotubes and carbon nanofibers by plasma assisted even 120°C reported and also this type with comparison other low temperature methods, have better vertically growth.

In cvd with aerosol, aerosol using as catalyst which catalyst particles distribution on substrate and help to synthesis cnt on substrate (28) Many researchers reported this method synthesizing high quality single and multiwall carbon nanotubes (28-30).

In aerogel type, sediments deposition on aerogel. Efficiency of Aerogel cvd is high (200% weight percentage for single-wall). The key point for high efficiency is high surface area of aerogel and so increase performance of alumina catalyst.

In alcohol cvd, alcohols use as carbon source which Fe and Co catalyst put on zeolite and evaporated alcohol (often methanol and ethanol), splashing over catalyst particles.

Temperature of process is rather low (about 550°C) that lower than other common cvd methods. Diameter of carbon nanotubes about 1 nm and efficiency of process is 40% . Due to the high purity, low production costs and high efficiency, this method can be used for mass production of carbon nanotubes.

In L-cvd; focusing a laser beam on a small portion of the substrate, prevents damage of substrate. We have more control over synthesis parameters and on the other hand does not need to warm up all the substrate.

In water assisted cvd, the amount of water entering the process can be controlled and with precise control of amount of water can be achieved over 7 mm length of cnt.

In oxygen assisted-cvd, with a certain proportion adding oxygen to other gasses, single walled cnt with high efficiency could be synthesised. In fact; by adding oxygen to hydrogen, can be more control over the process and stop destruction sp² bonds that led to the steady alignment growth of single-walled nanotubes.

Added oxygen also leads to the loss of amorphous carbon and other carbon impurities and

remove the destructive precursor role during the growth and on the other hand, increasing the purity and efficiency; however, this method for some catalysts like separate iron nanoparticles due to carbothermal reaction, is not suitable .

Mechano Thermal method

Mechano thermal containing two main steps; first producing amorphous carbon and subsequently, annealing them in vacuum furnace. Carbon amorphisation done by high energy ball milling. Milling time for synthesis amorphous carbon up to 180 h that change for different condition: difference in type of atmosphere (Ar or air), cup speed (300 rpm or more), ball to powder ratio, numbers of balls and purity of powders. With increasing milling time, crystallite size decreasing and finally forming amorphous structure.

With attention to long time of milling, very small amount of metal powders due to Friction between the cup and balls, enter the graphite powder and possibility help to nucleation and growth of cnt in thermal step.

Produced amorphous carbon putting in vacuum furnace. Temperature of furnace 1400° C for a few hours to connecting atoms of amorphous carbons together and forming carbon nanotubes. Structure of produced carbon nanotubes is usually springy multi walled nanotubes.

Properties of Mechano-thermal includes: simple process, suitable for mass production, low cost, and don't need to special equipments, butt the time of process is too long and mechanism of process is not continuous and inclusive two steps.

Laser Ablation method

In Laser ablation/vaporization, by strike pulsed laser or continuous wave laser on graphite target; nucleation and growth of carbon nanotubes to be started (31,23). First formation a hot evaporation and subsequently quickly cooled.

During cooling of the samples, small molecules and carbon atoms quickly condense and form larger clusters and synthesized carbon nanotubes by van der waals forces stay together. For producing multi wall carbon nanotubes use pure graphite rods and for single wall use composite block of graphite. For producing single walled, Graphite composited with metal catalyst, such as Fe, Ni and Co and He-H₂ and Ar use as ambient gas.

In pulsed laser, needs more intensity laser's light than continuous laser. Nd:YAG and CO₂ are most common lasers used for laser ablation (31).

Diameters of cnt which produced by this method 4-30 nm and length of them is about 1 micrometer. Byproducts and impurities are amorphous carbon, catalyst particles, fullerene etc. Catalysts also help to growth of carbon nanotubes. Most of catalyst were used in laser ablation are: Co, Cu, Nb, Ni, Pt, Co/Ni, Co/Pt, Co/Cu, Ni/Pt. quality of production related to target composition , power of laser beam and laser

properties, catalyst type, type of ambient gas , temperature of reactions and distance between substrate and target (31). Produced carbon nanotubes by this method have high purity, high yield and most produced single wall cnt; but not suitable for mass production and also need expensive and especial equipments .

Flame Synthesis

In this method, cnt synthesizing by direct combustion of carbon source in presence of an oxidizing gas (23). Generally; flame synthesis contain of three steps. First producing carbon source by hydrolysis of hydrocarbon. Second; diffusion of carbon's atoms to metallic catalyst and third; nucleation carbon nanotubes on surface of catalyst and it's gradual growth.

Oxidation gas can be oxygen or nitrogen and carbon feedstock are acetylene, methane, ethanol and ethylene. Type of flame created, have essential role on quality of produced carbon nanotubes and determinate amount of amorphous carbon in final producing. For optimizing condition, must be control temperature, composition of fuel gas and catalyst of reactions. This way is economic, suitable for mass production and most synthesizing single walled cnt, but rate of growth is relatively low.

Arc discharge

Arc discharge known as one of oldest method for producing carbon nanotubes (14). Two high purity graphite rods used as anode and cathode and by applied direct current (in some cases pulsed current), a stable arc is created. Due to the power of created arc, carbon separated from anode and condensed on cathode to forming of soot (23).

Arc discharge done in various environment such as: liquid environment (liquid nitrogen, toluene, not ionized water), gas environment (Ar, Ar-H, He) or in plasma rotating arc discharge. Plasma rotating arc discharge is an economic method for large-scale synthesis of carbon nanotubes. Centrifugal force which created by rotation, accelerating the evaporation of anode and also cause uniform and stable dispersion of arc and so increases volume and temperature of discharge plasma.

Most carbon nanotubes that synthesised by arc method are multi walled but by penetration graphite rods and filling them with graphite's powder and metal catalyst; can be achieve to single wallcarbon nanotubes.

Pressure of Steam chamber and flow rate; are two key parameters for controlling the process. In arc discharge; speed of process is high and synthesis condition is controllable, but both of quality of productions and efficiency of process is low.

The synthesis methods were analyzed by Nur-Azzah Afah Binti Taib , Sarawak Md. Rezaur Rahman, Mohammed Mahbul Matin, Jamal Uddin, Muhammad Khusairy Bin Bakri, Afrasyab Khan Authors (30).

Laser vaporization method

The CNTs were first synthesized using a laser in 1995, and the pulsed laser vaporization (PLV) technique is used to extract a large variety of carbon allotropes from graphite, one of which is CNTs. A laser beam (Yttrium Aluminum Garnet or CO₂ laser) was used in this process, and it will be put within a reactor, where it will be focused on the graphite rods. Until beginning the process, argon buffer gas and a

catalyst mixture of Co and Ni in a 50:50 ratio was passed through the rod at 1200°C. The metal was added to the process to help catalyze the creation of SWCNTs, but it also produced a slew of other byproducts. As a result of the high temperature of the argon buffer steam, the rod will vaporize. As the vaporization was cooled, it was deposited in the copper collector, and nanotubes were formed (33,34). The schematic diagrams for the laser ablation procedure are shown in Fig. 8.

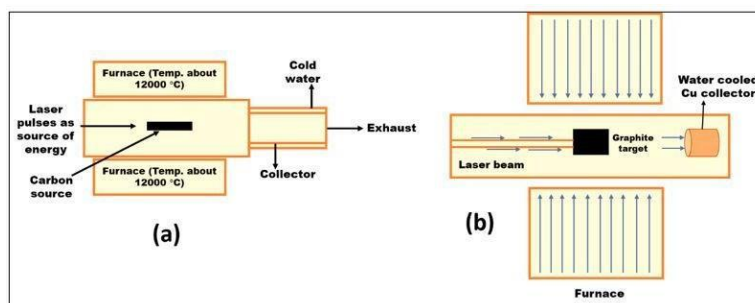


Fig. 8. Schematic diagram for laser ablation technique.

One of the benefits of this method is that high-quality SWCNTs with limited defects can be achieved in a reasonably high yield. Since the metallic atoms appear to vaporize when the tube's end is closed, this was possible. SWCNTs generated have excellent structural integrity as well. Furthermore, diameter modulation of the samples can be achieved easily by adjusting the method's parameters, i.e. catalytic metal, flow rate, and temperature. Apart from that, SWCNTs can be synthesized without requiring the production of MWCNTs.

However, there are several drawbacks to this approach. The CNTs generated may have some branching and may not be perfectly straight. Despite using higher purity graphite rods and laser forces, the amount of CNTs generated is lower than when the arc discharge approach is used (35). Typically, a significant amount of SWCNTs can be generated with good crystallization using both arc discharge and laser ablation methods. However, owing to the unique basic equipment requirements and high energy demand, these two strategies are less advantageous than CVD. In terms of yield and purity, CVD are superior to arc and laser methods. This is because the size of the carbon source, i.e., anode for arc discharge and target for laser ablation, determines the amount of the sample formed in both arc and laser processes. There is also a need for intensive purification of CNTs developed using these two techniques, which led to the production of gas phase methods like CVD.

Chemical vapor deposition (CVD) method

CVD is showing high potential to be used further as a CNTs processing tool for future industrial applications due to advantages such as relatively low growth temperature, high yields, and high purities

with many explicit properties that can be obtained during its manufacture. While this process was first used in the 1960s and 1970s to produce carbon fibers and carbon nanofibers, it was not until 1996 that it was used on a wide scale for the production and synthesis of CNTs. Strong, liquid, and gaseous precursors were used to aid in the development of CNTs at relatively low temperatures, i.e., 500 to 1000°C, and at atmospheric pressure. Metal or metal oxide catalyst particles are used as "seeds" to aid in the development of certain precursors. In addition, the gaseous or volatile carbon compound can decompose with the aid of metallic nanoparticles as a catalyst in this step. The catalyst also serves as a nucleation site for the development of CNTs. The reaction chamber is filled with a combination of nitrogen, ethylene, and acetylene during the procedure. This approach allows CNTs to expand in a variety of macroscopic morphologies, including powders and films (i.e., thick or thin), as well as various microscopic architectures (i.e., aligned, coiled, intertwined, or straight). The simplicity of the process is due to the use of such precursors, as well as different substrates and catalysts. As a result, producers will get the desired type of CNT. The four key parameters that specify the form of CNTs formed (SWCNT or MWCNT) in this process are the reactor's atmosphere, the source of hydrocarbon, the catalyst, and the growth temperature. MWCNTs are typically formed at lower temperatures (i.e. 600 to 900°C), while SWCNT development occurs at temperatures greater than 900°C. Not just that, but the commodity obtained is purer and has a higher yield. Regardless, defects can be detected in the composition of the samples collected, and these defects are normally in significant numbers. The general and basic schematic diagrams for the CVD technique are shown in Fig.9.

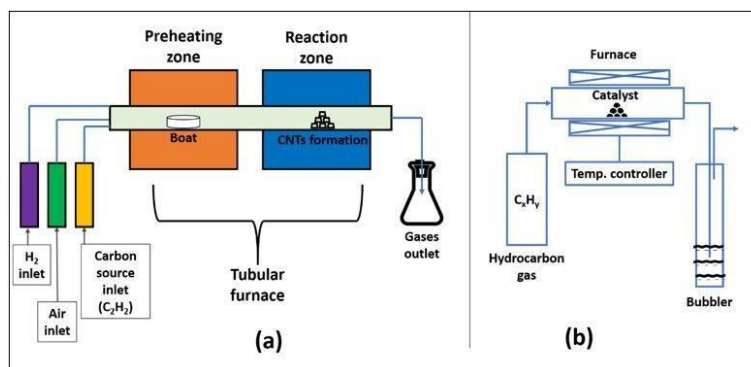


Fig. 9. Schematic diagrams of CVD process.

Thermal catalytic CVD

Decomposition of hydrocarbons or other carbon feedstock will take place at elevated temperatures ranging from 500 to 1200°C in this process. Prior to use, the feed would be dissolved in a steady flow of noble gases in the furnace, which would pass through transition metal catalysts such as iron, nickel, and cobalt, among others. The decomposed carbon would dissolve such metal particles until it reached a point of super saturation. The hydrocarbon is then decomposed and deposited on a substrate, i.e., alumina, glass, or silicon substrate. The carbon precipitate would then form in the shape of fullerene forms. Depending on the temperature range of the process, different forms of CNT may be produced by using various types of carbon feedstock. Chemical composition and textural properties of the catalyst material(s) used are two parameters that control the length, diameter, orientation, and consistency of produced CNTs. The amounts of defects and the existence of amorphous carbon was also used to test the above properties of the finished product.

Plasma-enhanced CVD (PECVD)

PECVD is a broad concept that encompasses a variety of synthesis methods which may be either direct or remote. Direct PECVD was used to make MWCNT field emitter towers and some SWCNTs, while remote PECVD can be used to develop all types of CNTs. Instead of using thermal energy, this method uses energy sources that can supply energy for both hydrocarbon decomposition and CNT processing at a low temperature. The plasma energy sources used on the CNT formation are hot filament PECVD, direct current PECVD, radio frequency PECVD, and microwave PECVD. Hydrocarbon gas is used over intermediate metals in an ionized state in this process. Furthermore, the reactive species in the plasma system influenced the development of microscopic diameter tubes, which had implications for both diameter regulation and selective etching of metallic SWCNTs. The PECVD process consists of three major stages: (i) primary reaction takes place between energetic particles and carbon precursor in nonequilibrium plasma which leads to the precursor to be decomposed into carbon atoms and other active radicals; (ii)

diffusion of carbon atoms and radicals onto the catalyst surface, as well as secondary reactions between the reactants, and (iii) catalyst interacts with the reactants on its surface, allowing carbon atoms to infiltrate and precipitate, as well as the release of result gases (Ding et al., 2016). This kind of CVD process has the benefit of producing a high yield of matched CNTs at a lower substrate temperature. Furthermore, by adding a voltage to the substrate, the volume of supplied ionized carbon species onto the catalyst surface can be tuned. The chirality distribution and growth rate of SWCNTs can be regulated, for example, by adjusting catalyst size and H₂ flow rate. This kind of CVD process has the benefit of producing a high yield of matched CNTs at a lower substrate temperature. Furthermore, by adding a voltage to the substrate, the volume of supplied ionized carbon species onto the catalyst surface can be tuned. The chirality distribution and growth rate of SWCNTs can be regulated, for example, by adjusting catalyst size and H₂ flow rate.

Alcohol CVD (ACCVD)

Since the temperature of the process is relatively low as low as 550°C, the ACCVD system can produce SWCNTs in large quantities at a low cost. Evaporated methanol and ethanol are applied to zeolite-supported iron and cobalt catalytic metal particles in this process. Alcohol reacting with catalytic metal particles created hydroxyl radicals, which removed carbon atoms with hanging bonds, preventing the formation of high-purity SWCNTs.

CONCLUSION

Nanomaterials provide an enriched knowledge on distinct probability and also definitely sound well in biomedical regenerative therapy for its uniqueness owing to its excellent physical as well as chemical properties.

Among of the main methods for synthesising carbon nanotubes, chemical vapour deposition due to simplicity, controllable mechanism, high ability for synthesizing aligned cnt, variety modified types for producing different kind of cnt, high efficiency close to 100% and suitable for mass producing; is the most attractive way for synthesis of carbon nanotubes.

Flame synthesis have high potential for producing economical large scale of cnt that have a simple mechanism; but increasing impurities is a big problem in this mechanism.

Laser ablation and Arc discharge are common method for synthesis cnt that both of them not suitable for mass production, besides that; quality of yields in

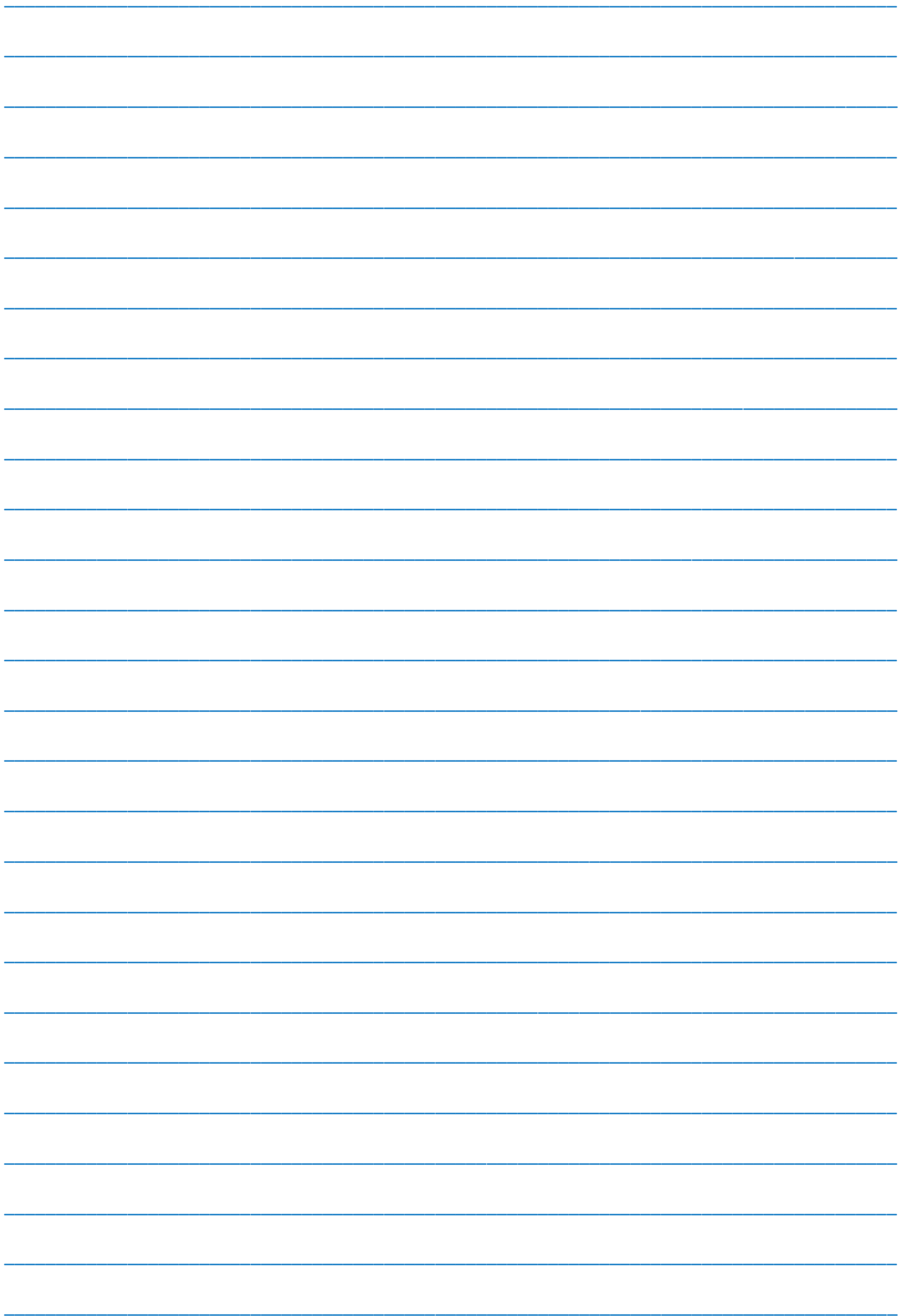
arc discharge is low. The problem of mass production also exist for electrolysis, and this method used in laboratory scale. In mechano thermal despite simplicity and large scale of production, not continuous (consist of two steps) and process is very slow.

- [1] *Ahmad Aqel, Kholoud M.M. Abou El-Nour, Reda A.A. Ammar, Abdulrahman Al-Warthan.* Carbon nanotubes, science and technology part (I) structure, synthesis and characterization. *Arabian Journal of Chemistry* (2012) 5, 1–23.
- [2] *S. Dolmer.* 20003. <http://www.inano.dk/sw180.asp>. Denmark. [online] available.
- [3] *K. Tanaka, T. Yamabe, K. Fukui.* 1999. *The Science and Technology of Carbon Nanotubes*, First ed. Elsevier, Oxford.
- [4] *S. Iijima.* 1991. *Nature* (London) 354, 56.
- [5] *P. Harris.* 2003. A Carbon Nanotube Page, Chemistry Department of the University of Reading, <http://www.personal.rdg.ac.uk/~scsharip/tubes.htm>. [online] Available.
- [6] *M.S. Dresselhaus, G. Dresselhaus, R. Saito.* 1995. *Carbon* 33, 883.
- [7] *T. Yildirim, Oş Gü İseren, Kılıç, S. Ciraci.* 2000. *Phys. Rev. B* 62, 19.
- [8] *Aravind Kumar Jagadeesan, Krithiga Thangavelu and Venkatesan Dhananjeyan.* Carbon Nanotubes: Synthesis, Properties and Applications. [21st Century Surface Science](#). Published: July 31st, 2020.
- [9] *V.P. Pham, S-H Jang, D. Whang, J.Y. Choi.* Direct growth of graphene on rigid and flexible substrates: Progress, applications, and challenges. *Chemical Society Reviews*. 2017;46:6276-6300.
- [10] *V.P Pham.* Hexagon flower quantum dot-like Cu pattern formation during low-pressure chemical vapor. Deposited Graphene growth on a liquid Cu/W substrate. *ACS Omega*. 2018;3:8036-8041.
- [11] *T. Torres.* Carbon nanotubes and related structures: Synthesis, characterization. In: *Functionalization and Applications*. Vol. 135. Weinheim: Wiley-VCH; 2010. pp. 215-228. Available from: <https://doi.org/10.1002/anie.201006930>
- [12] *P.J.F, Haris, A. Hirsch, C. Backes.* Carbon Nanotubes Science: Synthesis, Properties and Applications. Vol. 102. Germany: Cambridge University Press; 2009. pp. 210-23
- [13] *Seyed Oveis Mirabotalebi, Gholam-Hosein Akbari Fakhraadi.* National Conference on Nanostructures, Nanoscience and Nanoengineering 2017.
- [14] *S. Manafi, M. Rahimpour, and Y. Pajuhfar.* The synthesis of peculiar structure of spring-like multiwalled carbon nanotubes via mechanochemical method. *Ceramics International*, 2011. 37(7): p. 2803-2808.
- [15] *D.M. Guldi, and N. Martin.* Carbon nanotubes and related structures: synthesis, characterization, functionalization, and applications. 2010: John Wiley & Sons.
- [16] *B. Zheng, Y. Li, and J. Liu.* CVD synthesis and purification of single-walled carbon nanotubes on aerogel-supported catalyst. *Applied Physics A*, 2002. 74(3): p. 345-348.
- [17] *Y. Ando et al.,* Growing carbon nanotubes. *Materials today*, 2004. 7(10): p. 22-29.
- [18] *D.H. Toubestani et al.* CVD Growth of Carbon Nanotubes and Nanofibers: Big Length and Constant Diameter. in *Macromolecular symposia*. 2010. Wiley Online Library.
- [19] *Y. Chen et al.,* The nucleation and growth of carbon nanotubes in a mechano-thermal process. *Carbon*, 2004. 42(8): p. 1543-1548.
- [20] *Z. Kang, et al.,* One-step water-assisted synthesis of high-quality carbon nanotubes directly from graphite. *Journal of the American Chemical Society*, 2003. 125(45): p. 13652-13653.
- [21] *A. Szabó, et al.,* Synthesis methods of carbon nanotubes and related materials. *Materials*, 2010. 3(5): p. 3092-3140.
- [22] *M. Terrones.* Science and technology of the twenty-first century: synthesis, properties, and applications of carbon nanotubes. *Annual review of materials research*, 2003. 33(1): p. 419- 501.
- [23] *G.Z. Chen et al.,* Electrochemical investigation of the formation of carbon nanotubes in molten salts. *High Temperature Material Processes*, 1998. 2: p. 459-470.
- [24] *Z. Ren, Y. Lan, and Y. Wang.* Aligned carbon nanotubes: physics, concepts, fabrication and devices. 2012: Springer Science & Business Media.
- [25] *R.E. Smalley et al.,* Carbon nanotubes: synthesis, structure, properties, and applications. Vol. 80. 2003: Springer Science & Business Media.
- [26] *P. Queipo et al.,* Aerosol Catalyst Particles for Substrate CVD Synthesis of Single-Walled Carbon Nanotubes. *Chemical Vapor Deposition*, 2006. 12(6): p. 364-369.
- [27] *H. Byeon et al.,* Growth of ultra long multiwall carbon nanotube arrays by aerosol- assisted chemical vapor deposition. *Journal of nanoscience and nanotechnology*, 2010. 10(9): p. 6116-6119.
- [28] *S. Abdullayeva, et al.,* Characterization of high quality carbon nanotubes synthesized via

METHODS FOR SYNTHESIS OF NANOTUBES AND STRUCTURE

- Aerosol-CVD. Journal: JOURNAL OF ADVANCES IN PHYSICS, 2015. 11(4).
- [29] *M.M.A. Rafique, and J. Iqbal.* Production of carbon nanotubes by different routes-a review. Journal of encapsulation and adsorption sciences, 2011. 1(02): p. 29.
- [30] *Nur-Azzah Afah Binti Taib, Md. Rezaur Rahman, Mohammed Mahbul Matin, Jamal Uddin, Muhammad Khusairy Bin Bakri, Afrasyab Khan.* A Review on Carbon Nanotubes (CNT): Structure, Synthesis, Purification and Properties for Modern day Applications. Research Square. September 2021.
- [31] *R. Kaur, P. Vatta M. Kaur.* 2018. Carbon Nanotubes: A Review Article. International Journal for Research in Applied Science Engineering Technology 6(4):5075–5079. <https://doi.org/10.22214/ijraset.2018.4827>.
- [32] *A. Raunika, S.A. Raj Jayakrishna K, Sultan MTH.* (2017) Carbon nanotube: A review on its mechanical properties and application in aerospace industry. IOP Conference Series: Materials Science and Engineering. 270,012027. <https://doi.org/10.1088/1757-899X/270/1/012027>.
- [33] *G. Rahman, Z. Najaf, A. Mehmood, S. Bilal, S.A. Mian, G. Ali.* (2019) An Overview of the Recent Progress in the Synthesis and Applications of Carbon Nanotubes. C Journal of Carbon Research 5(1):1–31. <https://doi.org/10.3390/c5010003>.

Received: 15.03.2023



CONTENTS

1.	Thermal photons production in proton-proton collisions at high energies M.R. Alizada, A.I. Ahmadov	3
2.	Production of a Higgs-boson pair in e^-e^+ -collisions (II) S.K. Abdullayev, M.Sh. Gojayev	14
3.	Change in the properties of polymer nanocomposites (PP+ZrO ₂) with metal oxide nanoadditives after electrothermopolarization H.S. Ibrahimova	25
4.	Thermal photons production in proton-proton collisions at high energies Part II. Determination of dominant process of production of thermal photons M.R. Alizada, A.I. Ahmadov	29
5.	Instability of thermomagnetic waves in conducting media E.R. Hasanov, Sh.G. Khalilova, G.M. Mammadova	39
6.	Analysis of fluctuation conductivity in Y _{0,3} Cd _{0,7} Ba ₂ Cu ₃ O _{7-δ} V.M. Aliyev, G.I. Isakov, J.A. Rahimov, V.I. Eminova, S.Z. Damirova, G.A. Aliyeva	44
7.	Investigation of influence of barrier discharge plasma on barium titanate particle doped polyethylene by DSC method T.D. Ibragimov, I.S. Ramazanova, U.V. Yusifova, F.F. Yahyayev	49
8.	The Wigner distribution function of a semiconfined harmonic oscillator model with a position-dependent mass and frequency in an external homogeneous field. The case of parabolic well Shakir M. Nagiyev, Shovqiyya A. Amirova	56
9.	Methods for synthesis of nanotubes and structure (review article) A.M. Aliyeva	65



www.physics.gov.az